JOHANNES KEPLER
UNIVERSITÄT LINZ | JKU

TNF

Technisch-Naturwissenschaftliche
Fakultät

# Bose Gas of Tilted Dipoles in Coupled 2D-Layers—Ground State

BACHELORARBEIT

zur Erlangung des akademischen Grades

Bachelor of Science

im Bachelorstudium

Technische Physik

Eingereicht von:
Martin Hebenstreit

Angefertigt am:
Institut für Theoretische Physik

Beurteilung:
Priv.-Doz. Dr. Robert E. Zillich

Linz, September, 2013

## Abstract

This bachelor thesis discusses the homogeneous Bose gas of aligned dipoles trapped in coupled 2D layers. Hopping between the layers is not allowed. The ground state of the system is analyzed using hypernetted-chain Euler-Lagrange (HNC-EL) theory, neglecting elementary diagrams and triplet correlations. Dipoles in different layers are equivalent to a multi-component gas in one single 2D layer. The well known diagrammatic language of cluster expansions is introduced axiomatically in such a way that multi-component systems can be dealt with. We will take a step-by-step route deriving the HNC equation, Ornstein Zernike relation, and then formulate a set of conditional equations for the pair distribution function in such a form that numerical methods can solve them efficiently.

Results are presented, starting with one-layer systems, moving on to bi-layer systems with various dipole orientations, densities and distances between the layers. Pair distribution functions and static structure functions are computed in each case describing the ground state of the system. We concentrate on the bi-layer system varying the distance between the layers at fixed density and fixed tilting angle; tilting the dipoles at fixed density and fixed distance between the layers; and varying the density at fixed tilting angle and fixed distance between the layers. Out of the many possibilities of parameter combinations, we also present some special cases: A system with very different dipole densities in the two layers and a system with antiparallel dipole orientations. Finally we present results for a single tri-layer system and show how each of the three layers is correlated to each other.

## Zusammenfassung

Diese Bachelorarbeit beschäftigt sich mit homogenem Bose Gas bestehend aus ausgerichteten Dipolen in gekoppelten 2D Schichten. Ein Teilchenaustausch zwischen den Schichten ist nicht erlaubt. Die Hypernetted-Chain Euler-Lagrange (HNC-EL) Theorie wird benutzt um den Grundzustand des Systemes zu berechnen, Elementary Diagrams und Triplettkorrelationen werden dabei vernachlässigt. Dipole in verschiedenen Schichten sind äquivalent zu einem mehrkomponentigem Gas in einer einzigen Schicht. Die wohlbekannte Diagrammsprache wird axiomatisch auf eine Art und Weise eingeführt, dass auch mehrkomponentige Systeme behandelt werden können. Die HNC Gleichung, sowie die Ornstein Zernike Gleichung werden hergeleitet, die Gleichungen der HNC-EL Theorie soweit aufgelöst, bis bestimmende Gleichungen für die Paarverteilungsfunktion aufgestellt werden können, welche dann numerisch gelöst werden können.

Resultate für 1- und 2-Schichtensysteme werden besprochen. Dabei werden verschiedene Dichten, Dipolausrichtungen und Schichtabstände gewählt. Die Paarverteilungsfunktion sowie die statische Strukturfunktion beschreiben den Grundzustand des Systems und werden in jedem der Fälle berechnet. Wir gehen besonders auf das 2-Schichtensystem ein: Variieren der Schichtabstände bei fixer Dichte und Dipolausrichtung; Kippen der Dipole bei fixer Dichte und fixem Schichtabstand; Variieren der Dichte bei fixer Ausrichtung und fixem Schichtabstand. Aus den vielen möglichen Parameterkombinationen betrachten wir außerdem noch einige Spezialfälle: Ein System mit unterschiedlichen Dichten in den beiden Schichten, sowie ein System mit antiparallel ausgerichteten Dipolen. Schließlich zeigen wir noch ein 3-Schichtsystem und diskutieren die Kopplung der einzelnen Schichten untereinander.

# Contents

# 1 Introduction

Recently, dipolar Bose gases have become a popular field of research due to advances in the experimental realization of Bose-Einstein condensation (BEC). BEC was accomplished in gases of atoms with magnetic dipole moment. For example, erbium, a lanthanide, with both a large atomic mass of $m \approx 167.3u$ and a strong magnetic moment of $\mathfrak{m} \approx 7\mu_B$ is a candidate for a Bose gas with highly dipolar interactions. BEC of erbium atoms was achieved in 2012 [1], in some other magnetic atoms, chromium [9] and dysprosium [10], earlier. BEC is also interesting for molecules with electric dipole moment [14][15], since the electric dipole moment can be much stronger than the magnetic dipole moment of atoms. Thus theoretical investigation of dipolar quantum gases is rewarding. For more details see the recent review article [3].

The aim of this bachelor thesis is on the one hand to show the reader how the ground state of the strongly interacting Bose gas of aligned dipoles, trapped in coupled 2D layers (see Figure 1), is described using hypernetted-chain Euler-Lagrange (HNC-EL) theory and on the other hand to present results computed using this theory. This theory is based of the Meyer cluster expansion in diagrams in statistical mechanics. The method leads to results, not quite as accurate as Monte Carlo methods, but it gives some insights into the problem and helps familiarizing with the basic formalism. Though results of Monte Carlo simulations are more accurate, even the most simple version of HNC-EL gives results that are still qualitatively correct.

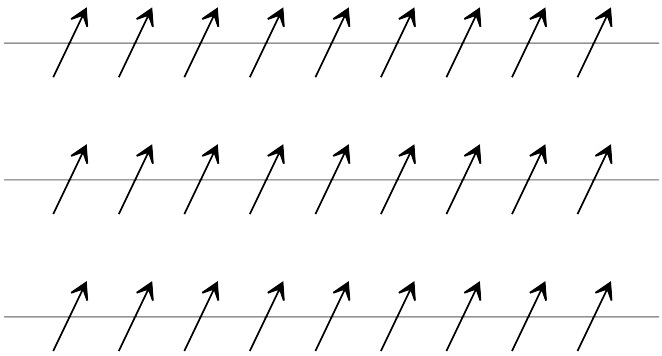

Figure 1: Aligned dipoles trapped in coupled 2D layers

A formalism is needed to describe the system. A quite helpful observation is that the dipoles in the different layers are equivalent to a multi-component system in one single layer with different interactions according to the particle types. This effectively reduces the inhomogenous, 3D Bose system to a homogenous multi-component 2D-problem. So, if we are talking about different particle types in this bachelor thesis, we are actually thinking of interacting dipoles which are situated in different layers.

We are treating homogeneous Bose systems, but note that the system is not isotropic just like the general dipole interaction isn't. Figure 2 shows a color map of the dipole-dipole interaction. The unit system is introduced in section 4.1. Note that there are cones of attractive interaction (along the dipole moment) and cones of repulsive interaction (perpendicular to the dipole moment). One can see that the dipole interaction is isotropic when dipoles are oriented perpedicular to the layer, but gets anisotropic when the dipoles are tilted.

We start with some important definitions in section 2. Important concepts, like the pair distribution function $g_2(\boldsymbol{r})$, will be introduced there. HNC-EL theory will be developed in section 3. Because of strong interactions mean field theory is not applicable in this case. In section 3.1 we thus make an ansatz for the wave function which includes pair correlations. According to Ritz' variational principle, the ground state can then be obtained by minimizing the energy functional [13, p. 133]. Therefore we'll have a look at the hamiltonian in section 3.2. In the process of calculating the functional derivative, one has to find a relation between the pair distribution function $g_2(\boldsymbol{r})$ and the pair correlations in the wave function. This relation is found via diagrammatic expansion in section 3.3. In the following subsections

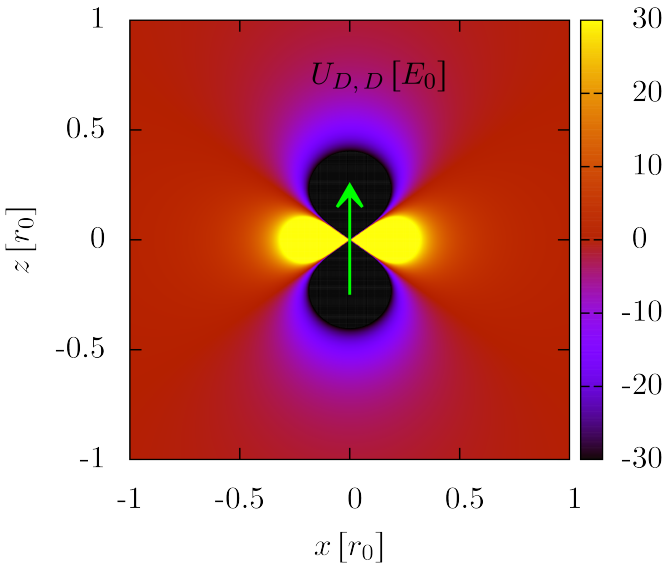


Figure 2: Dipole-dipole interaction energy

the most important equations of HNC-EL theory, Ornstein-Zernike relation and the hypernetted-chain equation, will be deduced. We arrive at a final set of equations in section 3.9. This set will be solved numerically in section 4.1, and finally computed results will be presented in sections 4.2 to 4.4.

In the course of this bachelor thesis the HNC-EL theory was derived for muli-component systems based on previous work on single-component systems [8]. The diagrammatic language [6] has been adapted for multi-component systems. The equations of HNC-EL theory have been deduced, an algorithm to solve the equations numerically was implemented in C++ and results were computed for several parameter (density, tilting angle, inter-layer distance) combinations.

## 2 Definitions

Important definitions are put down in this section, the less important ones will be placed where they are needed. In the following, Greek letters ($\alpha$, $\beta$, ...) used as indices will denote particle type (layer) variables, while Latin letters starting from $a$ ($a$, $b$, ...) will be used to label particle types consecutively. Latin letters starting from $i$ ($i$, $j$, ...) will be used to index particles of the same type, Arabic numbers will identify each single particle within the particles of a certain particle type (layer), they are indistinguishable though.

**Definition 1** (Naming Conventions, basic Nomenclature)**.**

$$\Omega := \textit{Volume} \tag{1}$$
$$M := \textit{Count of particle types} \tag{2}$$
$$N_\alpha := \textit{Count of particles of type } \alpha \tag{3}$$
$$N := \sum_\alpha N_\alpha \tag{4}$$
$$\boldsymbol{r}_{\alpha,\,i} := \textit{Coordinate of the } i\textit{th particle of type } \alpha \tag{5}$$
$$\boldsymbol{R} := \{\boldsymbol{r}_{a,\,1},\,\ldots,\,\boldsymbol{r}_{M,\,N_M}\} \tag{6}$$

**Definition 2** (Primed Sum)**.**

$$\sum_{\alpha_1,\,\alpha_2,\,\ldots,\,\alpha_n} \quad \sum_{i_1,\,i_2,\,\ldots,\,i_n}{}' := \sum_{\substack{(\alpha_1,\,i_1),\,(\alpha_2,\,i_2),\,\ldots,\,(\alpha_n,\,i_n),\\ (\alpha_k,\,i_k)\neq(\alpha_l,\,i_l)\ \textit{pairwise}}} \tag{7}$$

Of particular importance are sums over two particle types:

$$\sum_{\alpha,\,\beta}\sum_{i,\,j}{}' = \sum_{\substack{(\alpha,\,i),\,(\beta,\,j),\\ (\alpha,\,i)\neq(\beta,\,j)}} \tag{8}$$

**Definition 3** (N-Body Density [13, p. 133])**.**

$$\rho_n^{\alpha_1,\,\ldots,\,\alpha_n}(\boldsymbol{r},\boldsymbol{r}',\ldots,\boldsymbol{r}^{(n)}) := \sum_{i_1,\,i_2,\,\ldots,\,i_n}{}' \left\langle \delta(\boldsymbol{r}_{\alpha_1,\,i_1}-\boldsymbol{r})\delta(\boldsymbol{r}_{\alpha_2,\,i_2}-\boldsymbol{r}')\cdot\ldots\cdot\delta(\boldsymbol{r}_{\alpha_n,\,i_n}-\boldsymbol{r}^{(n)})\right\rangle \tag{9}$$

Of particular importance are the 1-body and the 2-body densities [13, p. 133]

$$\rho_1^{\alpha}(\boldsymbol{r}) = \sum_i \langle\delta(\boldsymbol{r}_{\alpha,\,i}-\boldsymbol{r})\rangle \tag{10}$$
$$\rho_2^{\alpha,\,\beta}(\boldsymbol{r},\boldsymbol{r}') = \sum_{i,\,j}{}' \left\langle\delta(\boldsymbol{r}_{\alpha,\,i}-\boldsymbol{r})\delta(\boldsymbol{r}_{\beta,\,j}-\boldsymbol{r}')\right\rangle. \tag{11}$$

**Definition 4** (N-Body Distribution Function [13, p. 133])**.**

$$g_n^{\alpha_1,\,\alpha_2,\,\ldots,\,\alpha_n}(\boldsymbol{r},\,\boldsymbol{r}',\,\ldots,\,\boldsymbol{r}^{(n)}) := \frac{\rho_n^{\alpha_1,\,\alpha_2,\,\ldots,\,\alpha_n}(\boldsymbol{r},\,\boldsymbol{r}',\,\ldots,\,\boldsymbol{r}^{(n)})}{\rho_1^{\alpha_1}(\boldsymbol{r})\rho_1^{\alpha_2}(\boldsymbol{r}')\cdot\ldots\cdot\rho_1^{\alpha_n}(\boldsymbol{r}^{(n)})} \tag{12}$$

Of particular importance is the 2-body (pair) distribution function

$$g_2^{\alpha,\beta}(\boldsymbol{r},\boldsymbol{r}') = \frac{\rho_2^{\alpha,\beta}(\boldsymbol{r},\boldsymbol{r}')}{\rho_1^{\alpha}(\boldsymbol{r})\rho_1^{\beta}(\boldsymbol{r}')}. \tag{13}$$

One can interpret this function as some measure of probability to find a particle next to another one with respect to the chance of finding single particles there at all.

Consider that in the homogeneous case, which will be the only one of interest in the following calculations, the coordinate system can always be transformed in such a way that one of the parameters in the densities and distribution functions can be omitted [7, p. 344 – 345], i.e.

$$\rho_1^{\alpha}(\boldsymbol{r}) = \rho_1^{\alpha} = \frac{N_\alpha}{\Omega} \tag{14}$$

$$\rho_2^{\alpha,\beta}(\boldsymbol{r},\boldsymbol{r}') = \rho_2^{\alpha,\beta}(\boldsymbol{r}-\boldsymbol{r}') \tag{15}$$

$$g_2^{\alpha,\beta}(\boldsymbol{r},\boldsymbol{r}') = g_2^{\alpha,\beta}(\boldsymbol{r}-\boldsymbol{r}') = \frac{\rho_2^{\alpha,\beta}(\boldsymbol{r}-\boldsymbol{r}')}{\rho_1^{\alpha}\rho_1^{\beta}}. \tag{16}$$

**Definition 5** (Weighted Fourier Transform [13, p. 136])**.**

$$\tilde{f}(\boldsymbol{k}) := \mathrm{FT}\left[f(\boldsymbol{r})\right] := \sqrt{\rho_1^{\alpha}\rho_1^{\beta}}\int \mathrm{d}^2 r\; e^{-i\boldsymbol{k}\boldsymbol{r}} f(\boldsymbol{r}) \tag{17}$$

$$f(\boldsymbol{x}) =: \mathrm{FT}^{-1}\left[\tilde{f}(\boldsymbol{k})\right] = \frac{1}{\sqrt{\rho_1^{\alpha}\rho_1^{\beta}}}\frac{1}{(2\pi)^2}\int \mathrm{d}^2 k\; e^{i\boldsymbol{k}\boldsymbol{r}}\tilde{f}(\boldsymbol{k}) \tag{18}$$

**Definition 6** (Static Structure Function [7, p. 350][4, p. 6132][13, p. 133])**.**

$$S^{\alpha,\beta}(\boldsymbol{k}) := \delta_{\alpha,\beta} + \mathrm{FT}\left[g_2^{\alpha,\beta}(\boldsymbol{r}) - 1\right] \tag{19}$$

**Definition 7** (Concrete Diagrams)**.** *Diagrams consist of filled circles, unfilled circles and lines connecting those circles. Each pair of two circles can either be connected by one or by zero lines. Cricles are labeled with two indices, the former one is called colouring, the latter one is called numbering. Each tuple consisting of colour and number has to be unique. These concrete diagrams denote integrals in the following way: Each filled point is an integration variable $\boldsymbol{r}_{\alpha,i}$, with $(\alpha, i)$ being the label of the point. Lines stand for the function $h_2^{\alpha,\beta}(\boldsymbol{r}_{\alpha,i}, \boldsymbol{r}_{\beta,j})$, with $(\alpha, i)$ and $(\beta, j)$ being the labels of the two circles connected by the line. The integrand is the product of all $h_2$-functions generated by lines. unfilled circles denote free variables $\boldsymbol{r}_{\alpha,i}$. The integral is weighted by $\rho_1^{\alpha}$ for each filled point with the colouring $\alpha$. Concrete diagrams can be used in equations, their value equals the value of the corresponding integral.*

*Despite the additional labeling efforts for particle types, these concrete diagrams are identical with those known from literature [6, p. 65 – 66].*

Here is an example of a simple integral written as diagram:

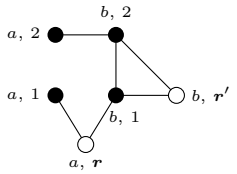


$$= \rho_1^a \rho_1^a \rho_1^b \rho_1^b \int \mathrm{d}^2 r_{a,1} \mathrm{d}^2 r_{a,2} \mathrm{d}^2 r_{b,1} \mathrm{d}^2 r_{b,2} \quad h_2^{a,a}(\boldsymbol{r}_{a,1}, \boldsymbol{r}) h_2^{a,b}(\boldsymbol{r}, \boldsymbol{r}_{b,1})$$

$$\times h_2^{b,b}(\boldsymbol{r}_{b,1}, \boldsymbol{r}') h_2^{b,b}(\boldsymbol{r}', \boldsymbol{r}_{b,2}) h_2^{b,b}(\boldsymbol{r}_{b,1}, \boldsymbol{r}_{b,2}) h_2^{a,b}(\boldsymbol{r}_{a,2}, \boldsymbol{r}_{b,2}) \tag{20}$$

**Definition 8** (Unnumbered Diagrams)**.** *These diagrams can be generated by omitting the numbering of concrete diagrams. Points in unnumbered diagrams are still labeled with the colouring. The value of an unnumbered diagram is equal to $\frac{1}{S}$ times the value of a corresponding concrete diagram, which can be constructed by introducing an arbitrary admissible numbering. $S$ is the order of the subgroup of number, but not colour, permutations leaving the connections unaltered.*

The following example allows 4 different permutations of the numbering without changing the connections. Therefore $S = 4$:

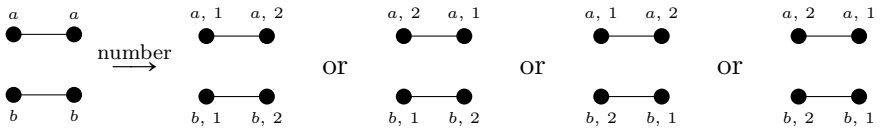


(21)

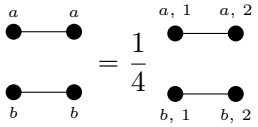


(22)

**Definition 9** (Uncoloured Diagrams)**.** *Uncoloured diagrams are diagrams where the labels of circles are omitted completely. One uncoloured diagram is equal to the sum of all different unnumbered diagrams which can be generated by applying arbitrary colourings to the uncoloured diagram.*

The following example is an uncoloured diagram for $M = 2$. There are 4 different colourings which can be applied on this diagram:

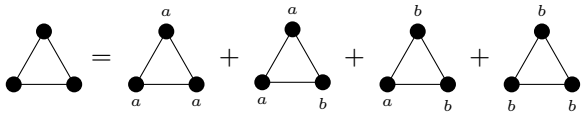


(23)

**Definition 10** (Sum of Diagrams)**.** *Let $G$ be a set of diagrams. Then by $[G]$ we denote the sum of all diagrams in the set $G$.*

# 3 Theory

We start calculating the ground state for a strongly interacting homogeneous many particle system with different particle types using hypernetted-chain Euler-Lagrange (HNC-EL) methods.

## 3.1 Ansatz

The idea is to make an ansatz consisting of an independent particle wave function $\phi_0$ for a weakly interacting model and pair correlations [13, p. 132]

$$\psi_0(\boldsymbol{r}_{a,1},\,\ldots,\,\boldsymbol{r}_{M,N_M}) = \left(\prod_{\alpha,\beta}\prod_{i,j}{}' f_2^{\alpha,\beta}(\boldsymbol{r}_{\alpha,i},\boldsymbol{r}_{\beta,j})\right)^{\frac{1}{2}} \phi_0(\boldsymbol{r}_{a,1},\,\ldots,\,\boldsymbol{r}_{M,N_M}) \tag{24}$$

$$= \underbrace{\exp\left\{\frac{1}{4}\sum_{\alpha,\beta}\sum_{i,j}{}' u_2^{\alpha,\beta}(\boldsymbol{r}_{\alpha,i},\boldsymbol{r}_{\beta,j})\right\}}_{\text{“Jastrow Feenberg form”}} \phi_0(\boldsymbol{r}_{a,1},\,\ldots,\,\boldsymbol{r}_{M,N_M}). \tag{25}$$

Note that in equation (24) the power $\frac{1}{2}$ is added to compensate for the fact that every $f_2^{\alpha,\beta}$ is contributing twice to the product. We assume $\phi_0(\boldsymbol{r}_1,\ldots,\boldsymbol{r}_N)=1$, the simplest possible choice [5, p. 6132 – 6133][8, p. 53]. Some physical information is built into the wave function in advance. Assuming a repulsive potential at small distances, one can conclude that $f_2^{\alpha,\beta}(\boldsymbol{r}_{\alpha,i},\mathbf{r}_{\beta,j})$ has to vanish when $(\alpha=\beta)\wedge|\boldsymbol{r}_i-\boldsymbol{r}_j|\to 0$. Additionally, the wave function should separate when $n_0$ particles (A) are separated from the rest of the system (B).

$$\psi_0(\boldsymbol{r}_{\alpha_1,1},\,\ldots,\,\boldsymbol{r}_{\alpha_i,n_0},\boldsymbol{r}_{\alpha_i,n_0+1},\ldots,\boldsymbol{r}_{\alpha_M,N_M}) = \psi_0^A(\boldsymbol{r}_{\alpha_1,1},\ldots,\boldsymbol{r}_{\alpha_i,n_0})\psi_0^B(\boldsymbol{r}_{\alpha_i,n_0+1},\ldots,\boldsymbol{r}_{\alpha_M,N_M}), \tag{26}$$

thus $|\boldsymbol{r}_{\alpha,i}-\boldsymbol{r}_{\beta,j}|\to\infty$ implies $f_2^{\alpha,\beta}(\boldsymbol{r}_{\alpha,i},\boldsymbol{r}_{\beta,j})\to 1$.

## 3.2 Energy

According to Ritz' variational principle, the ground state can be obtained by minimizing the energy functional [13, p. 133]

$$\forall_{\alpha,\beta}\frac{\delta\left\langle\widehat{\mathcal{H}}\right\rangle}{\delta u_2^{\alpha,\beta}(\boldsymbol{r})} = \frac{\delta}{\delta u_2^{\alpha,\beta}(\boldsymbol{r})}\frac{\left\langle\psi_0\right|\widehat{\mathcal{H}}\left|\psi_0\right\rangle}{\langle\psi_0|\,\psi_0\rangle} = 0 \tag{27}$$

$$\text{with}\quad \widehat{\mathcal{H}} = -\sum_{\alpha}\sum_{i}\frac{\hbar^2}{2m_\alpha}\Delta_{\alpha,i} + \frac{1}{2}\sum_{\alpha,\beta}\sum_{i,j}{}' v_2^{\alpha,\beta}(\boldsymbol{r}_{\alpha,i},\,\boldsymbol{r}_{\beta,j}) \tag{28}$$

$$= \left\langle\widehat{\mathcal{T}}\right\rangle + \left\langle\widehat{\mathcal{V}}\right\rangle. \tag{29}$$

Now let's have a look at the energy in detail, starting with the potential energy part

$$\left\langle\widehat{\mathcal{V}}\right\rangle = \frac{\left\langle\psi_0\right|\widehat{\mathcal{V}}\left|\psi_0\right\rangle}{\langle\psi_0|\,\psi_0\rangle} = \frac{1}{\langle\psi_0|\,\psi_0\rangle}\int \mathrm{d}^{2N}R\,|\psi_0(\boldsymbol{R})|^2\,\frac{1}{2}\sum_{\alpha,\beta}\sum_{i,j}{}' v_2^{\alpha,\beta}(\boldsymbol{r}_{\alpha,i},\,\boldsymbol{r}_{\beta,j}) \tag{30}$$

$$= \frac{1}{2}\sum_{\alpha,\beta}\sum_{i,j}{}'\frac{1}{\langle\psi_0|\,\psi_0\rangle}\int \mathrm{d}^2r\mathrm{d}^2r'\int \mathrm{d}^{2N}R\,|\psi_0(\boldsymbol{R})|^2\,v_2^{\alpha,\beta}(\boldsymbol{r},\,\boldsymbol{r}')\,\delta(\boldsymbol{r}_{\alpha,i}-\boldsymbol{r})\,\delta(\boldsymbol{r}_{\beta,j}-\boldsymbol{r}') \tag{31}$$

$$= \frac{1}{2}\sum_{\alpha,\beta}\int \mathrm{d}^2r\mathrm{d}^2r'\,\rho_2^{\alpha,\beta}(\boldsymbol{r},\,\boldsymbol{r}')v_2^{\alpha,\beta}(\boldsymbol{r},\,\boldsymbol{r}'). \tag{32}$$

In a similar way one can show that

$$\left\langle \widehat{\mathcal{T}} \right\rangle = -\frac{1}{2} \sum_{\alpha,\,\beta} \int \mathrm{d}^2 r \mathrm{d}^2 r' \; \rho_2^{\alpha,\,\beta}(\boldsymbol{r},\,\boldsymbol{r}') \left( \frac{\hbar^2}{8m_\alpha} + \frac{\hbar^2}{8m_\beta} \right) \Delta u_2^{\alpha\,\beta}(\boldsymbol{r} - \boldsymbol{r}'). \tag{33}$$

Summing up the two parts we get

$$E = \left\langle \widehat{\mathcal{H}} \right\rangle = \frac{1}{2} \sum_{\alpha,\,\beta} \int \mathrm{d}^2 r \mathrm{d}^2 r' \; \rho_1^{\alpha} \, \rho_1^{\beta} \, g_2^{\alpha,\,\beta}(\boldsymbol{r},\,\boldsymbol{r}') \underbrace{\left( v_2^{\alpha,\,\beta}(\boldsymbol{r},\,\boldsymbol{r}') - \left( \frac{\hbar^2}{8m_\alpha} + \frac{\hbar^2}{8m_\beta} \right) \Delta u_2^{\alpha\,\beta}(\boldsymbol{r} - \boldsymbol{r}') \right)}_{=: V_{JF}^{\alpha,\,\beta}(\boldsymbol{r},\,\boldsymbol{r}'),\ \text{"Jackson-Feenberg effective interaction"}}. \tag{34}$$

In order to apply the energy minimization (27) on (34), one has to find a relation between $g_2^{\alpha,\,\beta}$ and $u_2^{\alpha,\,\beta}$ [7, p. 345]. It is easily verifiable that this relation is given by

$$g_2^{\alpha,\,\beta}(\boldsymbol{r},\,\boldsymbol{r}') = \frac{1 + \delta_{\alpha,\,\beta}}{\rho_1^{\alpha} \, \rho_1^{\beta}} \frac{\delta \ln \langle \psi_0 |\, \psi_0 \rangle}{\delta u_2^{\alpha,\,\beta}(\boldsymbol{r},\,\boldsymbol{r}')}. \tag{35}$$

### 3.3 Diagrammatic Expansion

Equation (35) suggests to have a second look at the norm of the wave function

$$\langle \psi_0 |\, \psi_0 \rangle = \int \mathrm{d}^{2N} R \; |\psi_0(\boldsymbol{R})|^2 \tag{36}$$

$$= \int \mathrm{d}^{2N} R \; \left( \left( \prod_{\alpha,\,\beta} \prod_{i,\,j}{}' \, f_2^{\alpha,\,\beta}(\boldsymbol{r}_{\alpha,\,i}, \boldsymbol{r}_{\beta,\,j}) \right)^{\frac{1}{2}} \right)^2 \tag{37}$$

$$= \int \mathrm{d}^{2N} R \; \prod_{\alpha} \prod_{i<j} f_2^{\alpha,\,\alpha}(\boldsymbol{r}_{\alpha,\,i}, \boldsymbol{r}_{\alpha,\,j})^2 \prod_{\alpha<\beta} \prod_{i,\,j} f_2^{\alpha,\,\beta}(\boldsymbol{r}_{\alpha,\,i}, \boldsymbol{r}_{\beta,\,j})^2 \tag{38}$$

$$= \int \mathrm{d}^{2N} R \; \prod_{\alpha} \prod_{i<j} (1 + h_2^{\alpha,\,\alpha}(\boldsymbol{r}_{\alpha,\,i}, \boldsymbol{r}_{\alpha,\,j})) \prod_{\alpha<\beta} \prod_{i,\,j} \left( 1 + h_2^{\alpha,\,\beta}(\boldsymbol{r}_{\alpha,\,i}, \boldsymbol{r}_{\beta,\,j}) \right) \tag{39}$$

$$\begin{aligned} = \Omega^N \Bigg\{ & 1 + \frac{N_a(N_a-1)}{2\Omega^2} \int \mathrm{d}^2 r_{a,\,1} \mathrm{d}^2 r_{a,\,2} h_2^{a,\,a}(\boldsymbol{r}_{a,\,1}, \boldsymbol{r}_{a,\,2}) \\ & + \frac{N_b(N_b-1)}{2\Omega^2} \int \mathrm{d}^2 r_{b,\,1} \mathrm{d}^2 r_{b,\,2} h_2^{b,\,b}(\boldsymbol{r}_{b,\,1}, \boldsymbol{r}_{b,\,2}) + \ldots + \frac{N_a N_b}{\Omega^2} \int \mathrm{d}^2 r_{a,\,1} \mathrm{d}^2 r_{b,\,1} h_2^{a,\,b}(\boldsymbol{r}_{a,\,1}, \boldsymbol{r}_{b,\,1}) \\ & + \ldots + \frac{N_a(N_a-1)N_b}{2\Omega^3} \ldots + \ldots \Bigg\} \end{aligned} \tag{40}$$

$$\begin{aligned} \approx \Omega^N \Bigg\{ & 1 + \frac{(\rho_1^a)^2}{2} \int \mathrm{d}^2 r_{a,\,1} \mathrm{d}^2 r_{a,\,2} h_2^{a,\,a}(\boldsymbol{r}_{a,\,1}, \boldsymbol{r}_{a,\,2}) + \frac{(\rho_1^b)^2}{2} \int \mathrm{d}^2 r_{b,\,1} \mathrm{d}^2 r_{b,\,2} h_2^{b,\,b}(\boldsymbol{r}_{b,\,1}, \boldsymbol{r}_{b,\,2}) + \ldots \\ & + \rho_1^a \rho_1^b \int \mathrm{d}^2 r_{a,\,1} \mathrm{d}^2 r_{b,\,1} h_2^{a,\,b}(\boldsymbol{r}_{a,\,1}, \boldsymbol{r}_{b,\,1}) + \ldots \\ & + \frac{(\rho_1^a)^2 \rho_1^b}{2} \ldots + \ldots \Bigg\}. \end{aligned} \tag{41}$$

This series expansion can now be expressed in the language of diagrams[1] and here lies also the motivation to define diagrams with the corresponding coefficients the way they are defined. Note that only diagrams for particle types $a$ and $b$ are shown, the others contribute in a similar way:

[1] A method known from statistical mechanics [6, p. 71 – 74]

$$\langle\psi_0|\,\psi_0\rangle = \Omega^N \Bigg[ 1 + \frac{1}{2}$$  $$+ \frac{1}{2}$$  $$+ 1$$ 

$$+ \frac{1}{2}$$ 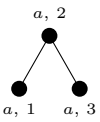 $$+ \frac{1}{2}$$ 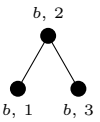 $$+ \frac{1}{2}$$ 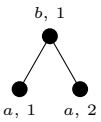 $$+ \frac{1}{2}$$ 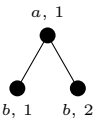 $$+ 1$$ 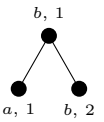 $$+ 1$$ 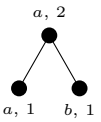

$$+ \frac{1}{8}$$ 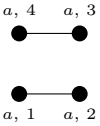 $$+ \frac{1}{8}$$ 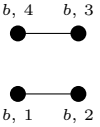 $$+ \frac{1}{4}$$ 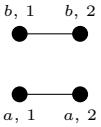 $$+ \frac{1}{2}$$ 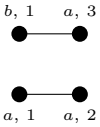 $$+ \frac{1}{2}$$ 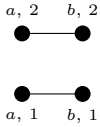 $$+ \frac{1}{2}$$ 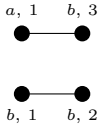

$$+ \frac{1}{6}$$ 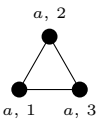 $$+ \frac{1}{6}$$ 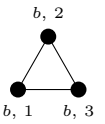 $$+ \frac{1}{2}$$ 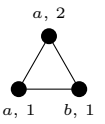 $$+ \frac{1}{2}$$ 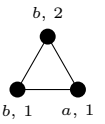 $$+ \dots \Bigg]$$ (42)

Omitting the numbering:

$$\langle\psi_0|\,\psi_0\rangle = \Omega^N \Bigg[ 1 +$$ 

$$+$$ 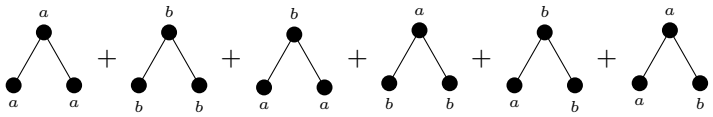

$$+$$ 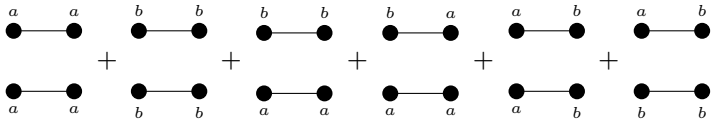

$$+$$ 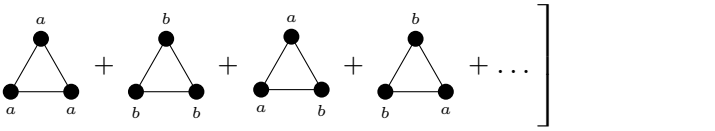 $$+ \dots \Bigg]$$ (43)

Omitting the colouring:

$$\langle\psi_0|\,\psi_0\rangle = \Omega^N \Bigg[ 1 +$$ 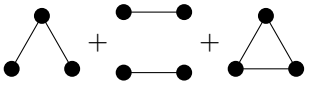 $$+ \dots \Bigg]$$ (44)

Now let's work a little bit on those diagrams.

**Definition 11** (Articulation Points)**.** *An articulation point is a circle in a diagram with the following properties.*

1. *It is a filled circle.*
2. *Removal of that circle causes the diagram to separate into two or more unconnected parts, of which at least one contains no unfilled circle.*

*This definition is identical to the one known in literature [6, p. 67].*

We now show that diagrams in (44) containing articulation points can be neglected exemplarily for 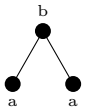

. We make use of translational invariance for that. Note that it can also be done for inhomogeneous systems.

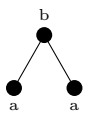

$= \frac{1}{2}$ 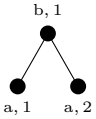

$= \frac{(\rho_1^a)^2\,\rho_1^b}{2} \int \mathrm{d}^2 r_{a,1} \mathrm{d}^2 r_{a,2} \mathrm{d}^2 r_{b,1} \quad h_2^{a,b}(\boldsymbol{r}_{a,1},\, \boldsymbol{r}_{b,1}) h_2^{a,\,b}(\boldsymbol{r}_{a,2},\, \boldsymbol{r}_{b,1})$ (45)

$= \frac{(\rho_1^a)^2\,\rho_1^b}{2} \int \mathrm{d}^2 r_{a,1} \mathrm{d}^2 r_{a,2} \mathrm{d}^2 r_{b,1} \quad h_2^{a,b}(\boldsymbol{r}_{a,1},\, \boldsymbol{r}_{b,1}) h_2^{a,\,b}(\boldsymbol{r}_{a,2} - \boldsymbol{r}_{b,1},\, \boldsymbol{0})$ (46)

$= \frac{1}{\Omega} \frac{(\rho_1^a)^2\,\rho_1^b}{2} \int \mathrm{d}^2 r_{a,1} \mathrm{d}^2 r_{a,2} \mathrm{d}^2 r_{b,1} \mathrm{d}^2 r_{b,2} \quad h_2^{a,b}(\boldsymbol{r}_{a,1},\, \boldsymbol{r}_{b,1}) h_2^{a,\,b}(\boldsymbol{r}_{a,2},\, \boldsymbol{0})$ (47)

$= \frac{1}{\Omega} \frac{(\rho_1^a)^2\,\rho_1^b}{2} \int \mathrm{d}^2 r_{a,1} \mathrm{d}^2 r_{a,2} \mathrm{d}^2 r_{b,1} \mathrm{d}^2 r_{b,2} \quad h_2^{a,b}(\boldsymbol{r}_{a,1},\, \boldsymbol{r}_{b,1}) h_2^{a,\,b}(\boldsymbol{r}_{a,2},\, \boldsymbol{r}_{b,2})$ (48)

$= \frac{1}{2N_b}$ 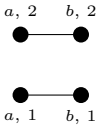

$= \frac{1}{N_b}$ 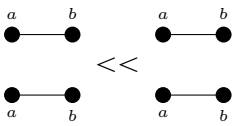

(49)

Hence

$\langle \psi_0 |\, \psi_0 \rangle = \Omega^N \Big[ 1 +$ 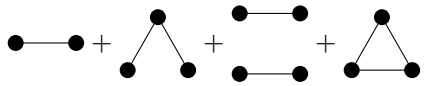 $+ \ldots \Big]$ (50)

$\approx \Omega^N \Big[ 1 +$ 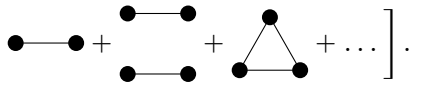 $+ \ldots \Big]$. (51)

Having (35) in mind, we now have to find some way to logarithmize $\langle \psi_0 |\, \psi_0 \rangle$. In the language of diagrams, there is a way to do it.

**Lemma 1** (Exponential Lemma)**.** *Let $G$ be a set of unnumbered diagrams so that there are no unfilled circles in the diagram, and so that for any two circles in the diagram, there exists an arbitrary path of lines connecting them. Let $H$ be the set of all possible products of diagrams in $G$. Then*

$$[H] = \exp\{[G]\} - 1. \tag{52}$$

*Proof.* This lemma has already been proved in literature. The proof from Hansen and McDonald is done for unlabeled diagrams describing single component systems, but is compatible with our definition of diagrams in every single step [6, p. 398 – 399]. □

**Lemma 2.** *Let $A_1$ be a set of uncoloured diagrams with no unfilled circles, and let $A_2$ be the set of all unnumbered diagrams occurring in any of the elements in $A_1$. Let $B_1$ be the set of all possible products of diagrams in $A_1$, and let $B_2$ be the set of all possible products of diagrams in $A_2$. Then*

$$[A_1] = [A_2] \quad \textit{and} \quad [B_1] = [B_2]. \tag{53}$$

*Proof.* $[A_1] = [A_2]$ is obvious, because each uncoloured diagram equals by definition the sum of the diagrams generated from it by applying colouring.

Let $N_1 \in \mathbb{N}$ and $a_{1,1}, a_{1,2}, \ldots, a_{1,N_1}$ be the elements of $A_1$. Each of the $a_{1,i}$ can be decomposed into unnumbered diagrams by applying all possible colourings. Let $(r_1, \ldots, r_{N_1}) \in \mathbb{N}^{N_1}$ and $a_{2,1,1}, \ldots, a_{2,N_1,r_{N_1}} \in A_2$ be so that $\forall_{i \in 1,\ldots,N_1} a_{1,i} = \sum_{j=1}^{r_i} a_{2,i,j}$.

Note that then $A_2 = \bigcup_{i\in\{1,\dots,N_1\}} \bigcup_{j\in\{1,\dots,r_i\}} \{a_{2,i,j}\}$ and $\forall_{i_1,i_2\in\{1,\dots,N_1\}} \forall_{j_1\in\{1,\dots,r_{i_1}\}, j_2\in\{1,\dots,r_{i_2}\}} \{a_{2,i_1,j_1}\} \cap \{a_{2,i_2,j_2}\} = \{\}$.

$$[B_1] = \sum_{b_1\in B_1} b_1 \tag{54}$$

$$= -1 + \sum_{n_1=0}^{\infty} \dots \sum_{n_{N_1}=0}^{\infty} \prod_{i=1}^{N_1} \frac{(a_{1,i})^{n_i}}{n_i!} \tag{55}$$

$$= -1 + \sum_{n_1=0}^{\infty} \dots \sum_{n_{N_1}=0}^{\infty} \prod_{i=1}^{N_1} \frac{\left(\sum_{j=1}^{r_i} a_{2,i,j}\right)^{n_i}}{n_i!} \tag{56}$$

$$= -1 + \sum_{n_1=0}^{\infty} \dots \sum_{n_{N_1}=0}^{\infty} \prod_{i=1}^{N_1} \frac{1}{\cancel{n_i!}} \sum_{k_{i,1}+\dots+k_{i,r_i}=n_i} \frac{\cancel{n_i!}}{k_{i,1}! \cdot \dots \cdot k_{i,r_i}!} \prod_{j=1}^{r_i} (a_{2,i,j})^{k_{i,j}} \tag{57}$$

$$= -1 + \sum_{n_1=0}^{\infty} \dots \sum_{n_{N_1}=0}^{\infty} \prod_{i=1}^{N_1} \sum_{k_{i,1}+\dots+k_{i,r_i}=n_i} \prod_{j=1}^{r_i} \frac{(a_{2,i,j})^{k_{i,j}}}{k_{i,j}!} \tag{58}$$

$$= -1 + \sum_{n_1=0}^{\infty} \dots \sum_{n_{N_1}=0}^{\infty} \sum_{k_{1,1}+\dots+k_{1,r_1}=n_1} \dots \sum_{k_{N_1,1}+\dots+k_{N_1,r_{N_1}}=n_{N_1}} \prod_{i=1}^{N_1} \prod_{j=1}^{r_i} \frac{(a_{2,i,j})^{k_{i,j}}}{k_{i,j}!} \tag{59}$$

$$= -1 + \sum_{k_{1,1}=1}^{\infty} \dots \sum_{k_{N_1,r_{N_1}}=1}^{\infty} \prod_{i=1}^{N_1} \prod_{j=1}^{r_i} \frac{(a_{2,i,j})^{k_{i,j}}}{k_{i,j}!} \tag{60}$$

$$= \sum_{b_2\in B_2} b_2 = [B_2] \tag{61}$$

□

**Theorem 1** (Exponential Theorem)**.** *Let $G$ be a set of (uncoloured) diagrams so that there are no unfilled circles in the diagram, and so that for any two circles in the diagram there exists an arbitrary path of lines connecting them. Let $H$ be the set of all possible products of diagrams in $G$. Then*

$$[H] = \exp\{[G]\} - 1. \tag{62}$$

*Proof.* Apply Lemma 1 and Lemma 2. □

Applying Theorem 1 onto (51) one gets rid of all of the diagrams consisting of unconnected parts:

$$\ln\langle\psi_0|\,\psi_0\rangle = N\ln\Omega +$$ 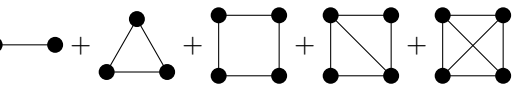 $$+\dots \tag{63}$$

Bringing (35) to mind once again, we need to know how functional derivation works with diagrams.
**Lemma 3** (Variational Derivation of Diagrams [6, p. 69])**.** *Let $q$ be a unnumbered diagram containing no unfilled circles. Then*

$$\frac{\delta q}{\delta h_2^{\alpha,\beta}(\boldsymbol{r},\,\boldsymbol{r}')} = \frac{\rho_1^\alpha \rho_1^\beta}{1+\delta_{\alpha,\beta}} \left[\begin{array}{l} \textit{All diagrams obtained by erasing an } h_2^{\alpha,\beta}\textit{-bond,} \\ \textit{changing the circles that it linked to unfilled ones,} \\ \textit{and labeling them with } (\alpha,\,\boldsymbol{r}) \textit{ and } (\beta,\,\boldsymbol{r}'). \end{array}\right]. \tag{64}$$

*Proof.* Let $S$ be the order of the subgroup of number permutations leaving the connections unaltered. Let $n_a$, $n_b$, …, $n_M$ be the count of filled circles with colour $a$, $b$, …. Then there are $\nu = \frac{n_a! \cdot n_b! \cdot \ldots \cdot n_M!}{S}$ different ways to number all filled circles of the same colour consecutively. Let $q_i$ be those concrete diagrams.[2] Then

$$q = \frac{1}{n_a! \cdot n_b! \cdot \ldots \cdot n_M!} \sum_{i=1}^{\nu} q_i. \tag{65}$$

The functional derivative affects via product rule every $h_2^{\alpha,\beta}(\boldsymbol{r}_{\alpha,i}, \boldsymbol{r}_{\beta,j})$ in the diagram by

$$\frac{\delta h_2^{\alpha,\beta}(\boldsymbol{r}_{\alpha,i}, \boldsymbol{r}_{\beta,j})}{\delta h_2^{\alpha,\beta}(\boldsymbol{r}, \boldsymbol{r}')} = \delta(\boldsymbol{r} - \boldsymbol{r}_{\alpha,i})\, \delta(\boldsymbol{r}' - \boldsymbol{r}_{\beta,j}) \tag{66}$$

effectively creating a sum of diagrams with another $h_2$ - bond of $q_i$ replaced by $\delta(\boldsymbol{r} - \boldsymbol{r}_{\alpha,i})\, \delta(\boldsymbol{r}' - \boldsymbol{r}_{\beta,j})$ in every contributing summand. These delta functions change the corresponding filled circles to unfilled ones labeled with $(\alpha, \boldsymbol{r})$ and $(\beta, \boldsymbol{r}')$ by elimination of the integration variables and causes the point weightings $\rho_1^\alpha$ and $\rho_1^\beta$ to factor out of the diagram

$$\frac{\delta q}{\delta h_2^{\alpha,\beta}(\boldsymbol{r}, \boldsymbol{r}')} = \begin{cases} \rho_1^\alpha \rho_1^\beta \frac{1}{n_a! \cdot n_b! \cdot \ldots \cdot n_M!} \sum_{i=1}^{\nu} \frac{1}{2} \sum_{i<j}^{n_i, n_i} q_i^{(j,k)} & \text{if } \alpha = \beta \\ \rho_1^\alpha \rho_1^\beta \frac{1}{n_a! \cdot n_b! \cdot \ldots \cdot n_M!} \sum_{i=1}^{\nu} \sum_{j=1}^{n_i} \sum_{k=1}^{n_i} q_i^{(j,k)} & \text{if } \alpha \neq \beta \end{cases} \tag{67}$$

$$= \rho_1^\alpha \rho_1^\beta \frac{1}{n_a! \cdot n_b! \cdot \ldots \cdot n_M!} \sum_{i=1}^{\nu} \frac{1}{1 + \delta_{\alpha,\beta}} \sum_{j=1}^{n_i} \sum_{k=1}^{n_i}{}' q_i^{(j,k)}, \tag{68}$$

where $q_i^{(j,k)}$ denotes $q_i$ removing $h_2^{\alpha,\beta}(\boldsymbol{r}_{\alpha,j}, \boldsymbol{r}_{\beta,k})$. Furthermore

$$\frac{\delta q}{\delta h_2^{\alpha,\beta}(\boldsymbol{r}, \boldsymbol{r}')} = \frac{\rho_1^\alpha \rho_1^\beta}{1 + \delta_{\alpha,\beta}} \cdot \frac{1}{n_a! \cdot \ldots \cdot (n_\alpha - 1 - \delta_{\alpha,\beta})! \cdot \ldots \cdot ((1 - \delta_{\alpha\beta})(n_\beta - 1))! \cdot \ldots \cdot n_M!} \sum_{i=1}^{\nu} q_i^{(1,2)}. \tag{69}$$

These diagrams can now be divided into $\mu$ groups of diagrams being connected exactly the same way

$$\frac{\delta q}{\delta h_2^{\alpha,\beta}(\boldsymbol{r}, \boldsymbol{r}')} = \frac{\rho_1^\alpha \rho_1^\beta}{1 + \delta_{\alpha,\beta}} \sum_{i=1}^{\mu} q_i' \tag{70}$$

$$= \frac{\rho_1^\alpha \rho_1^\beta}{1 + \delta_{\alpha,\beta}} \left[ \begin{array}{l} \text{All diagrams obtained by erasing an } h_2^{\alpha,\beta}\text{-bond,} \\ \text{changing the circles that it linked to unfilled ones,} \\ \text{and labeling them with } (\alpha, \boldsymbol{r}) \text{ and } (\beta, \boldsymbol{r}'). \end{array} \right]. \tag{71}$$

□

E.g.

$$\frac{\delta}{\delta h_2^{a,a}(\boldsymbol{r}, \boldsymbol{r}')} \quad \begin{array}{ccc} & \text{a} & \\ \text{a} & & \text{a} \end{array} \quad = \frac{(\rho_1^a)^2}{2} \quad \begin{array}{ccc} & \text{a} & \\ a, \boldsymbol{r} & & a, \boldsymbol{r}' \end{array} . \tag{72}$$

[2] When $\Gamma$ is the group of number permutations and $\Gamma'$ is the subgroup of $\Gamma$ leaving the connections unaltered, then $S = |\Gamma'|$ and $n_a! \cdot n_b! \cdot \ldots \cdot n_M! = |\Gamma|$. There are $\nu$ cosets of $\Gamma'$ in $\Gamma$, all of them but one changing the connections. Note that those cosets generally are not a group on their own. $\nu$ is then the index of $\Gamma'$ in $\Gamma$ and by Lagrange's theorem $\nu = \frac{|\Gamma|}{|\Gamma'|}$. Let R be a system of distinct representatives of those cosets. Applying an arbitrary admissible numbering onto $q$ to get a starting point, the $q_i$ can now be generated by applying the different permutations in R onto the labels of the starting diagram.

**Theorem 2** (Variational Derivation of Diagrams)**.** *Let $g$ be a uncoloured diagram containing no unfilled circles. Then*

$$\frac{\delta g}{\delta h_2^{\alpha,\beta}(\boldsymbol{r},\,\boldsymbol{r}')} = \frac{\rho_1^\alpha \rho_1^\beta}{1+\delta_{\alpha,\beta}} \left[ \begin{array}{l} \textit{All diagrams obtained by erasing an } h_2^{\alpha,\beta}\textit{-bond,} \\ \textit{changing the circles that it linked to unfilled ones,} \\ \textit{and labeling them with } (\alpha,\boldsymbol{r}) \textit{ and } (\beta,\boldsymbol{r}'). \end{array} \right]. \tag{73}$$

*Proof.* Write $g$ as a sum of unnumbered diagrams $g_i$. Apply lemma 3 on each $g_i$. Rewrite the sum of unnumbered diagrams provided by the lemma as a sum of uncoloured diagrams. □

Working a little more on the diagrammatic expansion

$$g_2^{\alpha,\beta}(\boldsymbol{r},\,\boldsymbol{r}') = \frac{2}{\rho_1^\alpha\,\rho_1^\beta} \frac{\delta \ln \langle\psi_0|\,\psi_0\rangle}{\delta u_2^{\alpha,\beta}(\boldsymbol{r},\,\boldsymbol{r}')} \tag{74}$$

$$= \frac{2}{\rho_1^\alpha\,\rho_1^\beta} \int \mathrm{d}^2 r'' \mathrm{d}^2 r''' \quad \frac{\delta h_2^{\alpha,\beta}(\boldsymbol{r}'',\,\boldsymbol{r}''')}{\delta u_2^{\alpha,\beta}(\boldsymbol{r},\,\boldsymbol{r}')} \frac{\delta \ln \langle\psi_0|\,\psi_0\rangle}{\delta h_2^{\alpha,\beta}(\boldsymbol{r}'',\,\boldsymbol{r}''')} \tag{75}$$

$$= \frac{2}{\rho_1^\alpha\,\rho_1^\beta} \underbrace{\exp\left\{u_2^{\alpha,\beta}(\boldsymbol{r},\,\boldsymbol{r}')\right\}}_{f_2^{\alpha,\beta}(\boldsymbol{r},\boldsymbol{r}')^2} \frac{\delta}{\delta h_2^{\alpha,\beta}(\boldsymbol{r},\,\boldsymbol{r}')} \Big[ N \ln\Omega + \text{●—●} + \text{△} + \text{□} + \ldots \Big] \tag{76}$$

and finally applying theorem 2:

$$g_2^{\alpha,\beta}(\boldsymbol{r},\,\boldsymbol{r}') = f_2^{\alpha,\beta}(\boldsymbol{r},\,\boldsymbol{r}')^2 \Big[ 1 + \text{○}_{\alpha,\,\boldsymbol{r}}\text{○}_{\beta,\,\boldsymbol{r}'} + \text{○}_{\alpha,\,\boldsymbol{r}}\text{○}_{\beta,\,\boldsymbol{r}'} + \text{○}_{\alpha,\,\boldsymbol{r}}\text{○}_{\beta,\,\boldsymbol{r}'} + \text{○}_{\alpha,\,\boldsymbol{r}}\text{○}_{\beta,\,\boldsymbol{r}'} + \ldots \Big]. \tag{77}$$

(77) is the final form of the diagrammatic expansion. Note that in the contributing diagrams the unfilled circles are always connected in some way but never directly. This is the case because we eliminated diagrams with articulation points beforehand.

Now we have a closer look at the diagrams and find two different classes of them.

**Definition 12** (Nodal and Non-Nodal Diagrams [6, p. 67][8, p. 66])**.** *An uncoloured diagram is nodal iff*

1. *There are exactly two unfilled circles in the diagram:* $(\alpha,\,\boldsymbol{r})$ *and* $(\beta,\,\boldsymbol{r}')$.
2. *There is at least one connection line in the diagram.*
3. *The unfilled circles are not directly connected.*
4. *All paths connecting these two unfilled circles have to go through one single filled circle.*

*An uncoloured diagram is non-nodal iff*

1. *There are exactly two unfilled circles in the diagram:* $(\alpha,\,\boldsymbol{r})$ *and* $(\beta,\,\boldsymbol{r}')$.
2. *There is at least one connection line in the diagram.*
3. *The diagram is not nodal.*

$N^{\alpha,\beta}(\boldsymbol{r},\,\boldsymbol{r}')$ *is the sum of all nodal diagrams,* $X^{\alpha,\beta}(\boldsymbol{r},\,\boldsymbol{r}')$ *is the sum of all non-nodal diagrams.*

E.g.[3]

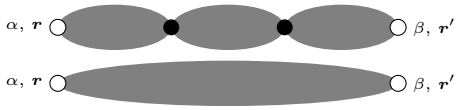


is nodal, (78)

is non-nodal. (79)

Now we have aquired the means to deduce three important equations from the diagrammatic expansion, the central equations of HNC-EL theory. Those are crucial to solve the problem.

## 3.4 Separation into nodal and non-nodal Diagrams

We insert $f_2^{\alpha,\beta}(\boldsymbol{r},\boldsymbol{r}')^2 = h_2^{\alpha,\beta}(\boldsymbol{r},\boldsymbol{r}') + 1$ into the expansion (77) and observe that the factor $h_2$ can be multiplied into the diagrams adding a line between the unfilled circles

$$g_2^{\alpha,\beta}(\boldsymbol{r},\boldsymbol{r}') = \Big(h_2^{\alpha,\beta}(\boldsymbol{r},\boldsymbol{r}')+1\Big)\left[1 + \quad + \quad + \quad + \quad + \ldots\right] \tag{80}$$

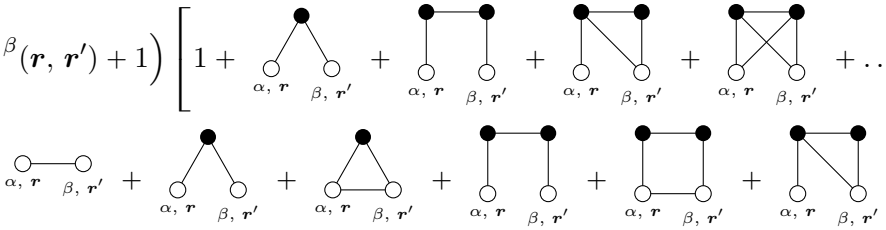


$$= 1 + \quad + \quad + \quad + \quad + \quad + \quad + \ldots. \tag{81}$$




We observe that all diagrams in the series contain two unfilled circles, and there is at least one line in each diagram. So [13, p. 136]

$$g_2^{\alpha,\beta}(\boldsymbol{r},\boldsymbol{r}') - 1 = N^{\alpha,\beta}(\boldsymbol{r},\boldsymbol{r}') + X^{\alpha,\beta}(\boldsymbol{r},\boldsymbol{r}'). \tag{82}$$

## 3.5 Ornstein-Zernike Relation

There is a relationship between the sum of all nodal diagrams and the sum of all non-nodal ones in form of chaining up non-nodal diagrams to construct nodal ones [5, p. 2178][13, p. 136]

$$N^{\alpha,\beta}(\boldsymbol{r},\boldsymbol{r}') = \quad + \quad + \quad + \quad + \ldots \quad . \tag{83}$$

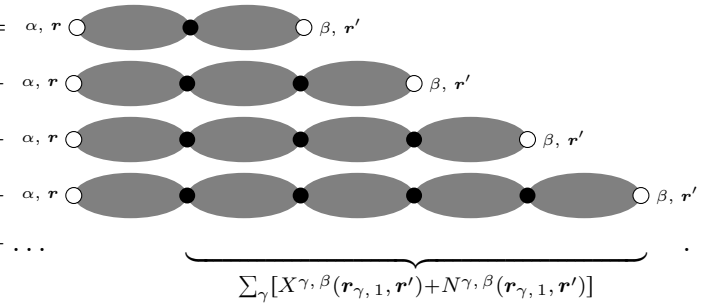


If this series is cut through at the first nodal point on the left side, then on the right side there are again all the nodal diagrams, but note that those are nodal diagrams with all possible colourings of the first unfilled circle, hence $\sum_\gamma$ must be added. Hence

$$N^{\alpha,\beta}(\boldsymbol{r},\boldsymbol{r}') = \sum_\gamma \rho_1^\gamma \int \mathrm{d}^2 r_{\gamma,1}\, X^{\alpha,\gamma}(\boldsymbol{r},\boldsymbol{r}_{\gamma,1})\Big[X^{\gamma,\beta}(\boldsymbol{r}_{\gamma,1},\boldsymbol{r}') + N^{\gamma,\beta}(\boldsymbol{r}_{\gamma,1},\boldsymbol{r}')\Big] \tag{84}$$

$$\sqrt{\rho_1^\alpha \rho_1^\beta} N^{\alpha,\beta}(\boldsymbol{r},\boldsymbol{r}') = \sum_\gamma \sqrt{\rho_1^\gamma \rho_1^\gamma} \int \mathrm{d}^2 r_{\gamma,1}\, X^{\alpha,\gamma}(\boldsymbol{r},\boldsymbol{r}_{\gamma,1}) \sqrt{\rho_1^\alpha \rho_1^\beta}\Big[g_2^{\gamma,\beta}(\boldsymbol{r}_{\gamma,1},\boldsymbol{r}') - 1\Big]. \tag{85}$$

[3] The grey ellipses stand for an arbitrary complex network of filled circles and lines connecting the two points the ellipses end in. The network only has to be sufficiently complex that there are no further nodal points in it.

Formulating the equation in Fourier space and introducing a matrix representation to make up for the particle type indexing

$$\tilde{N}^{\alpha,\beta}(\boldsymbol{k}) = \sum_{\gamma} \tilde{X}^{\alpha,\gamma}(\boldsymbol{k}) \left[ S^{\gamma,\beta}(\boldsymbol{k}) - \delta_{\gamma,\beta} \right] \tag{86}$$

$$= \sum_{\gamma} \tilde{X}^{\alpha,\gamma}(\boldsymbol{k}) S^{\gamma,\beta}(\boldsymbol{k}) - \tilde{X}^{\alpha,\beta}(\boldsymbol{k}) \tag{87}$$

$$\tilde{\boldsymbol{N}}(\boldsymbol{k}) = \tilde{\boldsymbol{X}}(\boldsymbol{k}).\boldsymbol{S}(\boldsymbol{k}) - \tilde{\boldsymbol{X}}(\boldsymbol{k}) = \tilde{\boldsymbol{X}}(\boldsymbol{k}).\left(\boldsymbol{S}(\boldsymbol{k}) - \mathbf{1}\right). \tag{88}$$

Equation (88) is known as Ornstein-Zernike relation.

## 3.6 Hypernetted-Chain Equation

Starting from the final formulation of the diagrammatic expansion (77) again, we can divide the diagrams again into two different classes.

**Definition 13** (Composite and Simple Diagrams [8, p. 68])**.** *An uncoloured diagram is called composite iff*

1. *There are exactly two unfilled circles in the diagram:* $(\alpha, \boldsymbol{r})$ *and* $(\beta, \boldsymbol{r}')$*.*
2. *There is at least one connection line in the diagram.*
3. *The diagram can be written as a product of two other diagrams, none of them being unity.*

*An uncoloured diagram is simple iff*

1. *There are exactly two unfilled circles in the diagram:* $(\alpha, \boldsymbol{r})$ *and* $(\beta, \boldsymbol{r}')$*.*
2. *The diagram is not composite.*

$C^{\alpha,\beta}(\boldsymbol{r}, \boldsymbol{r}')$ *is the sum of all composite diagrams,* $S^{\alpha,\beta}(\boldsymbol{r}, \boldsymbol{r}')$ *is the sum of all simple diagrams.*

Using the exponential theorem (theorem 1) once again and making use of the fact that all composite diagrams can be written as products of non-composite diagrams, one gets

$$S^{\alpha,\beta}(\boldsymbol{r}, \boldsymbol{r}') + C^{\alpha,\beta}(\boldsymbol{r}, \boldsymbol{r}') = \exp\left\{ S^{\alpha,\beta}(\boldsymbol{r}, \boldsymbol{r}') \right\} - 1. \tag{89}$$

Each of the diagrams in (77) is either composite or non-composite. So we can write

$$g_2^{\alpha,\beta}(\boldsymbol{r}, \boldsymbol{r}') = f_2^{\alpha,\beta}(\boldsymbol{r}, \boldsymbol{r}')^2 \left[ 1 + S^{\alpha,\beta}(\boldsymbol{r}, \boldsymbol{r}') + C^{\alpha,\beta}(\boldsymbol{r}, \boldsymbol{r}') \right] \tag{90}$$

$$= f_2^{\alpha,\beta}(\boldsymbol{r}, \boldsymbol{r}')^2 \exp\left\{ S^{\alpha,\beta}(\boldsymbol{r}, \boldsymbol{r}') \right\} \tag{91}$$

$$= \exp\left\{ u_2^{\alpha,\beta}(\boldsymbol{r}, \boldsymbol{r}') + S^{\alpha,\beta}(\boldsymbol{r}, \boldsymbol{r}') \right\}. \tag{92}$$

$S^{\alpha,\beta}(\boldsymbol{r}, \boldsymbol{r}')$ can now be decomposed into two classes once more. Some of them are nodal and some of them are non-nodal. The latter we call "elementary".

**Definition 14** (Elementary Diagrams [8, p. 69])**.** *An uncoloured diagram is called elementary iff*

1. *There are exactly two unfilled circles in the diagram:* $(\alpha, \boldsymbol{r})$ *and* $(\beta, \boldsymbol{r}')$*.*
2. *There is at least one connection line in the diagram.*
3. *The diagram is simple and non-nodal.*

$E^{\alpha,\beta}(\boldsymbol{r}, \boldsymbol{r}')$ *is the sum of all elementary diagrams.*

We get

$$g_2^{\alpha,\beta}(\boldsymbol{r},\boldsymbol{r}') = \exp\left\{u_2^{\alpha,\beta}(\boldsymbol{r},\boldsymbol{r}') + N^{\alpha,\beta}(\boldsymbol{r},\boldsymbol{r}') + E^{\alpha,\beta}(\boldsymbol{r},\boldsymbol{r}')\right\}, \tag{93}$$

the so-called hypernetted-chain equation [4, p. 6132].

## 3.7 Optimization

With (82), (88) and (93) we now have three important equations which will be used excessively henceforth, they are the tools to finally solve the problem. We start minimizing energy just as proposed in (27). The connection between $u_2$ and $g_2$ is known, but instead of minimizing with respect to $u_2$ we could minimize with respect to $g_2$ just as well, and this is what we'll do

$$\forall_{\alpha,\beta}\frac{\delta E}{\delta g_2^{\alpha,\beta}(\boldsymbol{r})} = 0. \tag{94}$$

The expression for energy we take from (34)

$$0 = \frac{\delta}{\delta g_2^{\alpha,\beta}(\boldsymbol{r})}\cancel{\frac{1}{2}}\sum_{\gamma,\kappa}\int \mathrm{d}^2r'\ \rho_1^\gamma\,\rho_1^\kappa\, g_2^{\gamma,\kappa}(\boldsymbol{r}')\left(v_2^{\gamma,\kappa}(\boldsymbol{r}') - \left(\frac{\hbar^2}{8m_\gamma}+\frac{\hbar^2}{8m_\kappa}\right)\Delta' u_2^{\gamma\,\kappa}(\boldsymbol{r}')\right). \tag{95}$$

Use the hypernetted-chain equation (93) to replace $u_2$ in (95)

$$\begin{aligned} 0 = v_2^{\alpha,\beta}(\boldsymbol{r}) &- \sum_{\gamma,\kappa}\frac{\rho_1^\gamma\,\rho_1^\kappa}{\rho_1^\alpha\,\rho_1^\beta}\int \mathrm{d}^2r'\ \left(\frac{\hbar^2}{8m_\gamma}+\frac{\hbar^2}{8m_\kappa}\right)\frac{\delta}{\delta g_2^{\alpha,\beta}(\boldsymbol{r})}\, g_2^{\gamma,\kappa}(\boldsymbol{r}')\Delta' \ln\, g_2^{\gamma,\kappa}(\boldsymbol{r}') \\ &+ \underbrace{\sum_{\gamma,\kappa}\frac{\rho_1^\gamma\,\rho_1^\kappa}{\rho_1^\alpha\,\rho_1^\beta}\int \mathrm{d}^2r'\ \left(\frac{\hbar^2}{8m_\gamma}+\frac{\hbar^2}{8m_\kappa}\right)\frac{\delta}{\delta g_2^{\alpha,\beta}(\boldsymbol{r})}\, g_2^{\gamma,\kappa}(\boldsymbol{r}')\Delta'\left[N^{\gamma,\kappa}(\boldsymbol{r}')+E^{\gamma,\kappa}(\boldsymbol{r}')\right]}_{=:w_I^{\alpha,\beta}(\boldsymbol{r})}. \end{aligned} \tag{96}$$

Start with working on the first term, leaving the second term unchanged, and replacing it with $w_I^{\alpha,\beta}(\boldsymbol{r})$ for the time being

$$\begin{aligned} 0 &= v_2^{\alpha,\beta}(\boldsymbol{r}) + w_I^{\alpha,\beta}(\boldsymbol{r}) - \sum_{\gamma,\kappa}\left(\frac{\hbar^2}{8m_\gamma}+\frac{\hbar^2}{8m_\kappa}\right) \\ &\qquad\times\int \mathrm{d}^2r'\ \delta_{\alpha,\gamma}\delta_{\beta,\kappa}\delta(\boldsymbol{r}-\boldsymbol{r}')\Delta' \ln\, g_2^{\gamma,\kappa}(\boldsymbol{r}') + g_2^{\gamma,\kappa}(\boldsymbol{r}')\Delta'\left(\frac{1}{g_2^{\gamma,\kappa}(\boldsymbol{r}')}\delta_{\alpha,\gamma}\delta_{\beta,\kappa}\delta(\boldsymbol{r}-\boldsymbol{r}')\right) \qquad (97) \\ &= v_2^{\alpha,\beta}(\boldsymbol{r}) + w_I^{\alpha,\beta}(\boldsymbol{r}) - \left(\frac{\hbar^2}{8m_\alpha}+\frac{\hbar^2}{8m_\beta}\right)\left(\Delta \ln\, g_2^{\alpha,\beta}(\boldsymbol{r}) + \frac{1}{g_2^{\alpha,\beta}(\boldsymbol{r})}\Delta\, g_2^{\alpha,\beta}(\boldsymbol{r})\right) \qquad (98) \\ &= v_2^{\alpha,\beta}(\boldsymbol{r}) + w_I^{\alpha,\beta}(\boldsymbol{r}) - \frac{1}{\sqrt{g_2^{\alpha,\beta}(\boldsymbol{r})}}\left(\frac{\hbar^2}{2m_\alpha}+\frac{\hbar^2}{2m_\beta}\right)\Delta\sqrt{g_2^{\alpha,\beta}(\boldsymbol{r})}. \qquad (99) \end{aligned}$$

The second part, $w_I^{\alpha,\beta}(\boldsymbol{r})$, is a little bit more tricky. In a first step, we neglect the contribution of elementary diagrams, putting in the second approximation into this theory after restricting the wave function to pair correlations [8, p. 71 – 72]. We'll also make use of the relation $g_2^{\alpha,\beta}(\boldsymbol{r}) = g_2^{\beta,\alpha}(-\boldsymbol{r})$, a

relation following from the fact that reordering arguments in $v_2^{\alpha,\beta}(\boldsymbol{r},\boldsymbol{r}')$ does not change the system

$$w_I^{\alpha,\beta}(\boldsymbol{r}) = \sum_{\gamma,\kappa}\left(\frac{\hbar^2}{8m_\gamma}+\frac{\hbar^2}{8m_\kappa}\right)\frac{\rho_1^\gamma\,\rho_1^\kappa}{\rho_1^\alpha\,\rho_1^\beta}\int \mathrm{d}^2r'\;\frac{\delta}{\delta g_2^{\alpha,\beta}(\boldsymbol{r})}\,(g_2^{\gamma,\kappa}(\boldsymbol{r}')-1)\Delta' N^{\gamma,\kappa}(\boldsymbol{r}') \tag{100}$$

$$= \sum_{\gamma,\kappa}\left(\frac{\hbar^2}{8m_\gamma}+\frac{\hbar^2}{8m_\kappa}\right)\frac{\sqrt{\rho_1^\gamma\,\rho_1^\kappa}}{\rho_1^\alpha\,\rho_1^\beta}\int \mathrm{d}^2r'\;\frac{\delta}{\delta g_2^{\alpha,\beta}(\boldsymbol{r})}\,(g_2^{\gamma,\kappa}(\boldsymbol{r}')-1)\frac{1}{(2\pi)^2}$$
$$\times\int \mathrm{d}^2k\;\exp\left\{i\boldsymbol{k}\boldsymbol{r}'\right\}\mathrm{FT}\left[\Delta' N^{\gamma,\kappa}(\boldsymbol{r}')\right] \tag{101}$$

$$= \sum_{\gamma,\kappa}\left(\frac{\hbar^2}{8m_\gamma}+\frac{\hbar^2}{8m_\kappa}\right)\frac{\sqrt{\rho_1^\gamma\,\rho_1^\kappa}}{\rho_1^\alpha\,\rho_1^\beta}\frac{\delta}{\delta g_2^{\alpha,\beta}(\boldsymbol{r})}\frac{1}{(2\pi)^2}$$
$$\times\int \mathrm{d}^2k\;\mathrm{FT}\left[\Delta N^{\gamma,\kappa}(\boldsymbol{r}')\right]\underbrace{\int \mathrm{d}^2r'\;\exp\left\{-i\boldsymbol{k}\boldsymbol{r}'\right\}\,(\underbrace{g_2^{\gamma,\kappa}(-\boldsymbol{r}')}_{g_2^{\kappa,\gamma}(+\boldsymbol{r}')}-1)}_{\mathrm{FT}\left[g_2^{\kappa,\gamma}(+\boldsymbol{r}')-1\right]}\,. \tag{102}$$

Some simple consequences of (82) and (88) are

$$\tilde{\boldsymbol{X}}(\boldsymbol{k}) = \mathbf{1}-\boldsymbol{S}(\boldsymbol{k})^{-1}, \tag{103}$$

$$\tilde{\boldsymbol{N}}(\boldsymbol{k}) = \boldsymbol{S}(\boldsymbol{k}).\left[\mathbf{1}-\boldsymbol{S}(\boldsymbol{k})^{-1}\right]^2 = \boldsymbol{S}(\boldsymbol{k})+\boldsymbol{S}(\boldsymbol{k})^{-1}-2\,\mathbf{1}. \tag{104}$$

Inserting (104) into (102) yields

$$w_I^{\alpha,\beta}(\boldsymbol{r}) = -\frac{\delta}{\delta g_2^{\alpha,\beta}(\boldsymbol{r})}\frac{1}{(2\pi)^2}\int \mathrm{d}^2k\;\sum_{\gamma,\kappa}\left(\frac{\hbar^2}{8m_\gamma}+\frac{\hbar^2}{8m_\kappa}\right)\frac{1}{\rho_1^\alpha\,\rho_1^\beta}k^2\left(\boldsymbol{S}(\boldsymbol{k})+\boldsymbol{S}(\boldsymbol{k})^{-1}-2\,\mathbf{1}\right)^{\gamma,\kappa}(\boldsymbol{S}(\boldsymbol{k})-\mathbf{1})^{\kappa,\gamma} \tag{105}$$

$$= -\frac{1}{(2\pi)^2}\int \mathrm{d}^2k\;\mathrm{d}^2k'\;\sum_{\gamma,\kappa}\left(\frac{\hbar^2}{8m_\gamma}+\frac{\hbar^2}{8m_\kappa}\right)\frac{1}{\rho_1^\alpha\,\rho_1^\beta}k^2$$
$$\times\frac{\delta}{\delta S^{\alpha,\beta}(\boldsymbol{k}')}\left(S^{\gamma,\kappa}(\boldsymbol{k})S^{\kappa,\gamma}(\boldsymbol{k})-3S^{\gamma,\kappa}(\boldsymbol{k})\delta_{\gamma,\kappa}-\left(\boldsymbol{S}^{-1}(\boldsymbol{k})\right)^{\gamma,\kappa}\delta_{\gamma,\kappa}\right)\frac{\delta S^{\alpha,\beta}(\boldsymbol{k}')}{\delta g_2^{\alpha,\beta}(\boldsymbol{r})}. \tag{106}$$

Expressing $S$ in terms of $g_2$ through the Fourier transform, one can observe that

$$\frac{\delta S^{\alpha,\beta}(\boldsymbol{k}')}{\delta g_2^{\alpha,\beta}(\boldsymbol{r})} = \exp\left\{-i\boldsymbol{k}'\boldsymbol{r}\right\}\sqrt{\rho_1^\alpha\rho_1^\beta}. \tag{107}$$

Inserting (107) into (106) one gets

$$w_I^{\alpha,\beta}(\boldsymbol{r}) = -\frac{1}{(2\pi)^2}\int \mathrm{d}^2k\;\mathrm{d}^2k'\;\sum_{\gamma,\kappa}k^2\left(\frac{\hbar^2}{8m_\gamma}+\frac{\hbar^2}{8m_\kappa}\right)\frac{1}{\sqrt{\rho_1^\alpha\,\rho_1^\beta}}$$
$$\times\frac{\delta}{\delta S^{\alpha,\beta}(\boldsymbol{k}')}\left(S^{\gamma,\kappa}(\boldsymbol{k})S^{\kappa,\gamma}(\boldsymbol{k})-3S^{\gamma,\kappa}(\boldsymbol{k})\delta_{\gamma,\kappa}-\left(\boldsymbol{S}^{-1}(\boldsymbol{k})\right)^{\gamma,\kappa}\delta_{\gamma,\kappa}\right)\exp\left\{-i\boldsymbol{k}'\boldsymbol{r}\right\}. \tag{108}$$

With a system of only one or two particle types, one could do the functional derivation of $\boldsymbol{S}(\boldsymbol{k})^{-1}$ in (108) by actually inserting formulas for matrix inversion [5, 3178]. However, for the general case look at $\mathbf{1}=\boldsymbol{S}(\boldsymbol{k}).\boldsymbol{S}(\boldsymbol{k})^{-1}$, do the functional derivation on both sides and observe that

$$\frac{\delta}{\delta S^{\alpha,\beta}(\boldsymbol{k}')}\left(\boldsymbol{S}^{-1}(\boldsymbol{k})\right)^{\gamma,\kappa} = -\left(\boldsymbol{S}^{-1}(\boldsymbol{k})\right)^{\gamma,\alpha}\left(\boldsymbol{S}^{-1}(\boldsymbol{k})\right)^{\beta,\kappa}\delta(\boldsymbol{k}-\boldsymbol{k}'). \tag{109}$$

Using (109) one gets

$$w_I^{\alpha,\beta}(\boldsymbol{r}) = -\frac{1}{(2\pi)^2}\int \mathrm{d}^2k\ \exp\left\{-i\boldsymbol{k}'\boldsymbol{r}\right\} k^2 \frac{1}{\sqrt{\rho_1^\alpha\,\rho_1^\beta}}\left[\left(2S^{\beta,\alpha}(\boldsymbol{k})-3\delta_{\alpha,\beta}\right)\left(\frac{\hbar^2}{8m_\alpha}+\frac{\hbar^2}{8m_\beta}\right)\right.$$
$$\left.+\sum_\gamma \left(\boldsymbol{S}^{-1}(\boldsymbol{k})\right)^{\gamma,\alpha}\left(\boldsymbol{S}^{-1}(\boldsymbol{k})\right)^{\beta,\gamma}\frac{\hbar^2}{4m_\gamma}\right] \tag{110}$$
$$= -\frac{1}{(2\pi)^2}\int \mathrm{d}^2k\ \exp\left\{i\boldsymbol{k}'\boldsymbol{r}\right\} k^2 \frac{1}{\sqrt{\rho_1^\alpha\,\rho_1^\beta}}\left[\left(2S^{\alpha,\beta}(\boldsymbol{k})-3\delta_{\alpha,\beta}\right)\left(\frac{\hbar^2}{8m_\alpha}+\frac{\hbar^2}{8m_\beta}\right)\right.$$
$$\left.+\sum_\gamma \left(\boldsymbol{S}^{-1}(\boldsymbol{k})\right)^{\alpha,\gamma}\left(\boldsymbol{S}^{-1}(\boldsymbol{k})\right)^{\gamma,\beta}\frac{\hbar^2}{4m_\gamma}\right] \tag{111}$$
$$= \mathrm{FT}^{-1}\left[-\left[\left(2S^{\alpha,\beta}(\boldsymbol{k})-3\delta_{\alpha,\beta}\right)\left(\frac{\hbar^2k^2}{8m_\alpha}+\frac{\hbar^2k^2}{8m_\beta}\right)+\sum_\gamma\left(\boldsymbol{S}^{-1}(\boldsymbol{k})\right)^{\alpha,\gamma}\left(\boldsymbol{S}^{-1}(\boldsymbol{k})\right)^{\gamma,\beta}\frac{\hbar^2k^2}{4m_\gamma}\right]\right]. \tag{112}$$

## 3.8 Formulation in x-Space

**Definition 15** (Kinetic Energy Matrix)**.**

$$T^{\alpha,\beta}(\boldsymbol{k}) := \left(\frac{\hbar^2k^2}{4m_\alpha}+\frac{\hbar^2k^2}{4m_\beta}\right)\delta_{\alpha,\beta} \tag{113}$$

Reformulating (99) and (112) using definition 15 one arrives at the final set of equations

$$\left(\frac{\hbar^2}{2m_\alpha}+\frac{\hbar^2}{2m_\beta}\right)\Delta\sqrt{g_2^{\alpha,\beta}(\boldsymbol{r}')} = \left(v_2^{\alpha,\beta}(\boldsymbol{r})+w_I^{\alpha,\beta}(\boldsymbol{r})\right)\sqrt{g_2^{\alpha,\beta}(\boldsymbol{r})} \tag{114}$$
$$\text{with}\ \ \tilde{\boldsymbol{w}}_I(\boldsymbol{k}) = -\frac{1}{2}\left(\boldsymbol{S}(\boldsymbol{k}).\boldsymbol{T}(\boldsymbol{k})+\boldsymbol{T}(\boldsymbol{k}).\boldsymbol{S}(\boldsymbol{k})-3\,\boldsymbol{T}(\boldsymbol{k})+\boldsymbol{S}^{-1}(\boldsymbol{k}).\boldsymbol{T}(\boldsymbol{k}).\boldsymbol{S}^{-1}(\boldsymbol{k})\right). \tag{115}$$

The first of them looks like a Schrödinger equation. The set could now be solved numerically, however solving them in this form causes numerical problems [8, p. 79]. Because of that we aim for an alternative formulation.

## 3.9 Formulation in k-Space

Reformulating (114):

$$\left(\frac{\hbar^2}{4m_\alpha}+\frac{\hbar^2}{4m_\beta}\right)\Delta g_2^{\alpha,\beta}(\boldsymbol{r}) - w_I^{\alpha,\beta}(\boldsymbol{r}) =$$
$$= \underbrace{v_2^{\alpha,\beta}(\boldsymbol{r})g_2^{\alpha,\beta}(\boldsymbol{r})+\left(\frac{\hbar^2}{2m_\alpha}+\frac{\hbar^2}{2m_\beta}\right)\left|\nabla\sqrt{g_2^{\alpha,\beta}(\boldsymbol{r})}\right|^2+\left(g_2^{\alpha,\beta}(\boldsymbol{r})-1\right)w_I^{\alpha,\beta}(\boldsymbol{r})}_{V_{p-h}^{\alpha,\beta}(\boldsymbol{r})}. \tag{116}$$

Transforming into Fourier space one gets

$$\mathrm{FT}\left[\left(\frac{\hbar^2}{4m_\alpha}+\frac{\hbar^2}{4m_\beta}\right)\Delta g_2^{\alpha,\beta}(\boldsymbol{r})-w_I^{\alpha,\beta}(\boldsymbol{r})\right]=\tilde{V}_{p-h}^{\alpha,\beta}(\boldsymbol{k}) \tag{117}$$

$$-\left(\frac{\hbar^2k^2}{4m_\alpha}+\frac{\hbar^2k^2}{4m_\beta}\right)\left(S^{\alpha,\beta}(\boldsymbol{k})-\delta_{\alpha,\beta}\right)-\tilde{w}_I^{\alpha,\beta}(\boldsymbol{k})=\tilde{V}_{p-h}^{\alpha,\beta}(\boldsymbol{k}) \tag{118}$$

and inserting $\tilde{\boldsymbol{w}}_I(\boldsymbol{k})$ from (115) into (118) yields

$$\boldsymbol{S}^{-1}(\boldsymbol{k}).\boldsymbol{T}(\boldsymbol{k}).\boldsymbol{S}^{-1}(\boldsymbol{k})-\boldsymbol{T}(\boldsymbol{k})=2\tilde{\boldsymbol{V}}_{p-h}(\boldsymbol{k}). \tag{119}$$

This equation should now be solved for $\boldsymbol{S}(\boldsymbol{k})$. Therefore we add $\boldsymbol{T}(\boldsymbol{k})$ to (119) and multiply with $\sqrt{\boldsymbol{T}(\boldsymbol{k})}$ from both left and right

$$\sqrt{\boldsymbol{T}(\boldsymbol{k})}.\boldsymbol{S}^{-1}(\boldsymbol{k}).\sqrt{\boldsymbol{T}(\boldsymbol{k})}.\sqrt{\boldsymbol{T}(\boldsymbol{k})}.\boldsymbol{S}^{-1}(\boldsymbol{k}).\sqrt{\boldsymbol{T}(\boldsymbol{k})}=2\sqrt{\boldsymbol{T}(\boldsymbol{k})}.\tilde{\boldsymbol{V}}_{p-h}(\boldsymbol{k}).\sqrt{\boldsymbol{T}(\boldsymbol{k})}+\boldsymbol{T}^2(\boldsymbol{k}). \tag{120}$$

We now diagonalize the rights side of (120). $\boldsymbol{D}(\boldsymbol{k})$ is the diagonal form with the co-matrices $\boldsymbol{A}(\boldsymbol{k})$ and $\boldsymbol{A}^{-1}(\boldsymbol{k})$. Note that the matrix $2\sqrt{\boldsymbol{T}(\boldsymbol{k})}.\tilde{\boldsymbol{V}}_{p-h}(\boldsymbol{k}).\sqrt{\boldsymbol{T}(\boldsymbol{k})}+\boldsymbol{T}^2(\boldsymbol{k})$ is hermitian. This is an advantage over the other ways to solve for $\boldsymbol{S}(\boldsymbol{k})$.

$$2\sqrt{\boldsymbol{T}(\boldsymbol{k})}.\tilde{\boldsymbol{V}}_{p-h}(\boldsymbol{k}).\sqrt{\boldsymbol{T}(\boldsymbol{k})}+\boldsymbol{T}^2(\boldsymbol{k})=:\boldsymbol{A}(\boldsymbol{k}).\boldsymbol{D}(\boldsymbol{k}).\boldsymbol{A}^{-1}(\boldsymbol{k}). \tag{121}$$

Now we get

$$\sqrt{\boldsymbol{T}(\boldsymbol{k})}.\boldsymbol{S}^{-1}(\boldsymbol{k}).\sqrt{\boldsymbol{T}(\boldsymbol{k})}.\sqrt{\boldsymbol{T}(\boldsymbol{k})}.\boldsymbol{S}^{-1}(\boldsymbol{k}).\sqrt{\boldsymbol{T}(\boldsymbol{k})}=\boldsymbol{A}(\boldsymbol{k}).\boldsymbol{D}(\boldsymbol{k}).\boldsymbol{A}^{-1}(\boldsymbol{k}) \tag{122}$$

$$\sqrt{\boldsymbol{T}(\boldsymbol{k})}.\boldsymbol{S}^{-1}(\boldsymbol{k}).\sqrt{\boldsymbol{T}(\boldsymbol{k})}=\boldsymbol{A}(\boldsymbol{k}).\sqrt{\boldsymbol{D}(\boldsymbol{k})}.\boldsymbol{A}^{-1}(\boldsymbol{k}) \tag{123}$$

$$\boldsymbol{S}^{-1}(\boldsymbol{k})=\sqrt{\boldsymbol{T}^{-1}(\boldsymbol{k})}.\boldsymbol{A}(\boldsymbol{k}).\sqrt{\boldsymbol{D}(\boldsymbol{k})}.\boldsymbol{A}^{-1}(\boldsymbol{k}).\sqrt{\boldsymbol{T}^{-1}(\boldsymbol{k})} \tag{124}$$

$$\boldsymbol{S}(\boldsymbol{k})=\sqrt{\boldsymbol{T}(\boldsymbol{k})}.\boldsymbol{A}(\boldsymbol{k}).\sqrt{\boldsymbol{D}^{-1}(\boldsymbol{k})}.\boldsymbol{A}^{-1}(\boldsymbol{k}).\sqrt{\boldsymbol{T}(\boldsymbol{k})}. \tag{125}$$

Gathering up equations (115), (116) and (125), our final set of equations in alternative formulation is composed of (126) – (128). These equations can be solved iteratively in that order starting with a sensible initial guess for $g_2^{\alpha\,\beta}(\boldsymbol{r})$ [8, p. 78 – 80]

$$\tilde{\boldsymbol{w}}_I(\boldsymbol{k})=-\frac{1}{2}\left(\boldsymbol{S}(\boldsymbol{k}).\boldsymbol{T}(\boldsymbol{k})+\boldsymbol{T}(\boldsymbol{k}).\boldsymbol{S}(\boldsymbol{k})-3\,\boldsymbol{T}(\boldsymbol{k})+\boldsymbol{S}^{-1}(\boldsymbol{k}).\boldsymbol{T}(\boldsymbol{k}).\boldsymbol{S}^{-1}(\boldsymbol{k})\right) \tag{126}$$

$$V_{p-h}^{\alpha,\beta}(\boldsymbol{r})=v_2^{\alpha,\beta}(\boldsymbol{r})g_2^{\alpha,\beta}(\boldsymbol{r})+\left(\frac{\hbar^2}{2m_\alpha}+\frac{\hbar^2}{2m_\beta}\right)\left|\nabla\sqrt{g_2^{\alpha,\beta}(\boldsymbol{r})}\right|^2+\left(g_2^{\alpha,\beta}(\boldsymbol{r})-1\right)w_I^{\alpha,\beta}(\boldsymbol{r}) \tag{127}$$

$$\boldsymbol{S}(\boldsymbol{k})=\sqrt{\boldsymbol{T}(\boldsymbol{k})}.\boldsymbol{A}(\boldsymbol{k}).\sqrt{\boldsymbol{D}^{-1}(\boldsymbol{k})}.\boldsymbol{A}^{-1}(\boldsymbol{k}).\sqrt{\boldsymbol{T}(\boldsymbol{k})}. \tag{128}$$

# 4 Results

## 4.1 General Remarks

### 4.1.1 Algorithm

In the process of iteratively solving equations (126) to (128) several constraints affecting the functions $g_2(\boldsymbol{r})$ and $S(\boldsymbol{k})$ can be taken advantage of. First of all $g_2$ stands for a probability, therefore the $g_2$ data must be real. The relation between $g_2$ and $S$ via a Fourier transform implies that $S(\boldsymbol{k})$ has to be a hermitian function. Remembering the fact that $g_2^{\alpha,\beta}(\boldsymbol{r}) = g_2^{\beta,\alpha}(-\boldsymbol{r})$, a relation also valid for $S$, in combination with the fact that for fixed $\alpha$ and $\beta$ the functions are hermitian, one can deduce, that for fixed $\boldsymbol{k}$ $S^{\alpha,\beta}(\boldsymbol{k}) = S^{\beta,\alpha}(\boldsymbol{k})^*$, i.e. the matrix $\boldsymbol{S}(\boldsymbol{k})$ is hermitian too. Those relations help speeding up the algorithms and saving memory at the same time. Note also that the most time-consuming part of the calculation are the matrix operations. Many of them have to be done at the same time and the calculations do not depend on the results of each other. The algorithm is efficiently parallelizable due to that.

During the calculations it has to be assured that the pair distribution function vanishes at small distances. Since the pair distribution function is calculated via inverse Fourier transforms, that behaviour must be enforced in some way. One possible way is to join the just calculated pair distribution function with the one from the last iteration [8, p.79]. Usually $\lambda = 1$

$$g_{n+1}^{\alpha,\beta} = g_n^{\alpha,\beta} \exp\left\{\lambda\left(g_{n+1}'^{\alpha,\beta} - g_n^{\alpha,\beta}\right)\right\}. \tag{129}$$

Figure 3 shows a flowchart of the implemented algorithm.

### 4.1.2 Unit System

For the calculations we choose a suitable unit system, in which all quantities are not too far from unity. $m_\alpha$ is the mass of dipoles of type $\alpha$, $\mathfrak{m}_\alpha$ is the magnetic moment of dipoles of type $\alpha$, $\mu_0$ ist the vacuum permeability. Analogous $\mathfrak{p}$ denote electric dipole momenta and $\epsilon_0$ is the vacuum permittivity. Considering the hamiltonian

$$\widehat{\mathcal{H}} = -\sum_\alpha \sum_i \frac{\hbar^2}{2m_\alpha}\Delta_{\alpha,i} + \frac{1}{2}\sum_{\alpha,\beta}\sum_{i,j}{}' v_2^{\alpha,\beta}(\boldsymbol{r}_{\alpha,i},\, \boldsymbol{r}_{\beta,j}) \tag{130}$$

$$\text{with}\quad v_2^{\alpha,\beta}(\boldsymbol{r}_{\alpha,i},\, \boldsymbol{r}_{\beta,j}) = \frac{\mu_0}{4\pi\left|\boldsymbol{r}_{\alpha,i} - \boldsymbol{r}_{\beta,j}\right|^3}\left(\mathfrak{m}_\alpha.\mathfrak{m}_\beta - 3\frac{\mathfrak{m}_\alpha.\left(\boldsymbol{r}_{\alpha,i} - \boldsymbol{r}_{\beta,j}\right)\mathfrak{m}_\beta.\left(\boldsymbol{r}_{\alpha,i} - \boldsymbol{r}_{\beta,j}\right)}{\left|\boldsymbol{r}_{\alpha,i} - \boldsymbol{r}_{\beta,j}\right|^2}\right) \tag{131}$$

it would be a sensible idea to measure distances in dipole lengths

$$r_0 = m_0\frac{\mu_0\left|\mathfrak{m}_0\right|^2}{4\pi\hbar^2} \text{ for magnetic and } r_0 = m_0\frac{\left|\mathfrak{p}_0\right|^2}{4\pi\epsilon_0\hbar^2} \text{ for electric dipoles} \tag{132}$$

and energies in

$$E_0 = \frac{\hbar^2}{m_0 r_0^2}, \tag{133}$$

because then the hamiltonian would look like

$$\widehat{\mathcal{H}} = -\sum_\alpha \sum_i \frac{1}{2m_\alpha^*}\Delta_{\alpha,i} + \frac{1}{2}\sum_{\alpha,\beta}\sum_{i,j}{}'\left(\frac{1}{\left|\boldsymbol{r}_{\alpha,i} - \boldsymbol{r}_{\beta,j}\right|}\right)^3 \times\left(\boldsymbol{n}_\alpha.\boldsymbol{n}_\beta - 3\frac{\left(\boldsymbol{n}_\alpha.\left(\boldsymbol{r}_{\alpha,i} - \boldsymbol{r}_{\beta,j}\right)\right)\left(\boldsymbol{n}_\beta.\left(\boldsymbol{r}_{\alpha,i} - \boldsymbol{r}_{\beta,j}\right)\right)}{\left|\boldsymbol{r}_{\alpha,i} - \boldsymbol{r}_{\beta,j}\right|^2}\right). \tag{134}$$

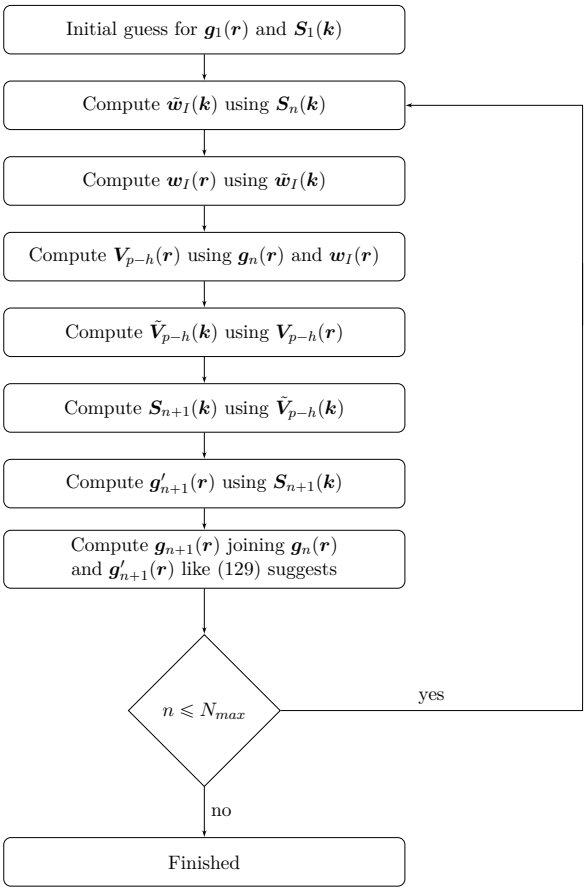


Figure 3: Flowchart of the computation of pair distribution function and static structure function with $N_{max}$ iterations.

In (132), (133) and (134) we introduce relative masses and dipole momenta

$$\boldsymbol{n}_\gamma := \frac{\mathfrak{m}_\gamma}{|\mathfrak{m}_0|},\ \boldsymbol{n}_\gamma := \frac{\mathfrak{p}_\gamma}{|\mathfrak{p}_0|} \text{ for the magnetic and electric case respectively} \tag{135}$$

$$\text{and } m^*_\gamma := \frac{m_\gamma}{m_0}. \tag{136}$$

Hence this will be the unit system of choice used to present the results in in the following [2, p. 1]. Typical dipole lenghts would be $r_0 = 1.1 \times 10^{-9}$m for chromium atoms, $r_0 = 1.1 \times 10^{-8}$m for erbium atoms, $r_0 = 2.1 \times 10^{-8}$m for dysprosium atoms and $r_0 = 7.5 \times 10^{-7}$m for hydroxyl radicals. RbCs is a strong electric dipole with $r_0 = 2.1 \times 10^{-6}$m [3, p. 5040], hence research efforts are currently put into the creation of a BEC [15].

Figure 4 is a plot of the intra-layer and inter-layer potential energy of two dipoles along the x-axis. The dipoles are tilted by multiple angles in direction of x-axis. The angle $\theta$ is specified in radiants and measured between the z-axis (normal to the layer) and the dipole moment. In the plot of the intra-layer potential energy we can observe that the potential energy decreases with increasing tilting angles $\theta$. Considering (131), at an angle of

$$\theta_{\max} = \arcsin\sqrt{\frac{1}{3}} \approx 0.196\pi \tag{137}$$

the repulsive intra-layer interaction turns into a attractive one, consequences are discussed in the following subsection. The inter-layer interaction is basically an attractive one, but tilting of the dipoles effectively reduces the attractive interaction and turns on a repulsive one at the same time. Note also

that with $\theta = 0$ the interaction is isotropic, in the other cases not. This fact will also be reflected in the corresponding pair distribution functions in the following sections. See also Figure 2 for the general dipole potential.

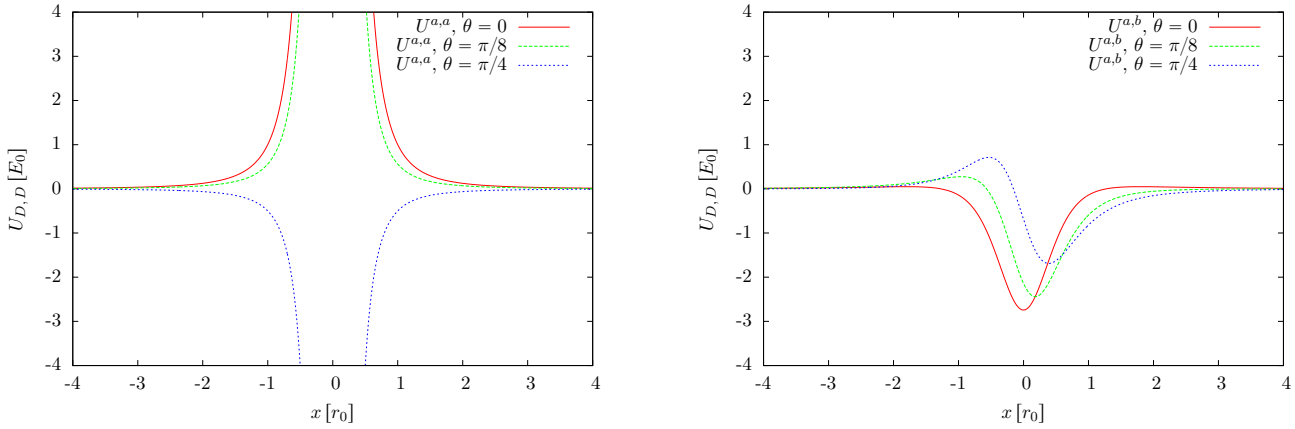


Figure 4: Potential energy of two interacting dipoles along the x-axis. The dipoles are situated in the same layer (left) and situated in different layers (right). The distance between the layers is $d = 0.9\,r_0$. Dipoles are tilted by $\theta = 0$, $\theta = \pi/8$ and $\theta = \pi/4$.

## 4.2 One Dipole Layer

We start with computing the static structure function $S^{a,a}(\boldsymbol{k})$ and the pair distribution function $g_2^{a,a}(\boldsymbol{r})$ for one dipole layer with dipole orientation perpendicular to that layer. Figure 5 shows the solutions for a relatively high density of $\rho_1^a = 256\,r_0^{-2}$. The systems with high densities are the most interesting ones, those HNC-EL theory was developed for, because in these cases the pair correlations are significant. The results are not quantitative correct, though, because of the neglect of elementary diagrams and triplet correlations. The first set of solutions show clearly isotropic behavior and this is exactly what one would expect, because the generally anisotropic dipole potential is isotropic in the case of dipole orientation perpendicular to the layer (non-tilted).

Taking advantage of isotropy, Figure 6 is a plot of structure and pair distribution functions along the x-axis. Several densities, namely $\rho_1^a = 9\,r_0^{-2}$, $\rho_1^a = 25\,r_0^{-2}$, $\rho_1^a = 49\,r_0^{-2}$, $\rho_1^a = 128\,r_0^{-2}$ and $\rho_1^a = 256\,r_0^{-2}$ are shown. The positions of the peaks in the static structure function are determined by the densities, for example we would expect the peak for $\rho_1 = 256\,r_0^{-2}$ at $k_{max} = 2\pi\sqrt{\rho_1} \approx 100\,r_0^{-1}$. What one can learn from the computation, however, is that the higher the density the higher the peak. High peaks, being the Fourier transforms of the pair distribution function, imply tendency towards long range order in the dipole layer. This order can be seen in the pair distribution function in Figures 5 and 6, however, particles sufficiently far away from each other are not correlated any more (the pair distribution function approaches 1).

Figures 7 to 10 show pair distribution functions and static structure functions of tilted dipoles with a fixed density of $\rho = 256\,r_0^{-2}$. Tilting of the dipoles works only up to a certain critical angle $\theta_{\text{crit}}$, beyond that angle the HNC-EL equations do not converge any more. The angle $\theta$ can certainly not exceed the maximal angle $\theta_{\text{max}}$ from (137), because beyond that angle the system collapses along the x-axis due to the attractive part of the dipole-dipole interaction exceeding the repulsive one (see also Figures 2 and 4). In the computations with $\rho_1^a = 256\,r_0^{-2}$, tilting of the dipoles was possible up to $\theta_{crit} = 0.185\pi$, above this angle the computations are unstable due to the high density. So, tilting was possible almost up to the maximal angle in this case. However, with lower densities even further tilting is possible, right up to $\theta_{\text{max}}$ . With increasing $\theta$ anisotropy of the solution grows larger. Having said that, note that the

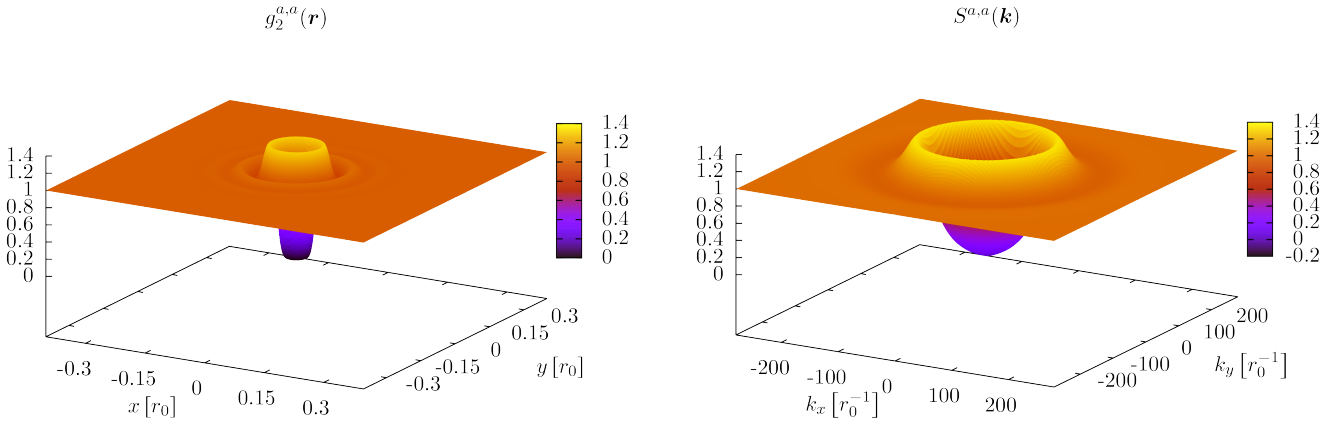


Figure 5: Pair distribution function $g_2^{a,\,a}(\boldsymbol{r})$ (left panel) and static structure function $S^{a,\,a}(\boldsymbol{k})$ (right panel) for one dipole layer, for the density $\rho_1^a = 256\,r_0^{-2}$, non-tilted dipoles. The pair distribution function only deviates from unity at small $r$. At larger $r > 0.3\,r_0$ the dipoles are not correlated any more. Thus the system is gaseous.

dipole-dipole interaction is an even function despite being anisotropic, and so is the pair distribution function, implying that the imaginary part is still $\mathfrak{Im}\,S^{a,\,a}(\boldsymbol{k}) = 0$. In Figures 11 and 12 one can see static structure functions and pair distribution functions of Figures 7 to 10 plotted along the x- and the y-axis. In Figures 11 and 12, the red line can be chosen as reference line, since it is the one for non-tilted dipoles and therefore the same in x- and y-direction. In contrast to this reference line, the peaks of the pair distribution functions for higher tilting angles are shifted towards lower $\boldsymbol{r}$ in x-direction and shifted towards higher $\boldsymbol{r}$ in y-direction. The change in y-direction is interesting, since the interaction in y-direction is unaffected by tilting. However, the so-called sequential relation can be deduced from the definition of the pair distribution function

$$\int \mathrm{d}^2 r\ \left(g_2^{\alpha,\,\beta}(\boldsymbol{r}) - 1\right) = -\delta_{\alpha,\,\beta}\frac{1}{\sqrt{\rho_1^\alpha \rho_1^\beta}}. \tag{138}$$

Since the integral in (138) gets larger when the peaks of the pair distribution function are shifted towards lower $\boldsymbol{r}$ in x-direction, the peaks of the pair distribution function have to be shifted towards higher $\boldsymbol{r}$ in y-direction to compensate, because the right side of (138) is fixed. It is remarkable that in Figures 9 and 10 the tilting angle is large enough ($\theta = 0.175\pi$ and $\theta = 0.185\pi$, respectively) to observe strong tendency towards long range order only in y-direction, but not in x-direction. It seems like these systems are on the verge of getting solid in y-direction, but staying gaseous in x-direction, indeed found in Ref. [11].

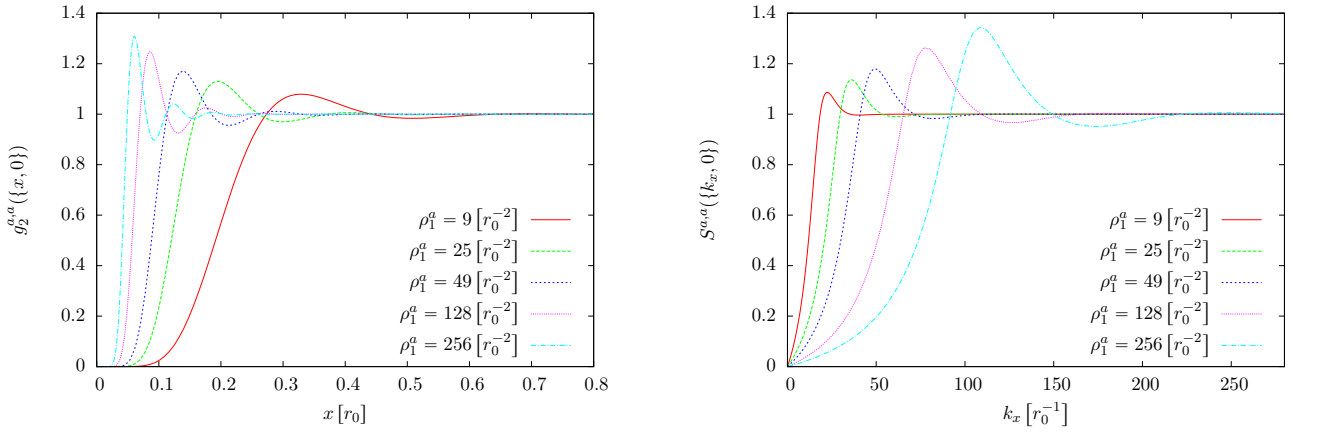


Figure 6: Pair distribution function $g_2^{a,a}(\boldsymbol{r})$ (left panel) and static structure function $S^{a,a}(\boldsymbol{k})$ (right panel) for one dipole layer, for multiple densities $\rho_1 = 9\,r_0^{-2}$, $\rho_1 = 25\,r_0^{-2}$, $\rho_1 = 49\,r_0^{-2}$, $\rho_1 = 128\,r_0^{-2}$, and $\rho_1 = 256\,r_0^{-2}$. The dipoles are oriented perpendicular to the layer. The system is isotropic, so plots for every other direction of $\boldsymbol{r}$ would be identical. For higher densities, the first peak of the pair distribution function is situated at lower $x$. For higher densities, there are also more oscillations in the pair distribution function. Thus, tendency towards long range order is higher for higher densities.

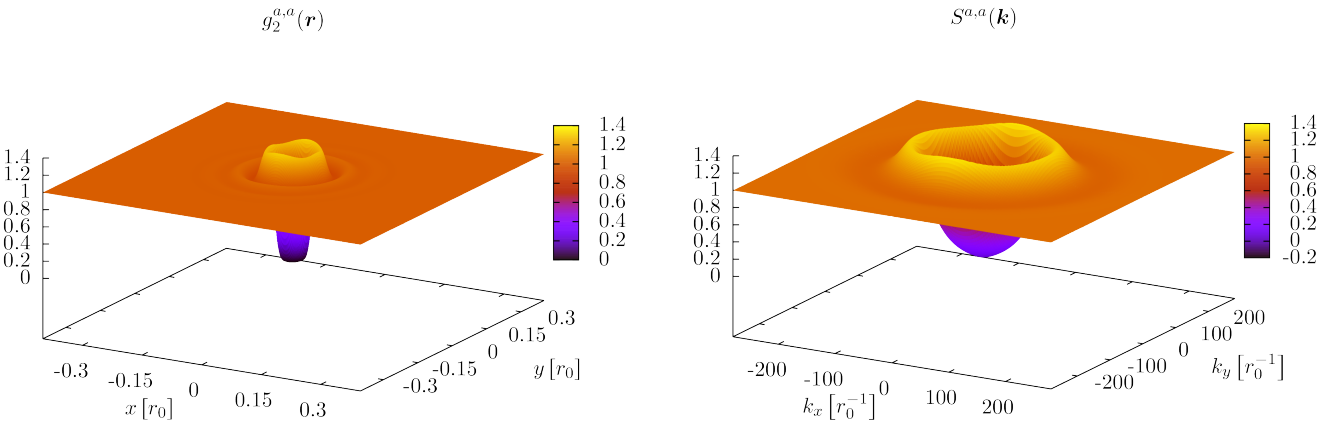


Figure 7: Like Figure 5. Dipoles are now tilted in the direction of the x-axis by an angle of $\theta = 0.1\pi$. Anisotropy slightly sets in.

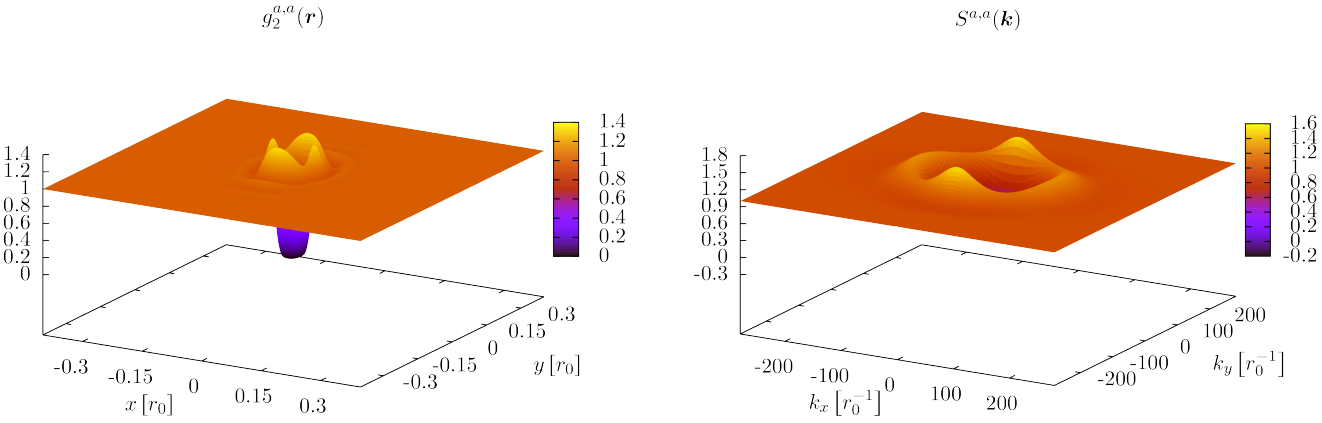


Figure 8: Like Figure 7. Dipoles are now tilted by $\theta = 0.15\pi$. One can now clearly see that the functions are no isotropic ones any more.

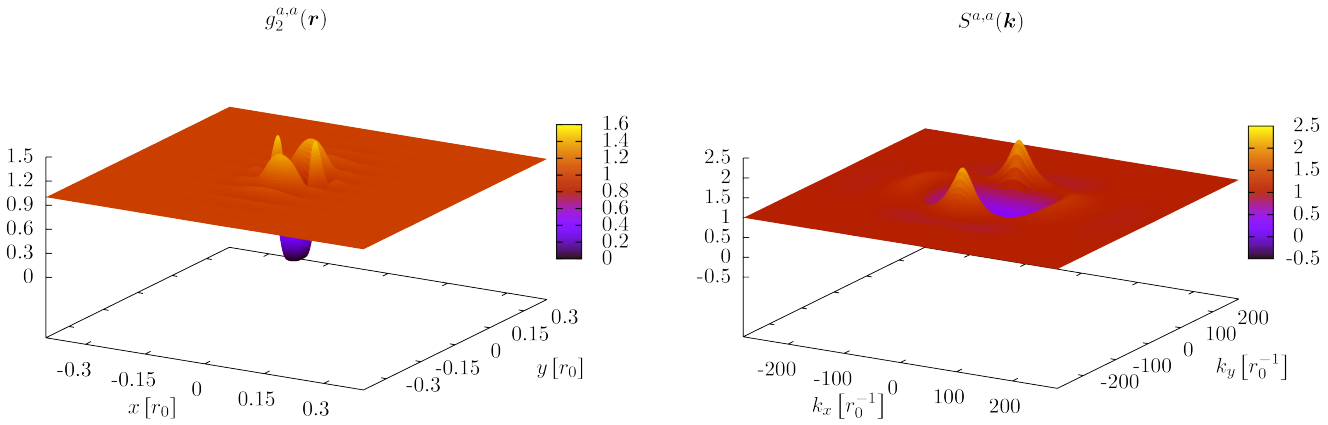


Figure 9: Like Figure 7. Dipoles are now tilted by $\theta = 0.175\pi$.

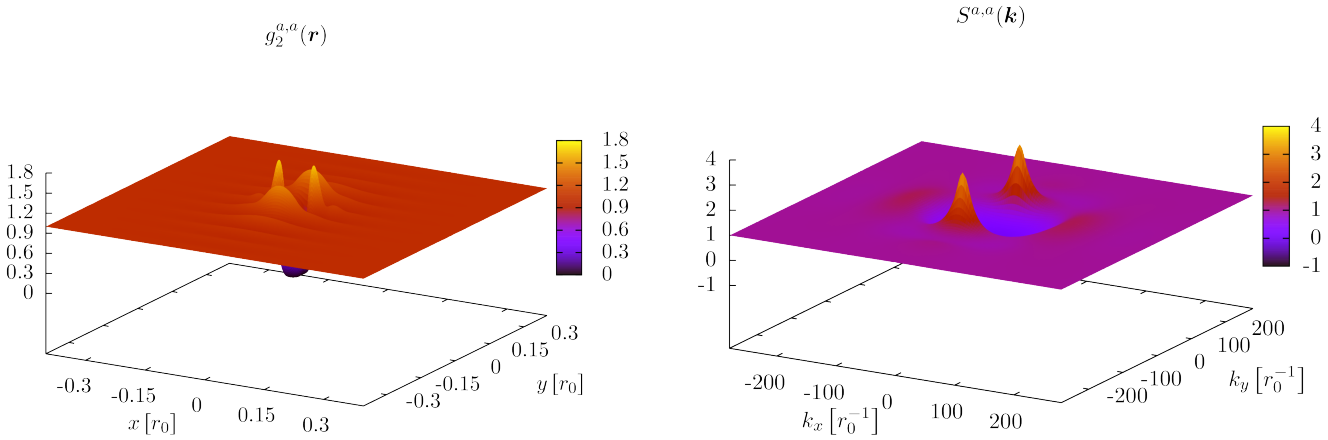


Figure 10: Like Figure 7. Dipoles are now tilted by $\theta = 0.185\pi$. For $\rho_1^a = 256\,r_0^{-2}$, this is the critical angle. No stable solutions can be obtained any more above $\theta_{\text{crit}} = 0.185\pi$. One can see high peaks in the static structure function, but only in y-direction. This is causing a high tendency towards long range order (see the oscillations) in the pair distribution function, but again only in y-direction.

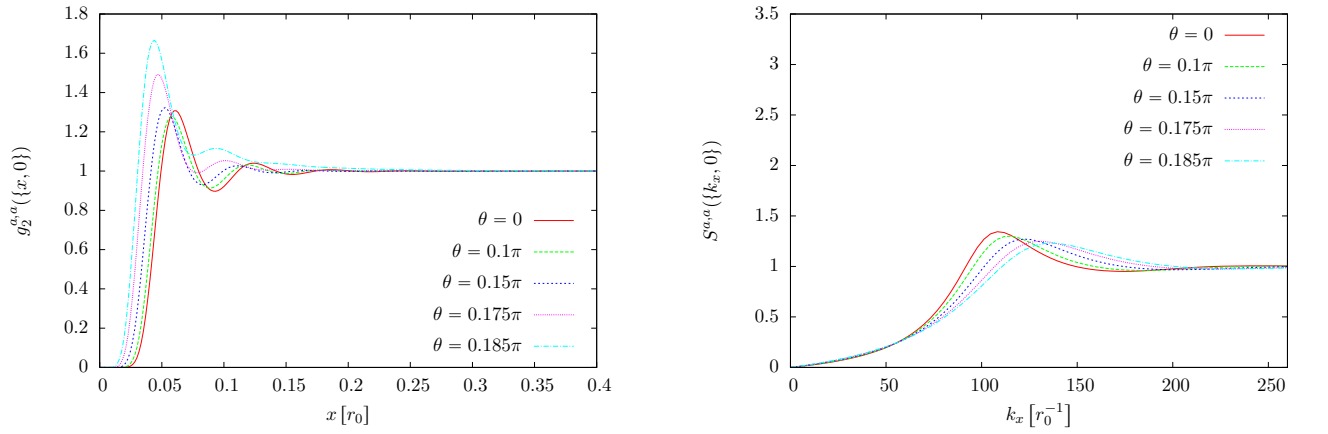


Figure 11: Pair distribution function $g_2^{a,a}(\boldsymbol{r})$ (left panel) and static structure function $S^{a,a}(\boldsymbol{k})$ (right panel) along the x-axis: One dipole layer, for the density $\rho_1^a = 256\,r_0^{-2}$ and multiple dipole orientations $\theta = 0$, $\theta = 0.1\pi$, $\theta = 0.15\pi$, $\theta = 0.175\pi$, and $\theta = 0.185\pi$. See also Figures 5 and 7 to 10. Note that the peak in the pair distribution function is situated at lower $\boldsymbol{r}$ for higher tilting angles.

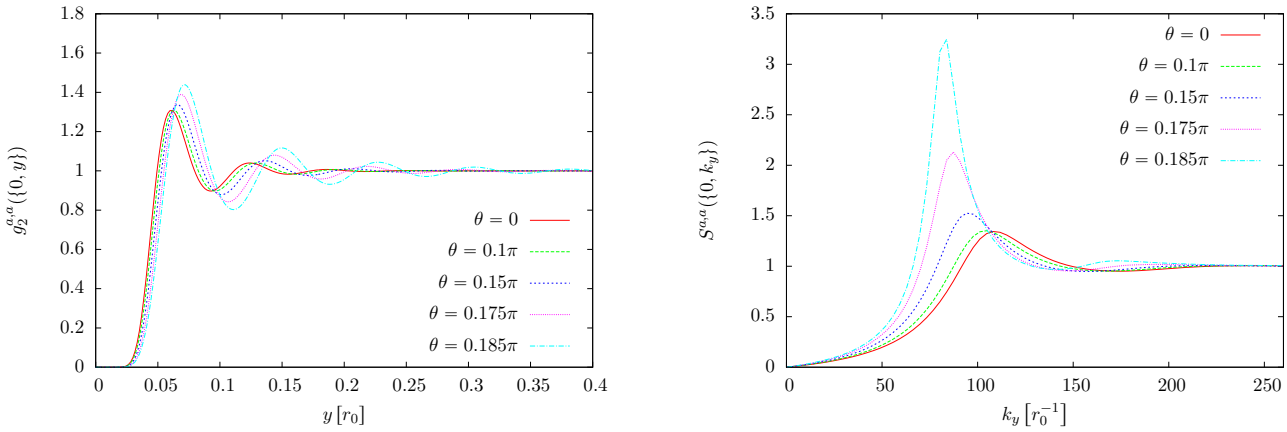


Figure 12: Like Figure 11, but along the y-axis. Note that this time the peak in the pair distribution function is situated at higher $\boldsymbol{r}$ for higher tilting angles.

## 4.3 Two Dipole Layers

In the case of $\rho_1^a = \rho_1^b$, some panels in the Figures in this section are redundant, because $g_2^{a,a}(\boldsymbol{r}) = g_2^{b,b}(\boldsymbol{r})$, $g_2^{a,b}(\boldsymbol{r}) = g_2^{b,a}(-\boldsymbol{r})$, $S^{a,a}(\boldsymbol{k}) = S^{b,b}(\boldsymbol{k})$, and $S^{a,b}(\boldsymbol{k}) = S^{b,a}(\boldsymbol{k})^*$. Yet all of the pair distribution functions and static structure functions are plotted in a matrix arrangement to emphasize those relations.

### 4.3.1 Varying inter-Layer Distances, fixed $\rho_1$, $\theta$

We now add a second dipole layer above the first one. In Figures 13 to 16 we begin with non-tilted dipoles in both layers, fixed densities of $\rho_1^\alpha = \rho_1^\beta = 256\, r_0^{-2}$, and varying distances $d$ between the two layers. The 3D-plots, Figures 13 and 14, are done only for $d = 0.06\, r_0$. One could omit 3D-plots at all—without tilting the functions are isotropic, again. The more the inter-layer pair distribution and static structure functions $g_2^{a,b}$, $g_2^{b,a}$, $S^{a,b}$ and $S^{b,a}$ deviate from 1 and 0 respectively, the closer the layers get. Coupling between the layers increases as the distance decreases. Increasing the distance between the layers causes the system to decompose into two independent one-layer systems eventually, because the intra-layer interactions outweigh the inter-layer interactions greatly. Decreasing the distance between the layers, inter-layer correlations increase very rapidly due to the $1/d^3$-dependence. Bringing the layers too close to each other, however, no stable solutions can be obtained anymore, in the computations we were able to decrease the distance down to $d = 0.06 r_0$. This is likely to be caused by dimer formation of dipoles, which our wave function ansatz containing only pair correlations does not allow for. The critical distance can be lowered by increasing densities $\rho_1$, though, since increasing the densities compensates the increase of inter-layer correlations caused by bringing the layers closer to each other. See section 4.3.3 for more details. Note that the intra-layer correlations are only slightly affected by the change of inter-layer distance.

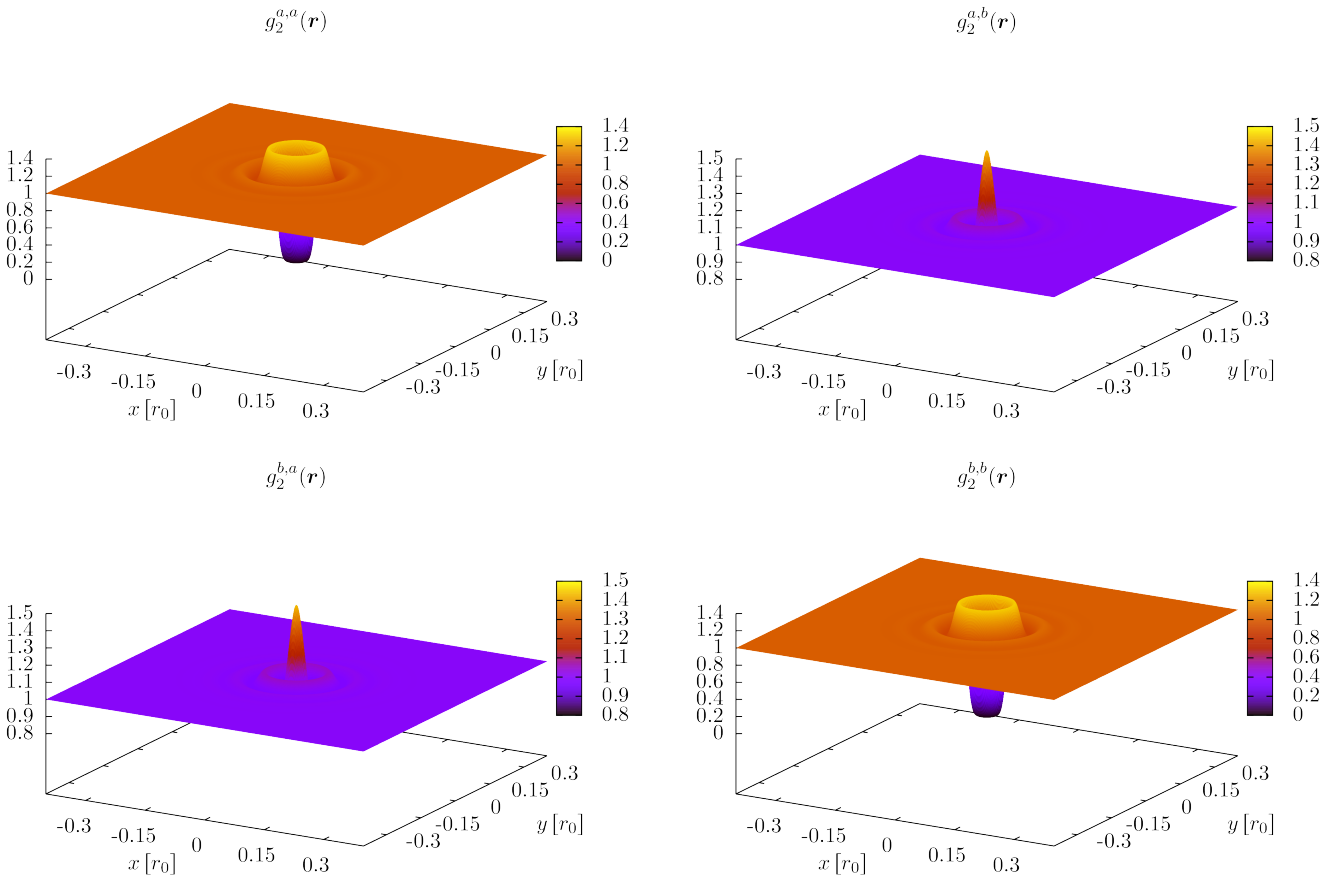


Figure 13: Pair distribution functions $g_2^{a,a}(\boldsymbol{r})$, $g_2^{a,b}(\boldsymbol{r})$, $g_2^{b,a}(\boldsymbol{r})$, and $g_2^{b,b}(\boldsymbol{r})$ for two dipole layers, for densities $\rho_1^a = \rho_1^b = 256\, r_0^{-2}$ and for a distance of $d = 0.06\, r_0$ between the layers, no tilting. Note that the functions are isotropic. Besides the intra-layer correlation, now a inter-layer correlation sets in, too. See also Figure 14 for the associated static structure functions.

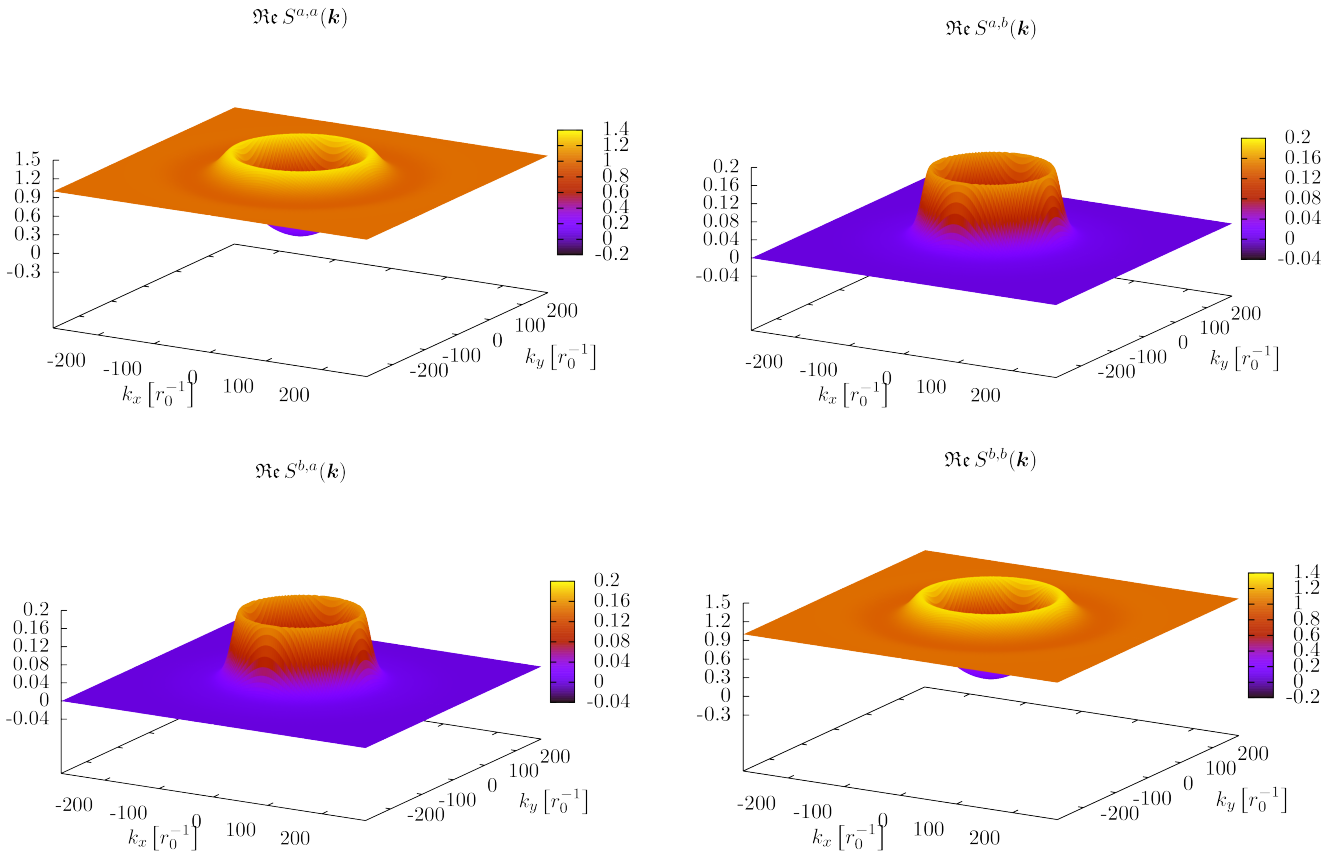


Figure 14: Static structure functions $S^{a,a}(\boldsymbol{k})$, $S^{a,b}(\boldsymbol{k})$, $S^{b,a}(\boldsymbol{k})$, and $S^{b,b}(\boldsymbol{k})$ for two dipole layers, for densities $\rho_1^a = \rho_1^b = 256\, r_0^{-2}$ and for a distance of $d = 0.06\, r_0$ between the layers, no tilting. Note that the functions are isotropic. See also Figure 13 for the associated pair distribution functions.

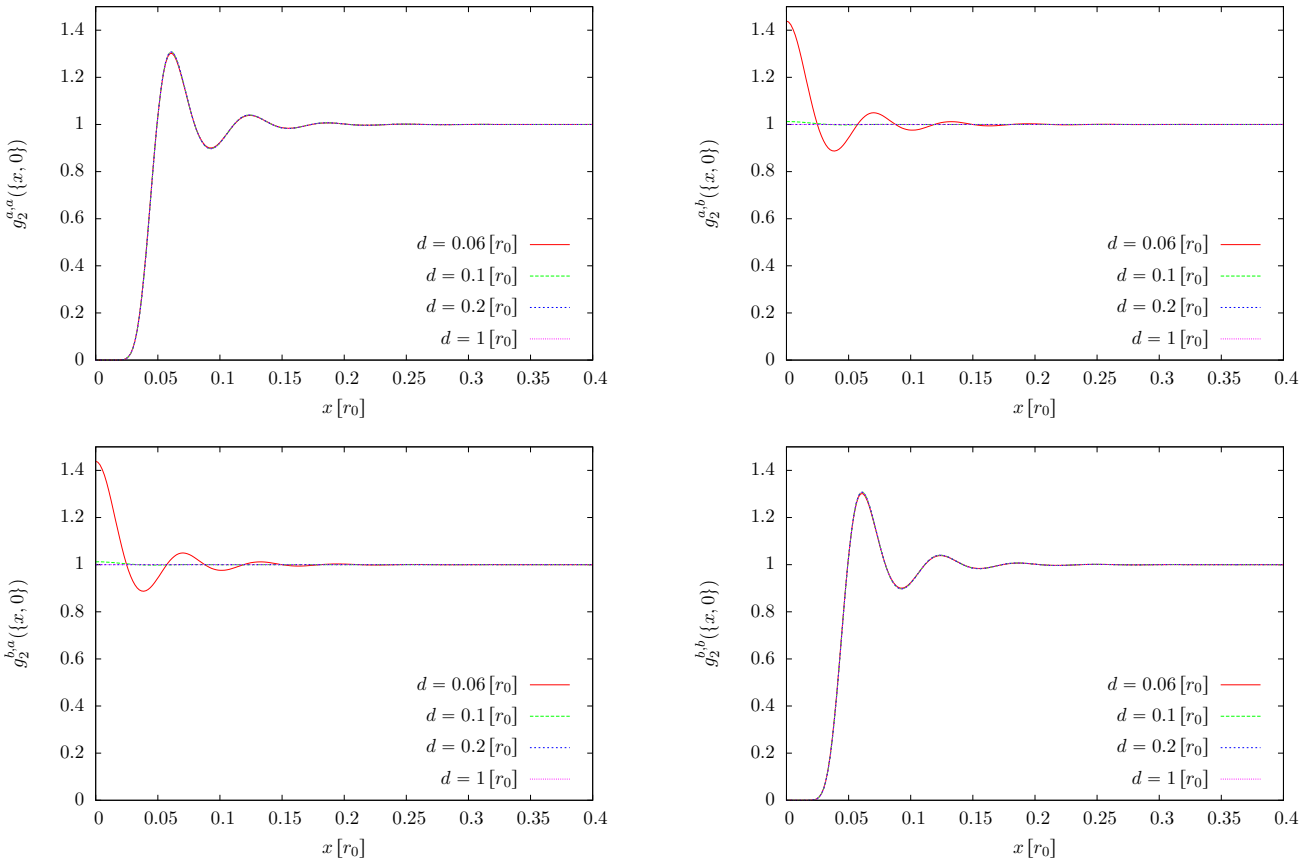


Figure 15: Pair distribution functions $g_2^{a,a}(\boldsymbol{r})$, $g_2^{a,b}(\boldsymbol{r})$, $g_2^{b,a}(\boldsymbol{r})$, and $g_2^{b,b}(\boldsymbol{r})$ along the x-axis. Results for two dipole layers, for densities $\rho_1^a = \rho_1^b = 256\, r_0^{-2}$, and for multiple distances $d = 1\, r_0$, $d = 0.2\, r_0$, $d = 0.1\, r_0$, and $d = 0.06\, r_0$ between the layers, no tilting. Note that due to the $1/d^3$-dependence, the correlations increase rapidly when the layers are brought closer to each other. See also Figure 13 for a 3D plot of the pair distribution functions for $d = 0.06\, r_0$.

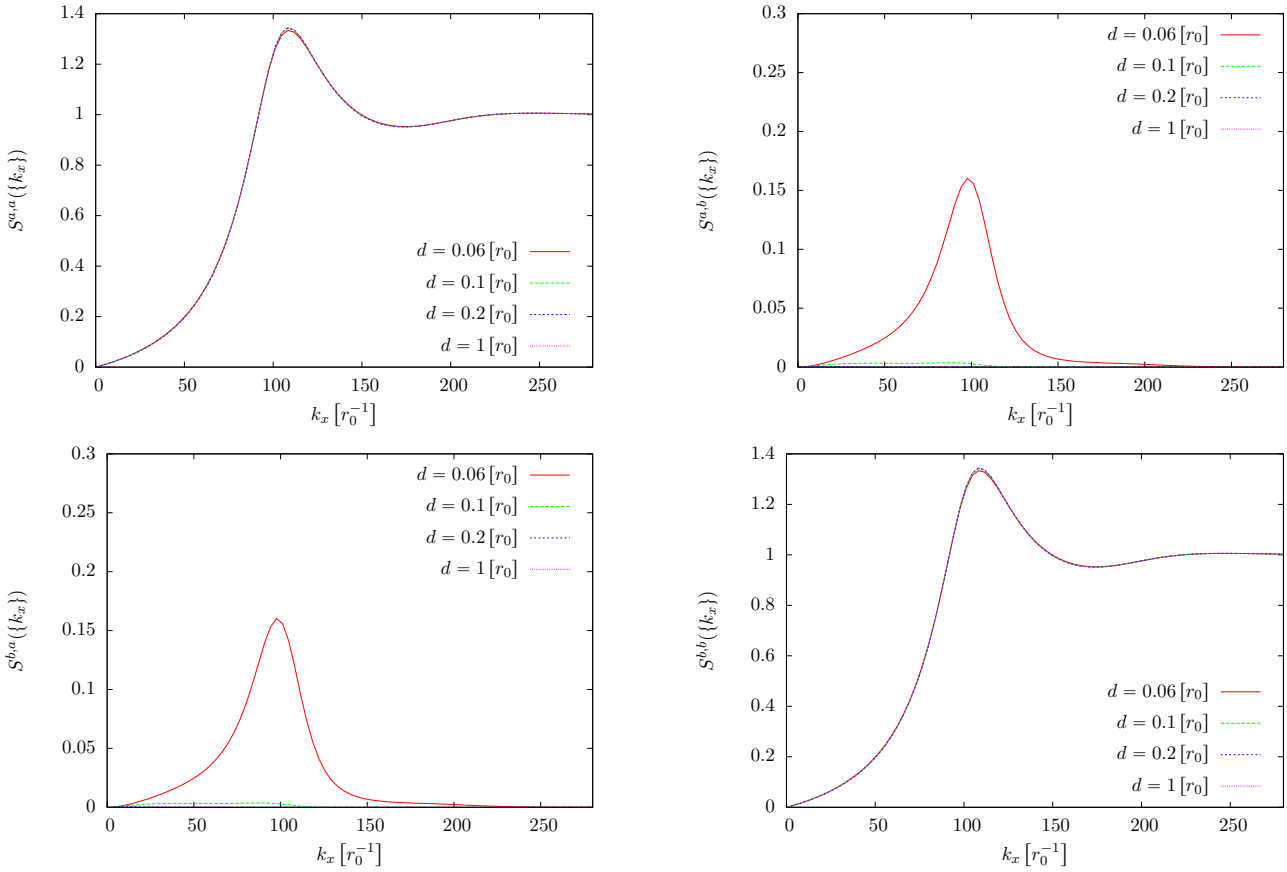


Figure 16: Static structure functions $S^{a,a}(\boldsymbol{k})$, $S^{a,b}(\boldsymbol{k})$, $S^{b,a}(\boldsymbol{k})$, and $S^{b,b}(\boldsymbol{k})$ along the x-axis for the configuration in Figure 15

### 4.3.2 Varying tilting Angles, fixed $\rho_1$, $d$

In Figures 17 to 26 the distance between the layers is fixed at $d = 0.06\,r_0$, a distance where inter-layer correlations are fairly large, see previous section 4.3.1. Now the tilting angle of the dipoles is varied. All dipoles are tilted the same way in both layers. As for a single layer (section 4.2), one can observe the loss of isotropy at non-zero angles, culminating in strong tendency towards long-range order at very high tilting angles like $\theta = 0.175\pi$ in Figure 21. In contrast to the tilted dipoles in one-layer systems from section 4.2, no results are obtained any more for $\theta = 0.185\pi$. The system seems to be unstable for $\theta > 0.175\pi$. Furthermore, this is the first time that some of the pair distribution functions, the inter-layer ones, are no even functions any more, causing imaginary contributions in the inter-layer structure functions. Figures 23 to 26 once again show the strong dependence on the direction of $\boldsymbol{r}$ and $\boldsymbol{k}$ of the pair distribution functions and the static structure functions. At higher tilting angles the system even tends to getting solid in y-direction again. The peaks in the intra-layer pair distribution functions are again shifted towards smaller $\boldsymbol{r}$ in x-direction and shifted towards larger $\boldsymbol{r}$ along the y-axis, preserving $\rho_1$. Tendency towards long range order can also be found in the inter-layer correlations, again only along the y-axis. One can also see that the static structure functions are hermitian, in the sense of $S^{\alpha,\beta}(\boldsymbol{k}) = S^{\alpha,\beta}(-\boldsymbol{k})^*$, because the pair distribution functions are real.

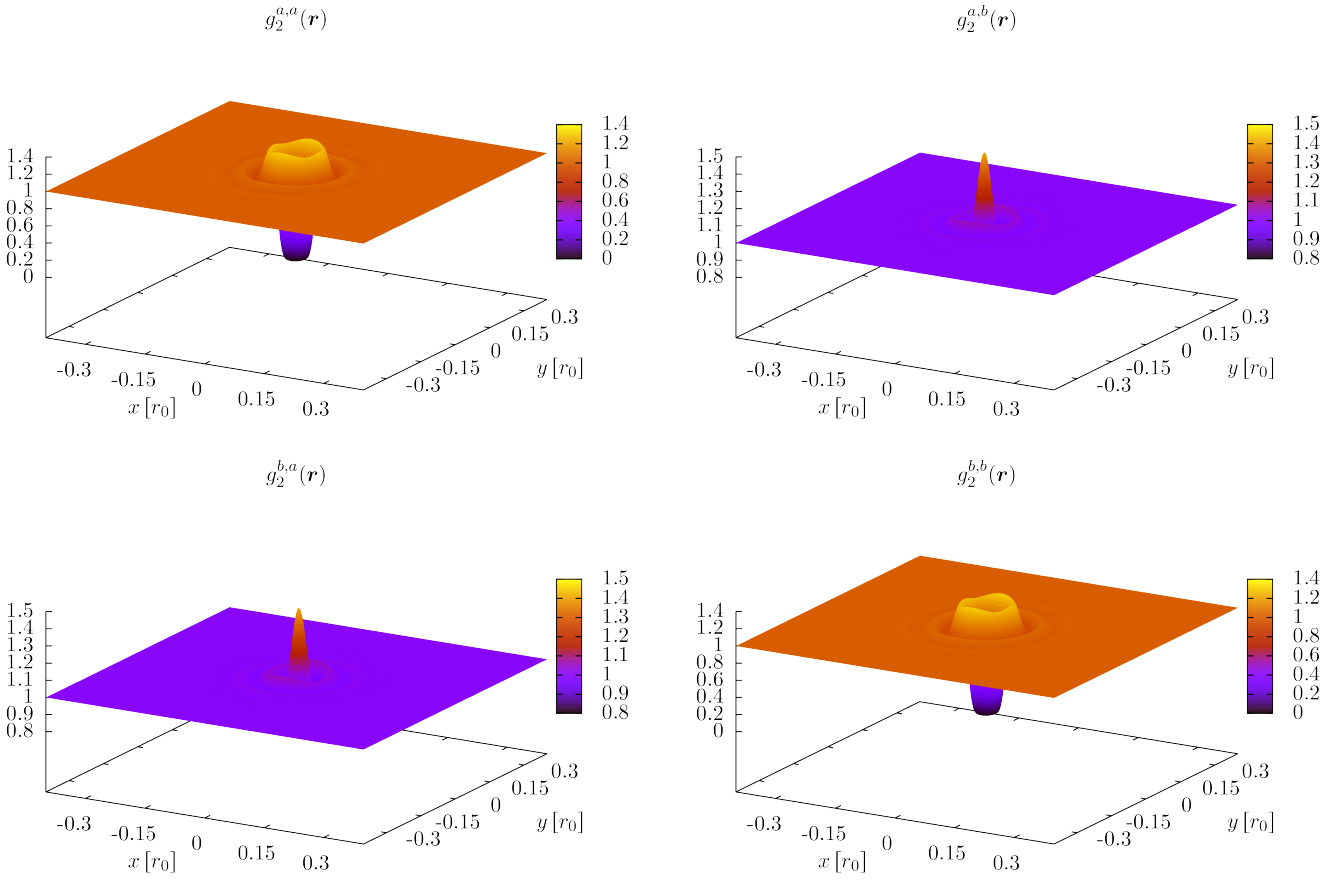


Figure 17: Like Figure 13. All dipoles are now tilted in the direction of the x-axis by an angle of $\theta = 0.1\pi$. Anisotropy slightly sets in. Furthermore, note that the pair distribution functions are no even functions any more.

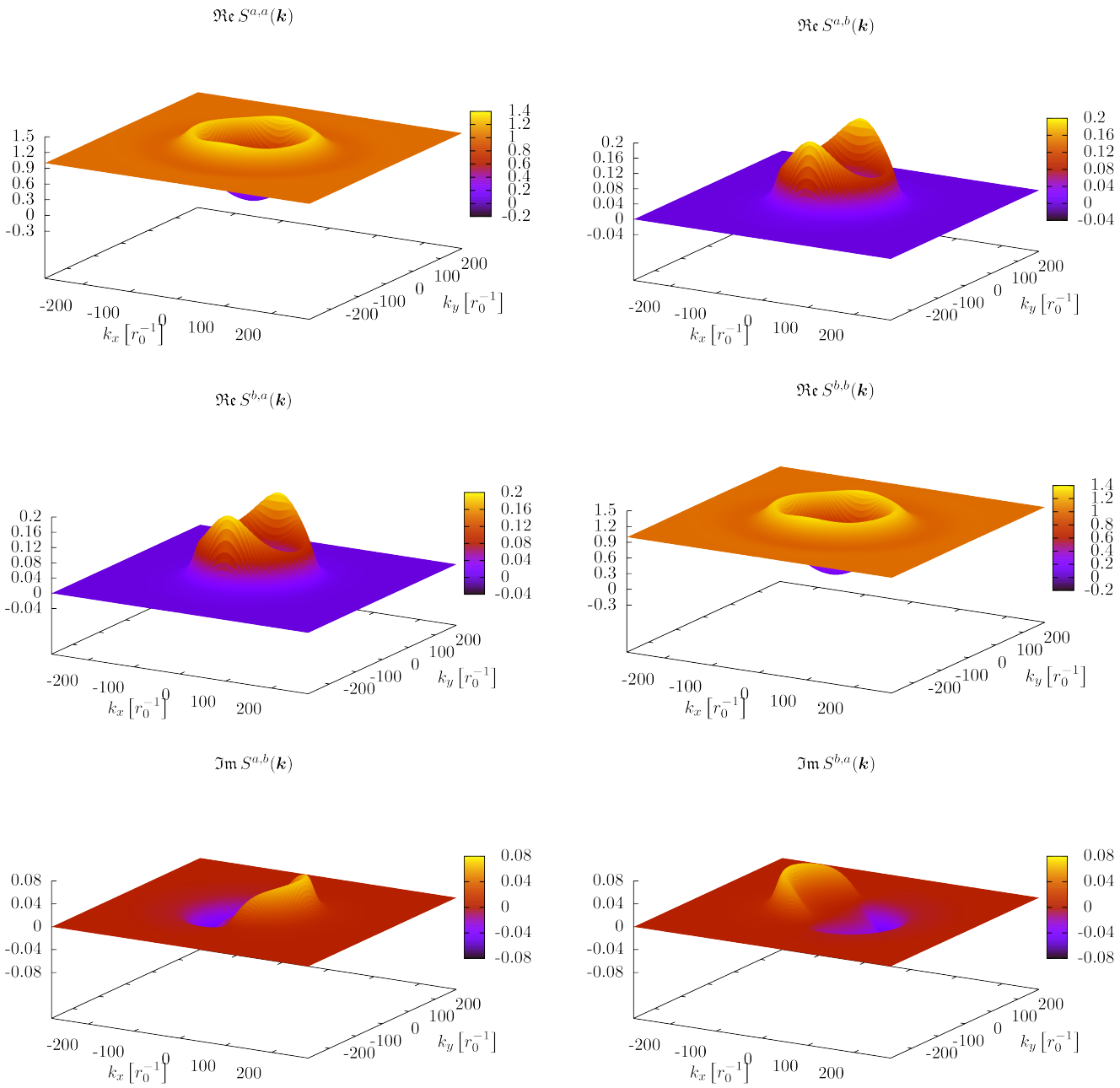


Figure 18: Like Figure 14. All dipoles are now tilted in the direction of the x-axis by an angle of $\theta = 0.1\pi$. Anisotropy slightly sets in. Furthermore, note that the pair distribution functions are no even functions any more. Thus the imaginary parts of the inter-layer static structure functions do not vanish any more.

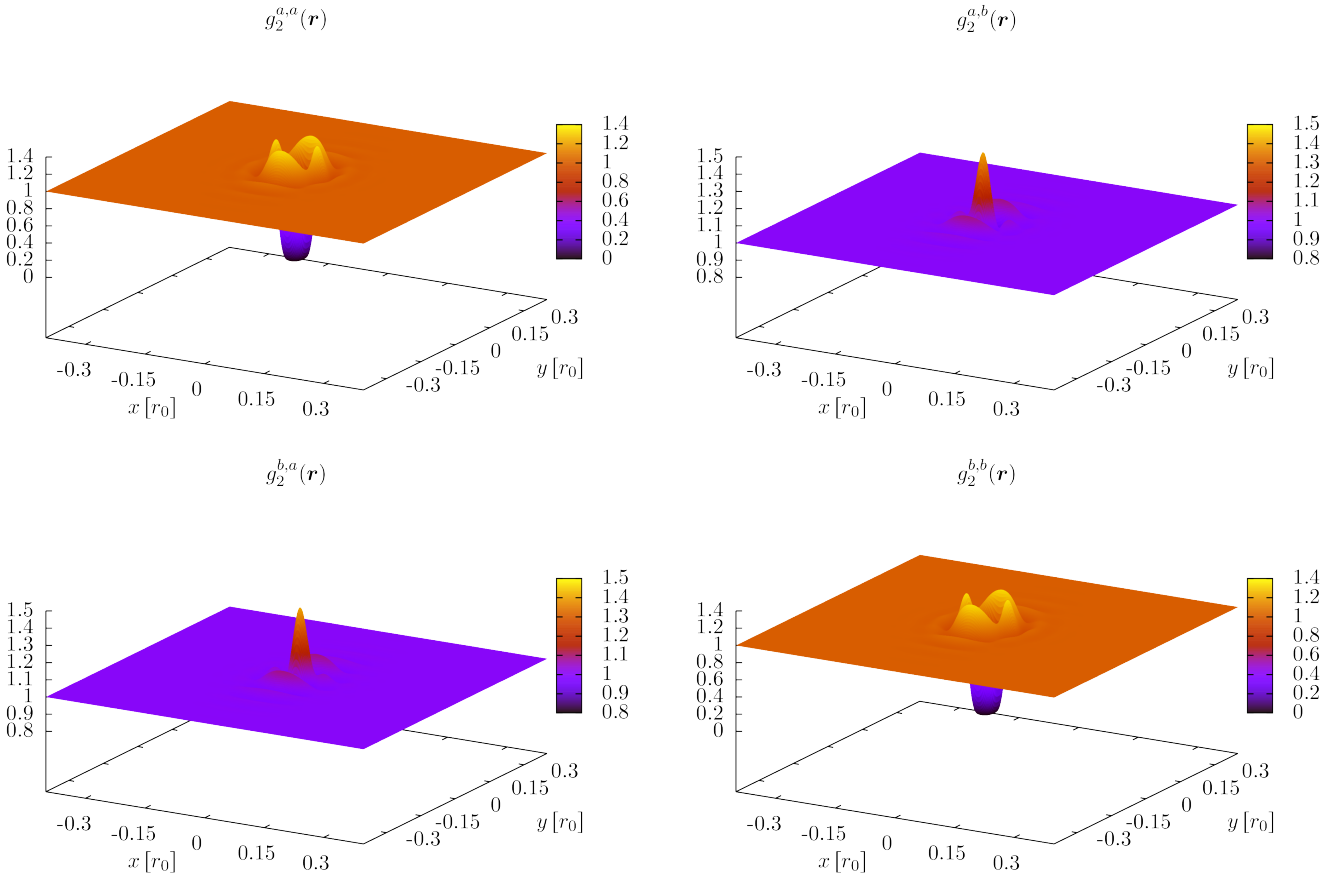


Figure 19: Like Figure 17. Dipoles are now tilted by $\theta = 0.15\pi$. One can now clearly see that the functions are no isotropic ones any more.

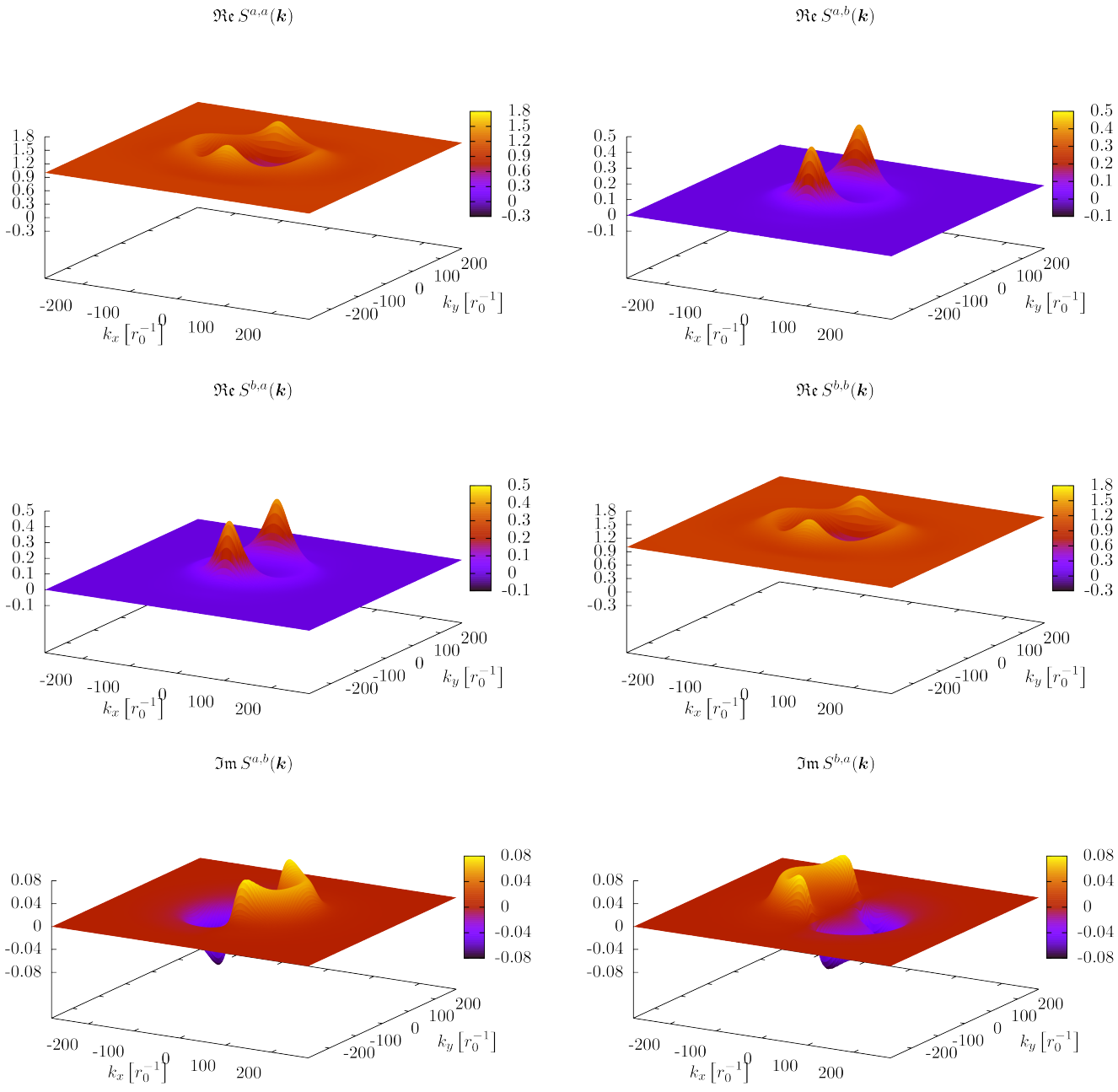


Figure 20: Like Figure 18. Dipoles are now tilted by $\theta = 0.15\pi$.

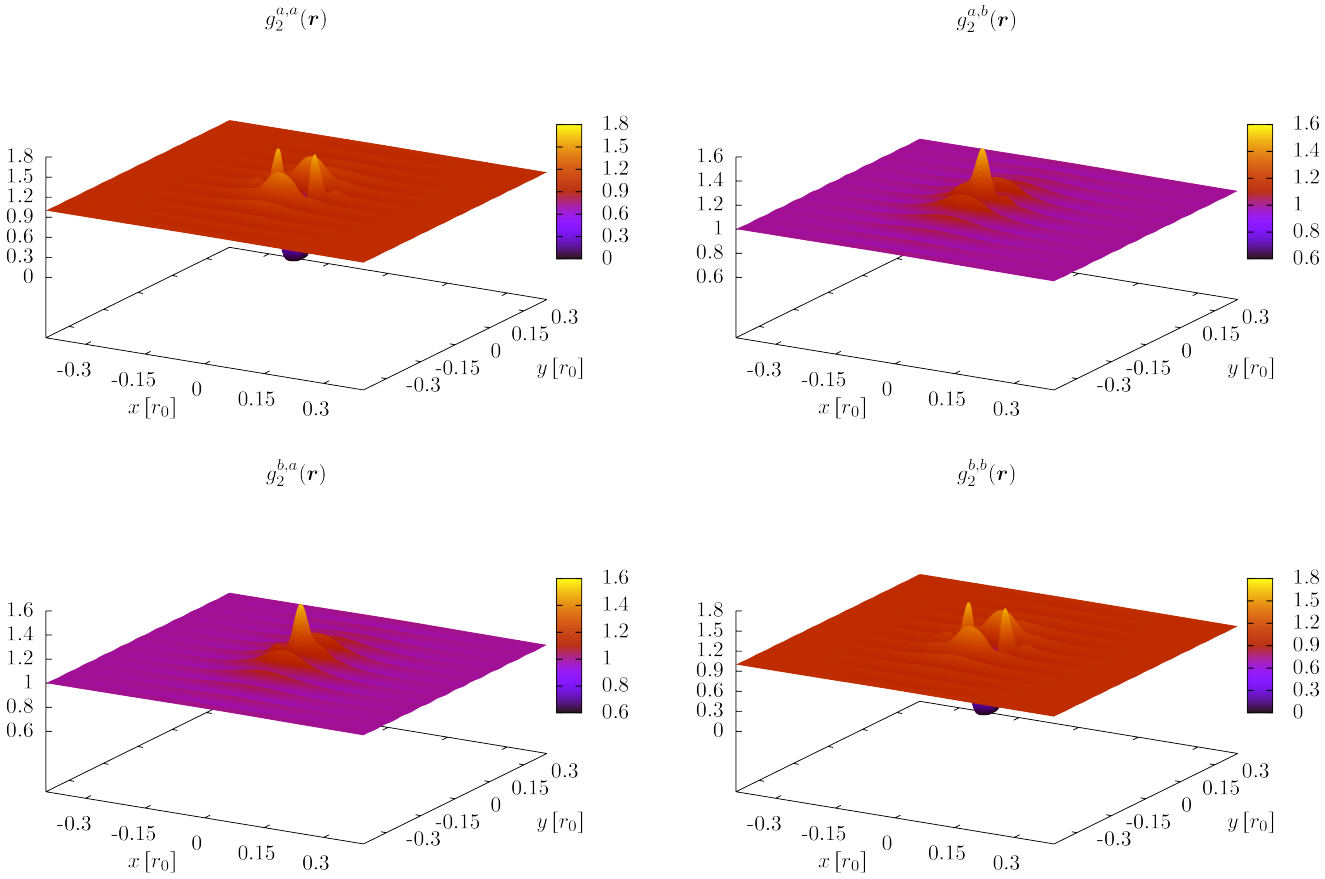


Figure 21: Like Figure 17. Dipoles are now tilted by $\theta = 0.175\pi$. this is the critical angle. No stable solutions can be obtained any more above $\theta_{\text{crit}} = 0.175\pi$. One can see a high tendency towards long range order (see the oscillations) in the pair distribution functions, but only in y-direction.

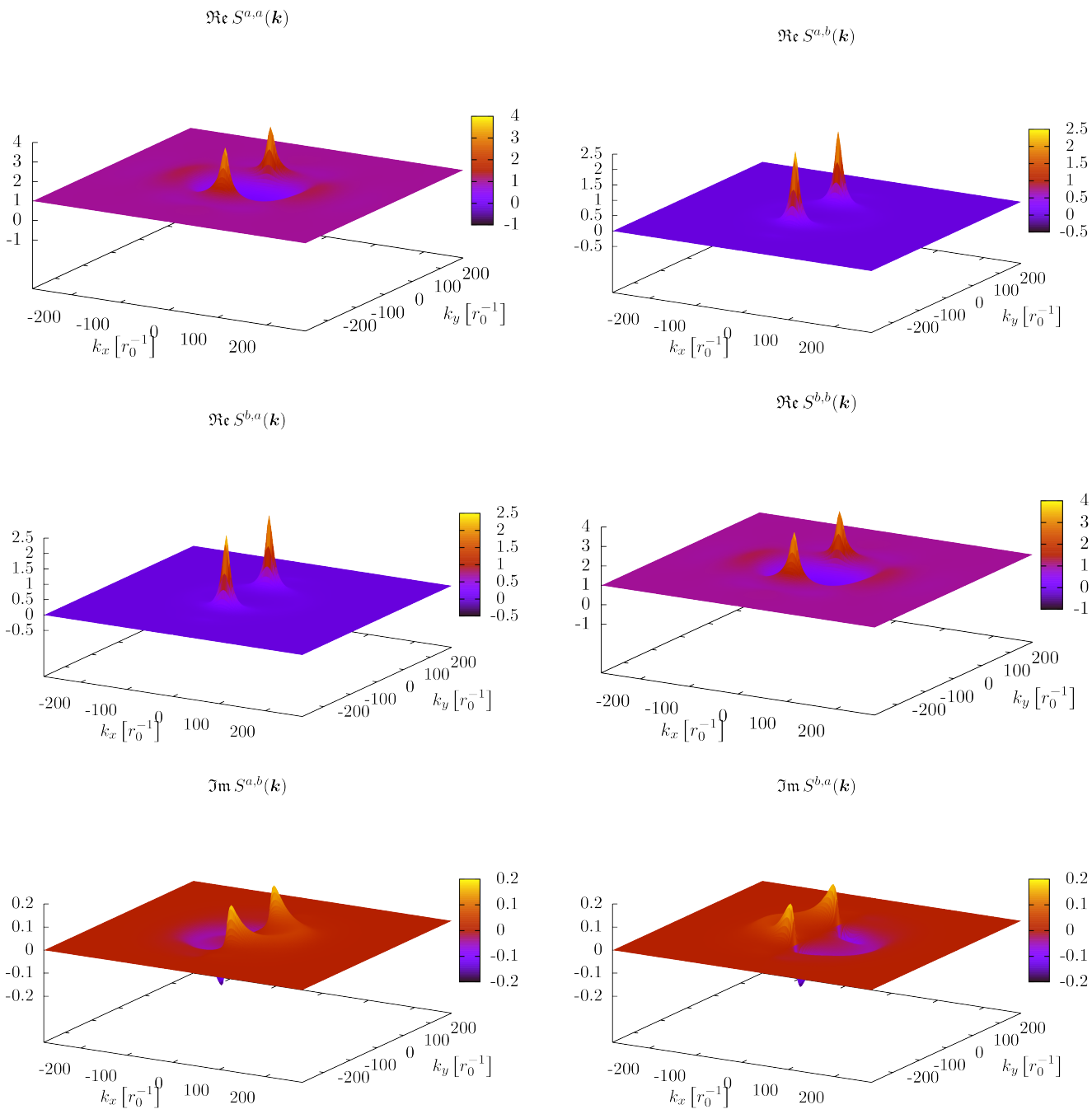


Figure 22: Like Figure 18. Dipoles are now tilted by $\theta = 0.175\pi$. Note the high peaks only along the y-axis.

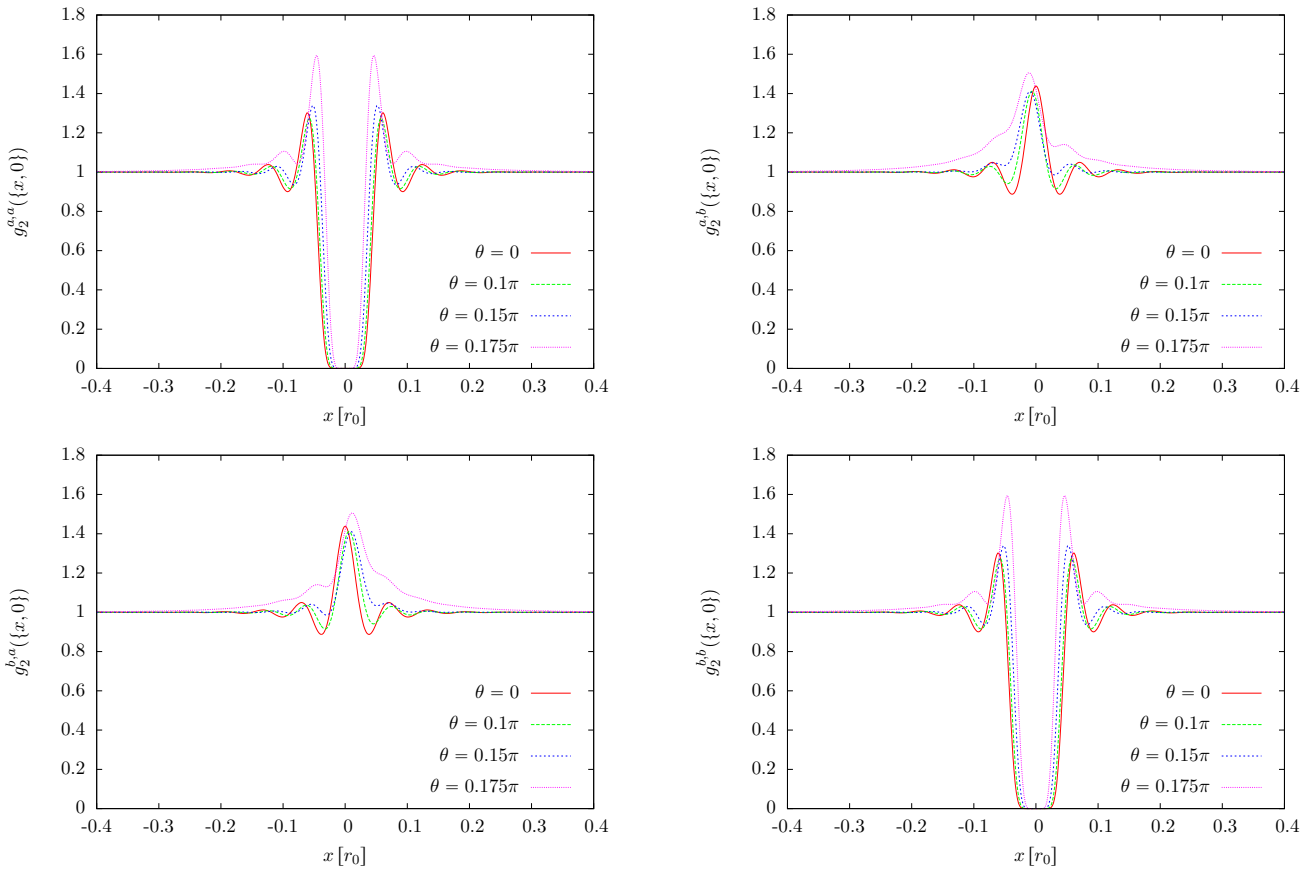


Figure 23: Pair distribution functions $g_2^{a,a}(\boldsymbol{r})$, $g_2^{a,b}(\boldsymbol{r})$, $g_2^{b,a}(\boldsymbol{r})$, and $g_2^{b,b}(\boldsymbol{r})$ along the x-axis. Results for two dipole layers, for the densities $\rho_1^a = \rho_1^b = 256\, r_0^{-2}$, for a distance of $d = 0.06\, r_0$ between the layers and for multiple dipole orientations $\theta = 0$, $\theta = 0.1\pi$, $\theta = 0.15\pi$, and $\theta = 0.175\pi$. See also Figures 13, 17, 19, and 21. Note that the inter-layer pair distribution functions are no even functions any more along the x-axis. No stable solutions for $\theta > \theta_{\text{crit}} = 0.175\pi$

.

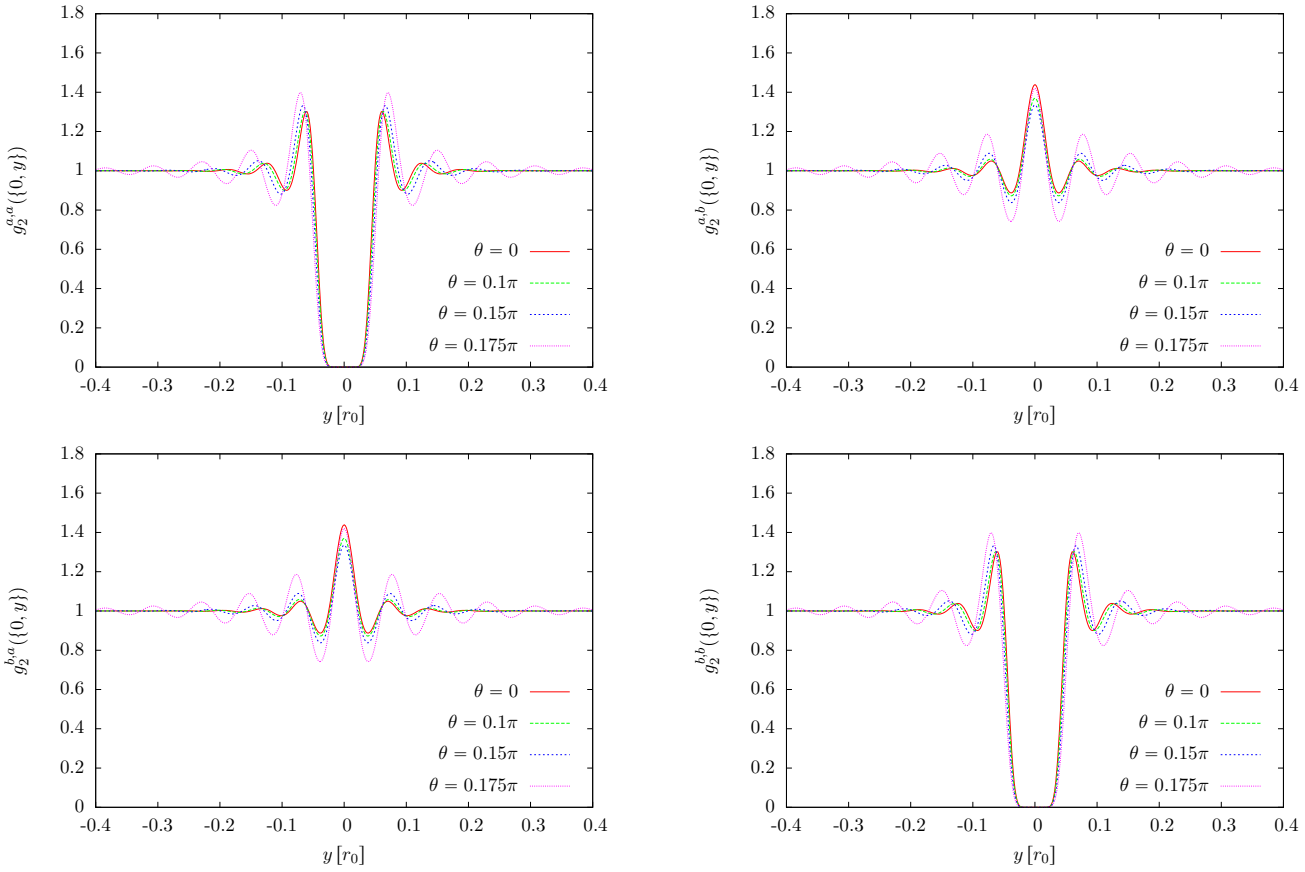


Figure 24: Like Figure 23, but along the y-axis. Note that the pair distribution functions are even along the y-axis.

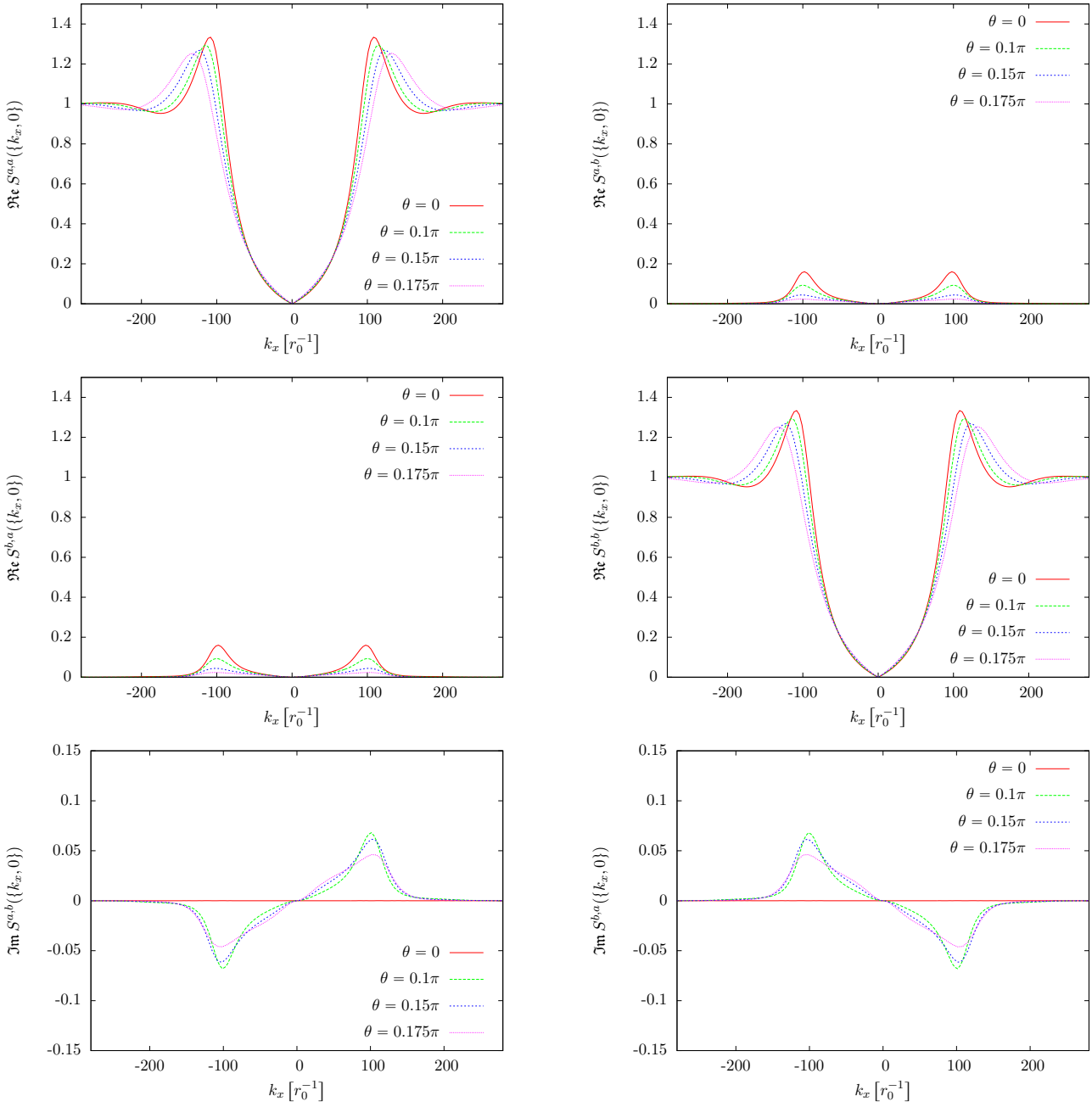


Figure 25: Static structure functions $S^{a,a}(\boldsymbol{k})$, $S^{a,b}(\boldsymbol{k})$, $S^{b,a}(\boldsymbol{k})$, and $S^{b,b}(\boldsymbol{k})$ along the x-axis. Results for two dipole layers, for the densities $\rho_1^a\rho_1^b = 256\, r_0^{-2}$, for a distance of $d = 0.06\, r_0$ between the layers and for multiple dipole orientations $\theta = 0$, $\theta = 0.1\pi$, $\theta = 0.15\pi$, and $\theta = 0.175\pi$. See also Figures 14, 18, 20, and 22. Note that the inter-layer pair distribution functions are no even functions any more along the x-axis. No stable solutions for $\theta > \theta_{\text{crit}} = 0.175\pi$

.

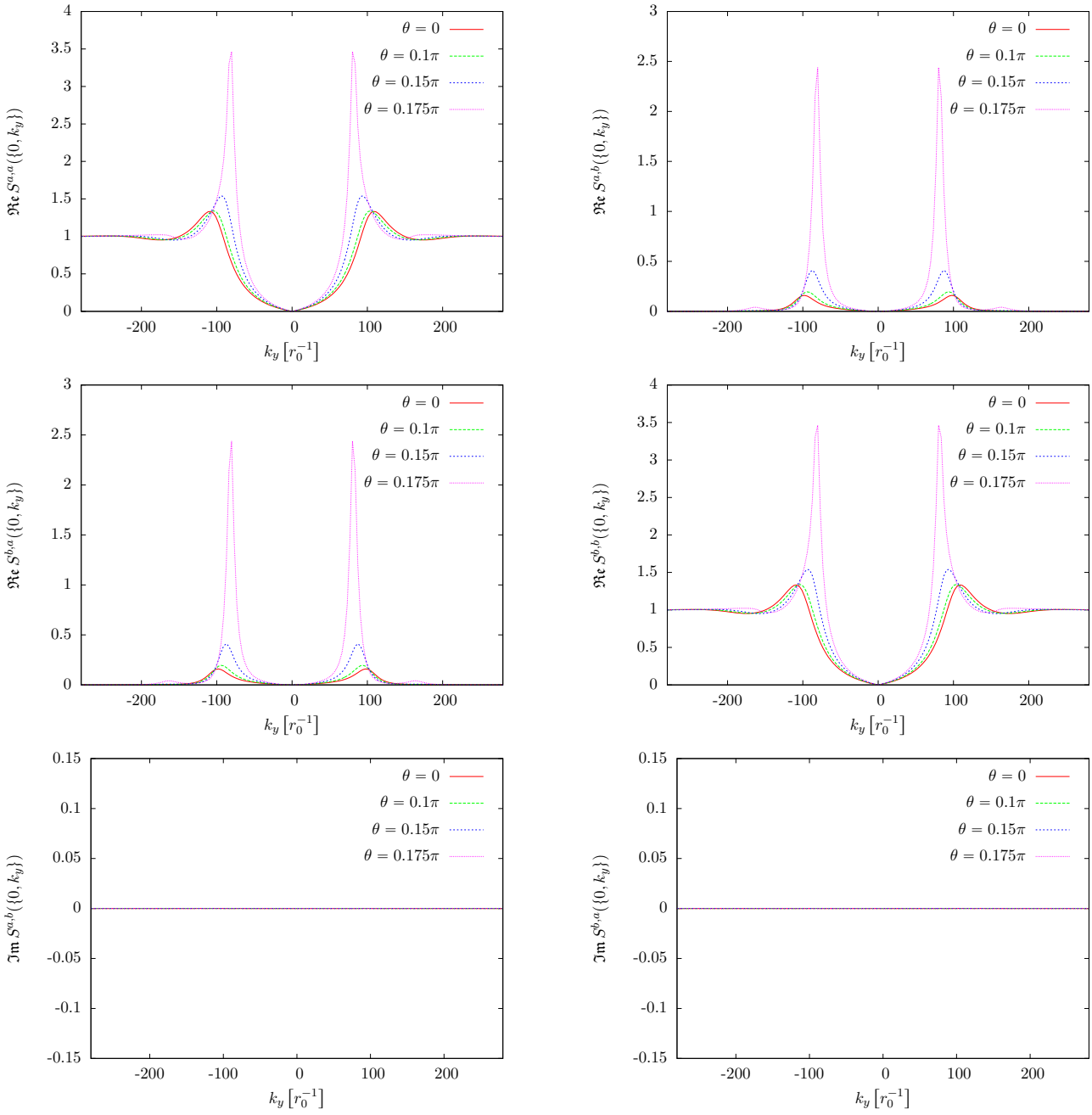


Figure 26: Like Figure 25, but along the y-axis. Note that the imaginary part of the static structure functions is 0, since the associated pair distribution functions are even along the y-axis (see Figure 23).

### 4.3.3 Varying Densities, fixed $d$, $\theta$

For bi-layer systems we have presented results of varying distances between the layers at fixed density and fixed dipole orientation, and we have presented results of varying dipole orientations at fixed density and fixed layer distance. So, what we'll do now is varying densities at fixed inter-layer distance $d = 0.15\, r_0$ and fixed dipole orientation $\theta = 0.175\pi$. Results are presented in Figures 27 to 30. One can see an interesting phenomenon: The intra-layer correlations are higher for denser systems, yet the inter-layer correlations are higher for dilute systems. This is why the layers can be brought closer together at high densities before dimerization sets in. We were able to lower the densities down to $\rho_1^a = \rho_1^b = 16\, r_0^{-2}$.

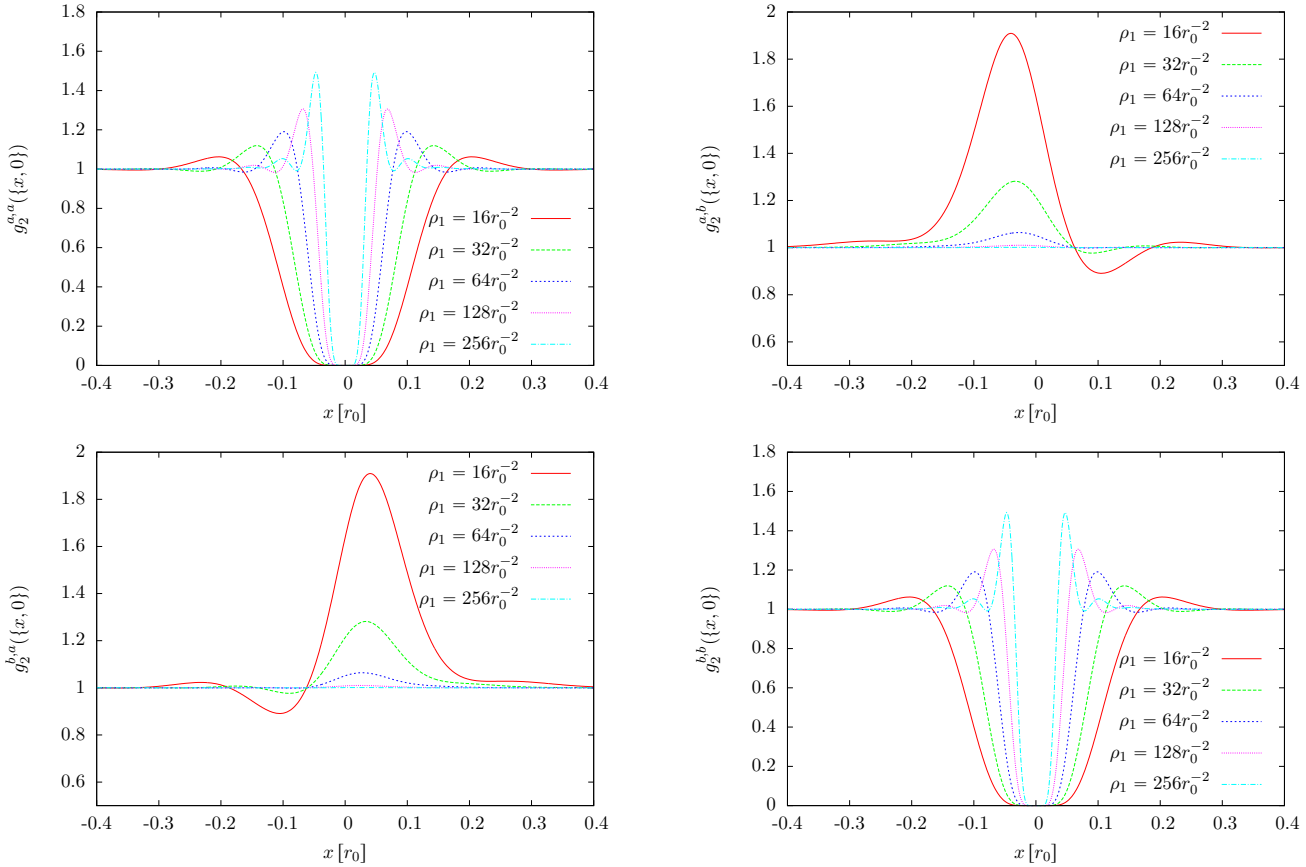


Figure 27: Pair distribution functions $g_2^{a,\,a}(\boldsymbol{r})$, $g_2^{a,\,b}(\boldsymbol{r})$, $g_2^{b,\,a}(\boldsymbol{r})$, and $g_2^{b,\,b}(\boldsymbol{r})$ along the x-axis. Results for two dipole layers, for a distance of $d = 0.15\, r_0$ between the layers, for a tilting angle of $\theta = 0.175\pi$, and for multiple densities $\rho_1^a = \rho_1^b$ with $\rho_1^a = 16\, r_0^{-2}$, $\rho_1^a = 32\, r_0^{-2}$, $\rho_1^a = 64\, r_0^{-2}$, $\rho_1^a = 128\, r_0^{-2}$, and $\rho_1^a = 256\, r_0^{-2}$. Note that the intra-layer correlations are highest for the highest density, while the inter-layer correlations are highest for the lowest density.

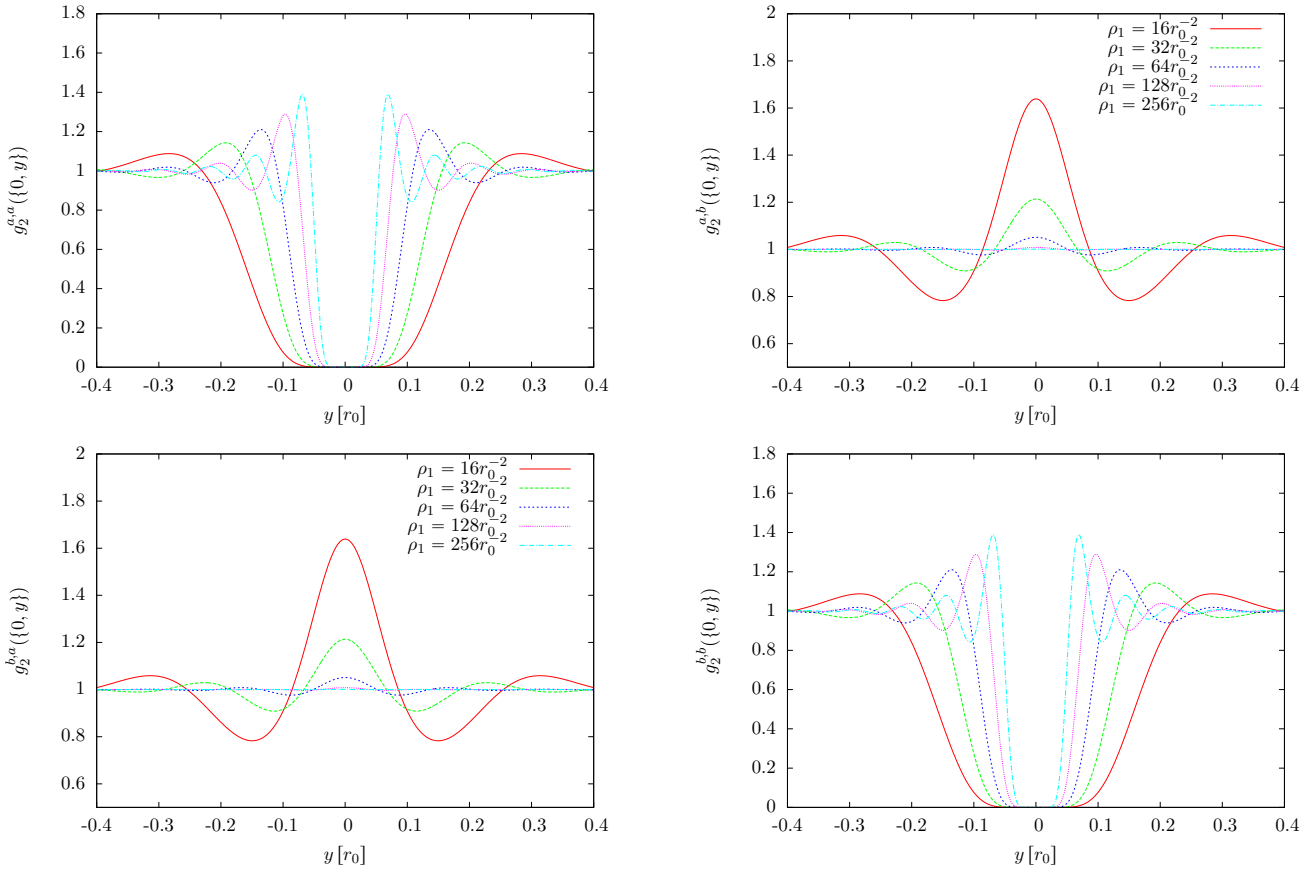


Figure 28: Like Figure 27, but along the y-axis.

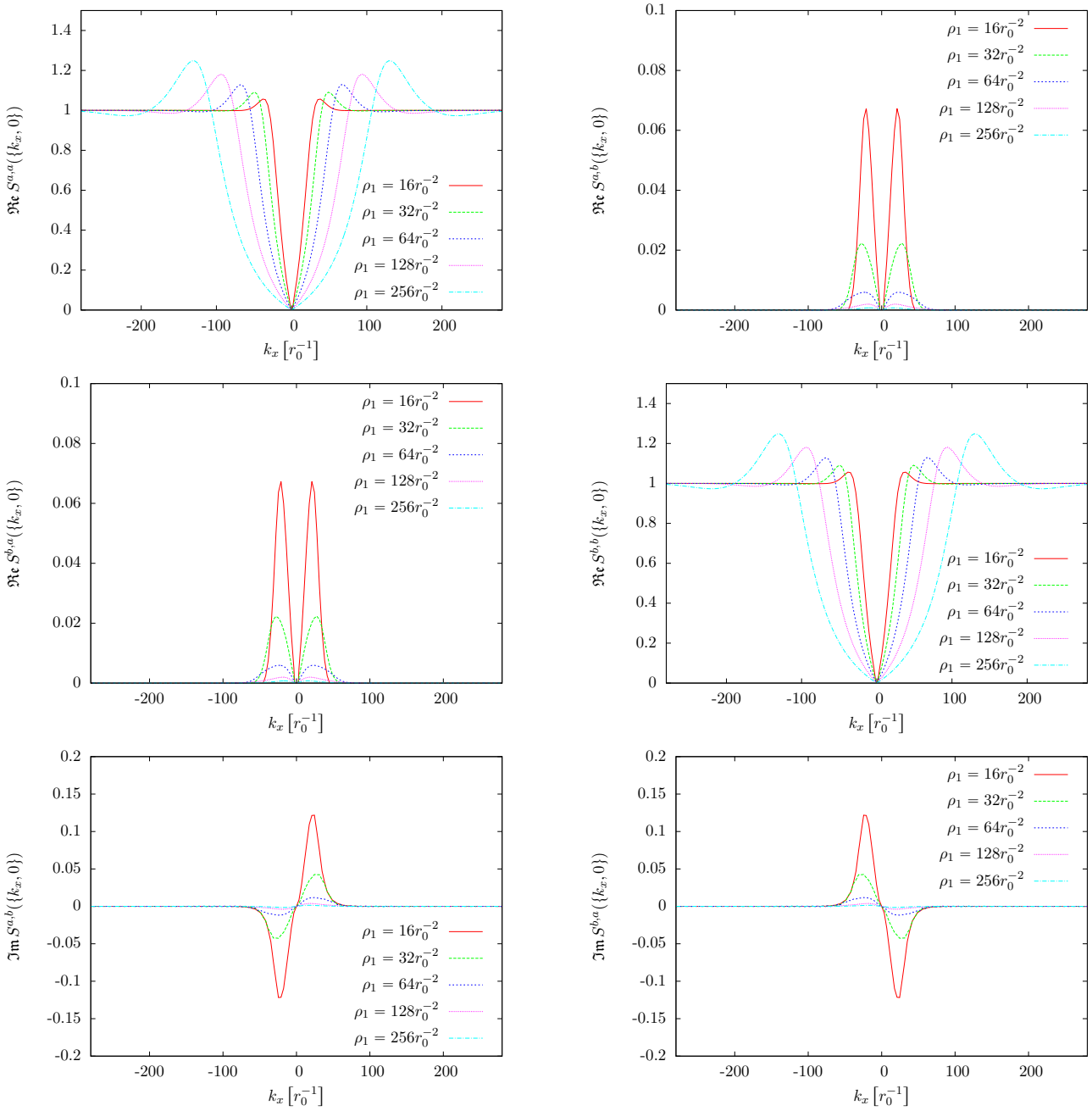


Figure 29: Static structure functions $S^{a,a}(\boldsymbol{k})$, $S^{a,b}(\boldsymbol{k})$, $S^{b,a}(\boldsymbol{k})$, and $S^{b,b}(\boldsymbol{k})$ along the x-axis. Results for two dipole layers, for a distance of $d = 0.15\,r_0$ between the layers, for a tilting angle of $\theta = 0.175\pi$, and for multiple densities $\rho_1^a = \rho_1^b$ with $\rho_1^a = 16\,r_0^{-2}$, $\rho_1^a = 32\,r_0^{-2}$, $\rho_1^a = 64\,r_0^{-2}$, $\rho_1^a = 128\,r_0^{-2}$, and $\rho_1^a = 256\,r_0^{-2}$.

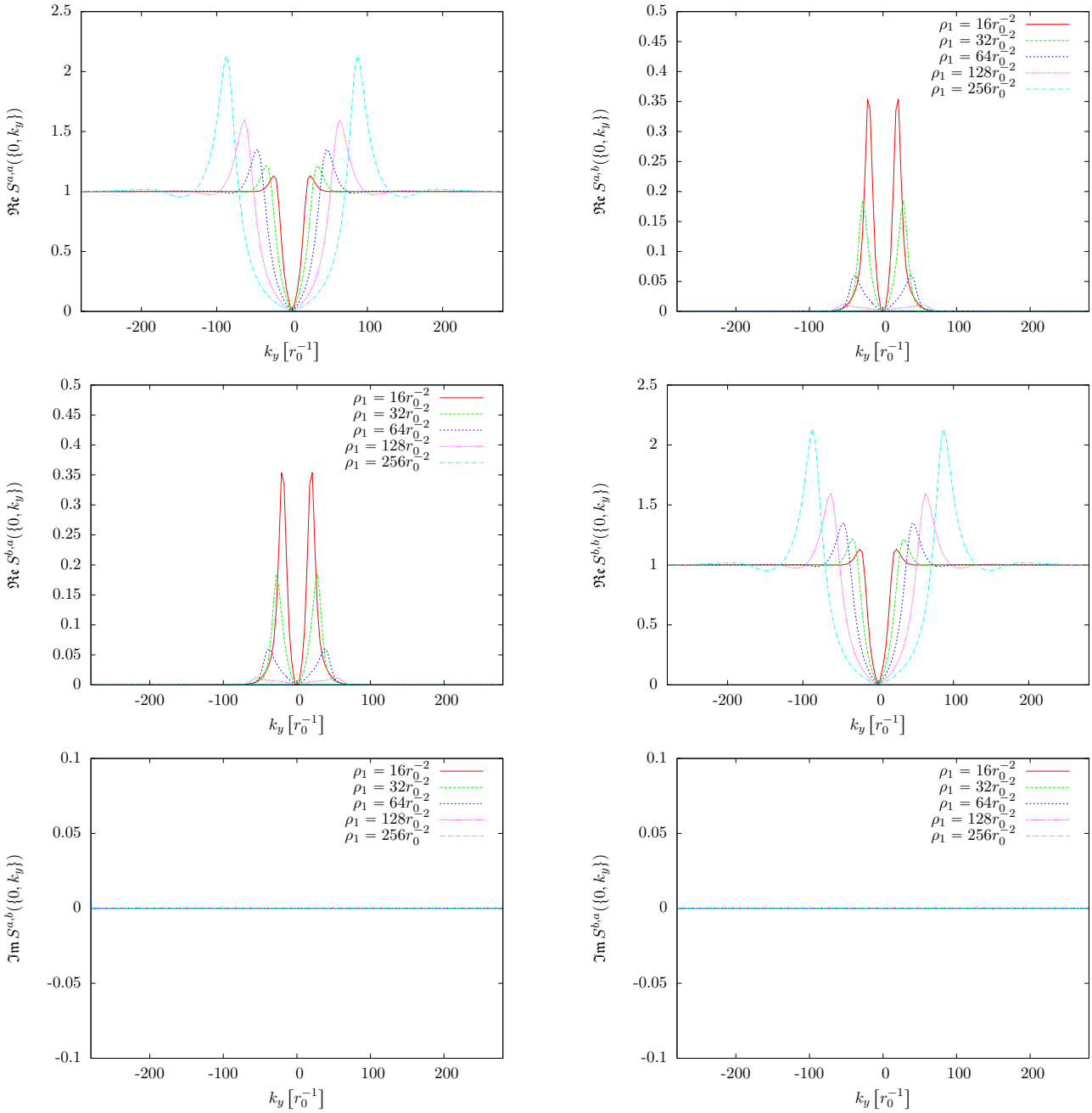


Figure 30: Like Figure 29, but along the y-axis.

### 4.3.4 Different Densities in the two Layers

A situation worth discussing is a system of two layers with different dipole densities. Figure 31 and 32 show pair distribution functions and static structure function computed for dipole layers with $\rho_1^a = 256\, r_0^{-2}$, $\rho_1^b = 16\, r_0^{-2}$ and $d = 0.07\, r_0$. Interestingly, the first peaks in $g_2^{a,b}$ and $g_2^{b,a}$ are higher than the first peak in $g_2^{b,b}$, thus dipoles in the low density $b$-layer seem to be more correlated to dipoles in the high density $a$-layer than to dipoles in their own layer.

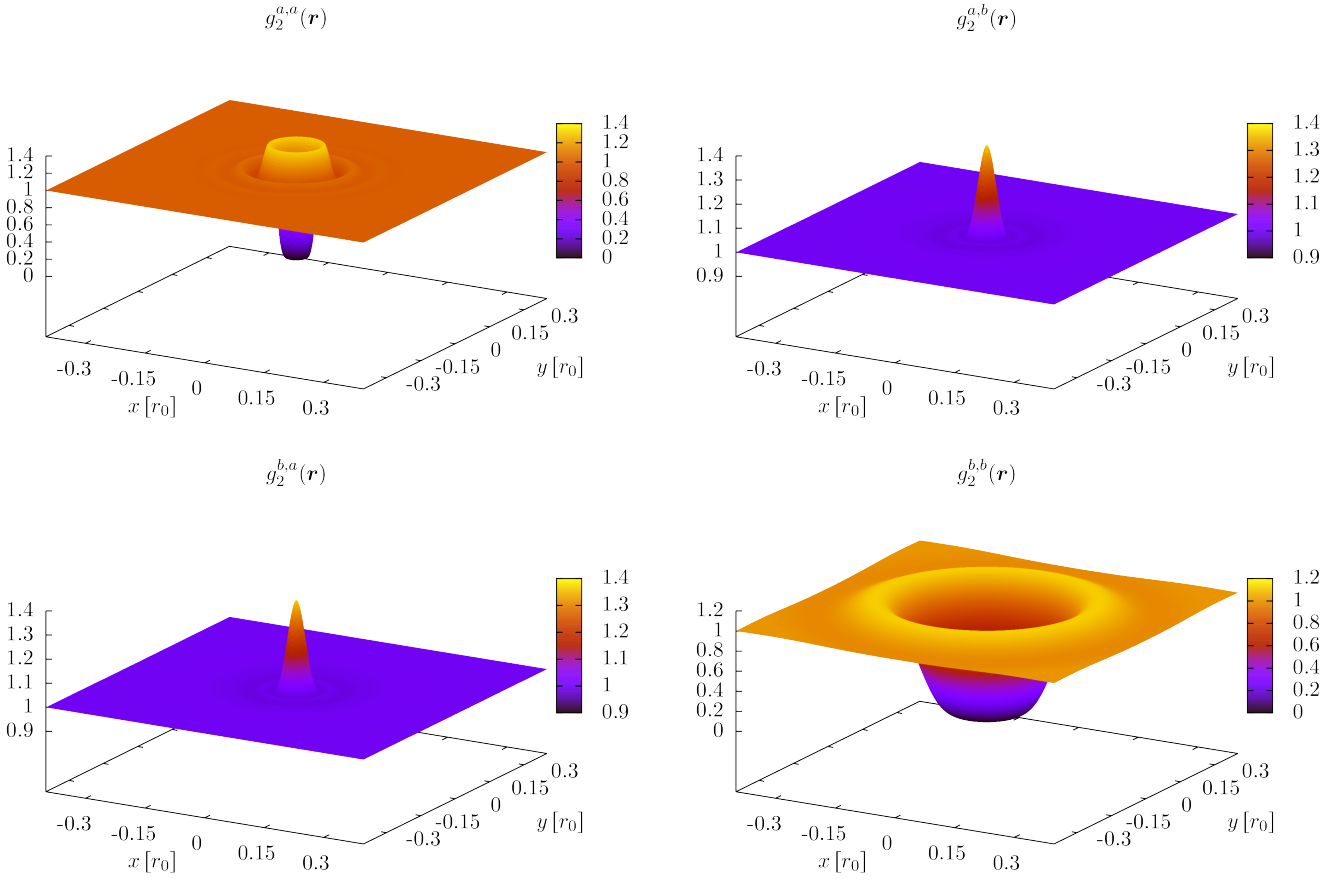


Figure 31: Pair distribution functions $g_2^{a,a}(\boldsymbol{r})$, $g_2^{a,b}(\boldsymbol{r})$, $g_2^{b,a}(\boldsymbol{r})$, and $g_2^{b,b}(\boldsymbol{r})$ for two dipole layers, for a distance of $d = 0.07\, r_0$ between the layers, no tilting, and for very different densities $\rho_1^a = 256\, r_0^{-2}$, $\rho_1^b = 16\, r_0^{-2}$ Note that the inter-layer correlations are higher, than the intra-layer correlation in the low density layer.

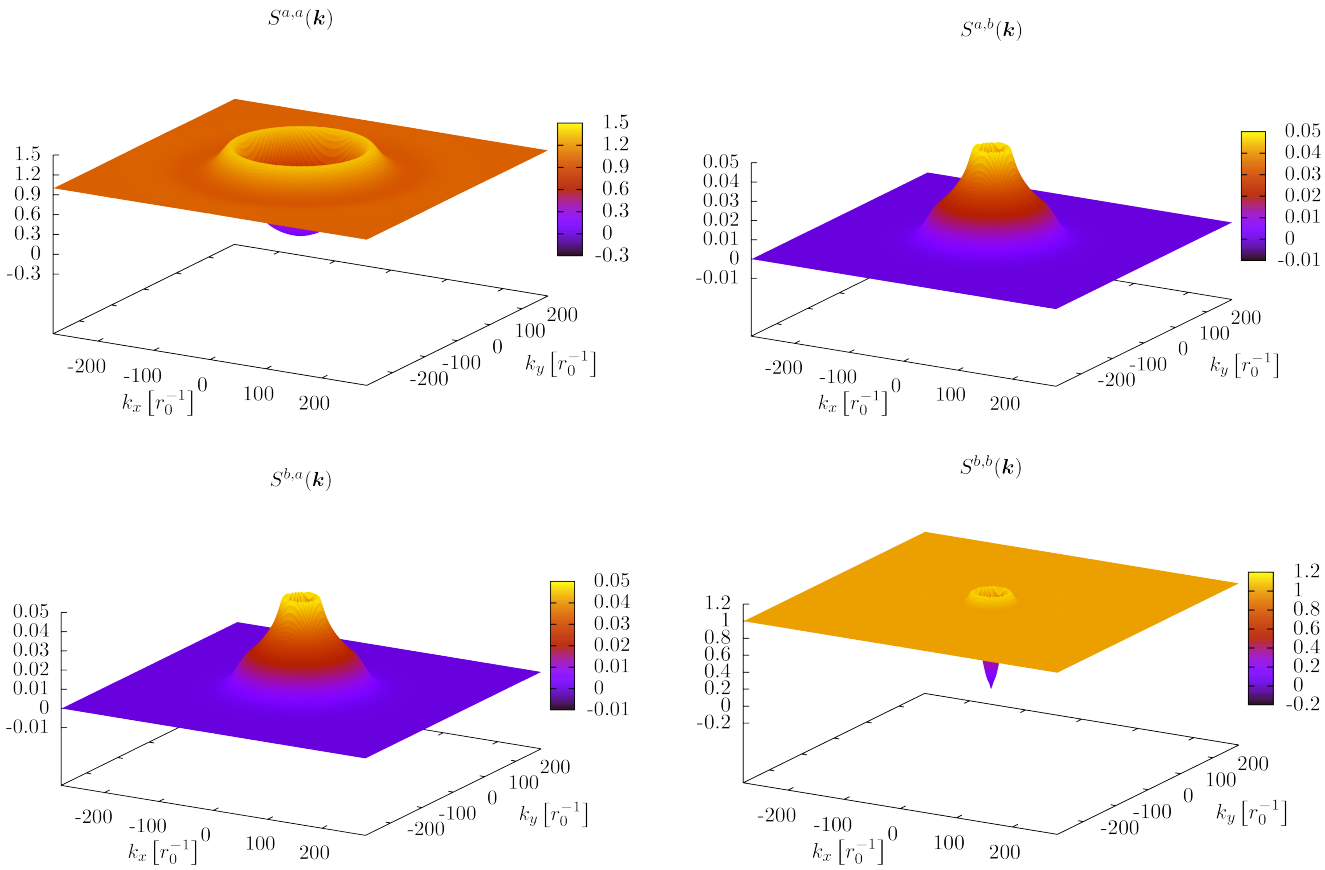


Figure 32: Static structure functions $S^{a,a}(\boldsymbol{k})$, $S^{a,b}(\boldsymbol{k})$, $S^{b,a}(\boldsymbol{k})$, and $S^{b,b}(\boldsymbol{k})$ for two dipole layers, for a distance of $d = 0.07\,r_0$ between the layers, no tilting, and for very different densities $\rho_1^a = 256\,r_0^{-2}$, $\rho_1^b = 16\,r_0^{-2}$ See Figure 31 for the associated pair distribution functions.

### 4.3.5 Antiparallel Dipole Orientation

Another quite interesting experiment is to orient dipoles in a system of two layers perpendicular to the layers, but in such a way that the dipoles of the first layer are antiparallel to those in the second layer. Figures 33 and 34 show such a system with the parameters $\rho_1^a = \rho_1^b = 256\, r_0^{-2}$ and $d = 0.06\, r_0$. Note that the inter-layer static structure functions look almost like those from Figure 14 mirrored at the $S^{a,b} = 0$ plain, i.e. $S^{a,b}_{\text{parallel}}(\boldsymbol{k}) \approx -S^{a,b}_{\text{antiparallel}}(\boldsymbol{k})$. However, this relation is only true approximately, it does not hold up under examination. The same is true for the pair distribution functions, but those seem to be mirrored at the $g_2^{a,b} = 1$ plain. About the same way that parallel dipoles from different layers in Figure 13 are correlated, the antiparallel dipoles from Figure 33 are anti-correlated.

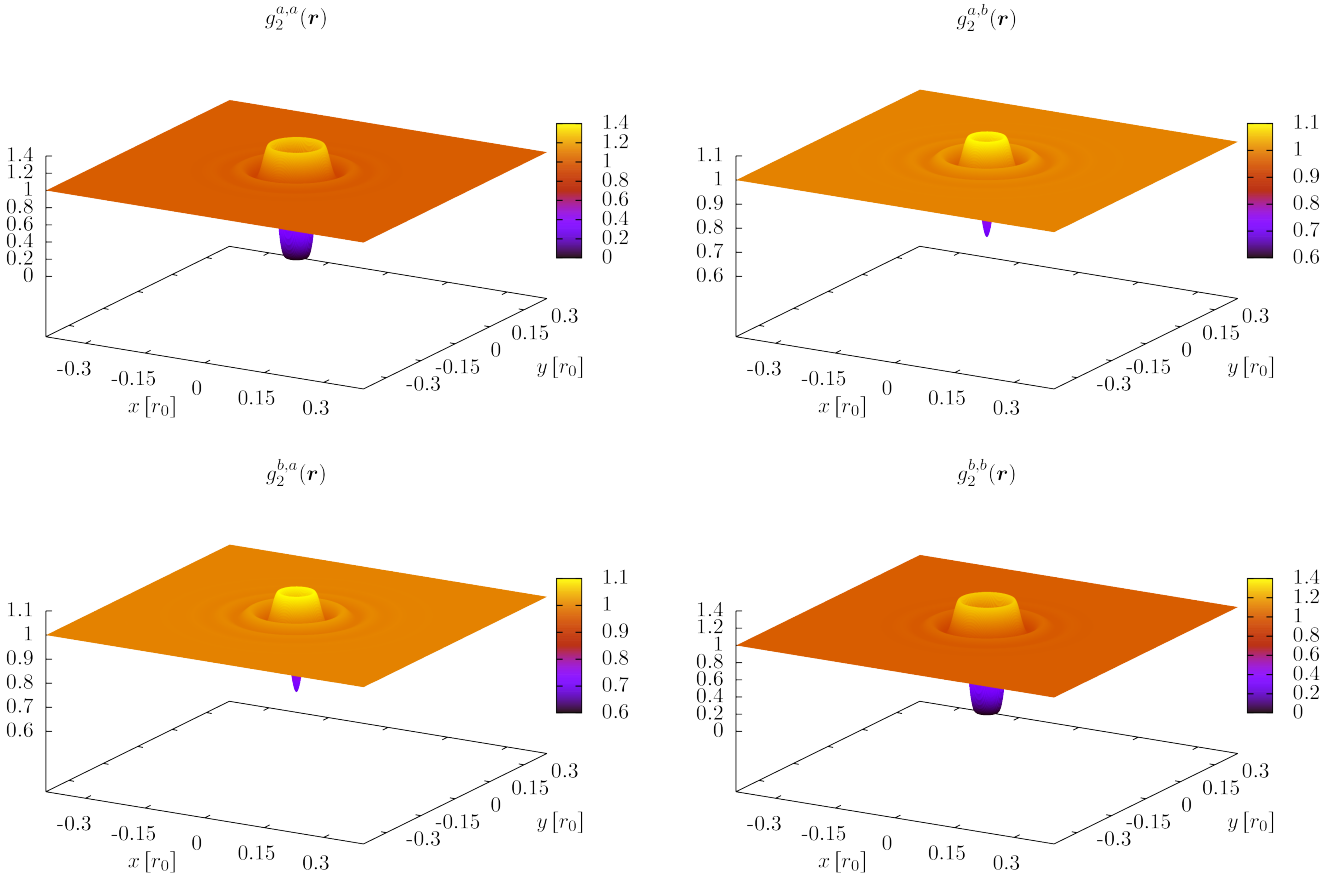


Figure 33: Pair distribution functions $g_2^{a,a}(\boldsymbol{r})$, $g_2^{a,b}(\boldsymbol{r})$, $g_2^{b,a}(\boldsymbol{r})$, and $g_2^{b,b}(\boldsymbol{r})$ for two dipole layers, for a distance of $d = 0.06\, r_0$ between the layers, and for densities $\rho_1^a = \rho_1^b 256\, r_0^{-2}$. In both layers the dipoles are oriented perpendicular to the layer, but antiparallel to dipoles in the other film Note that in contrast to previous results for parallel dipole orientations (see Figure 13), the inter-layer pair distribution functions are minimal at $\boldsymbol{r} = \boldsymbol{0}$ due to the repulsive dipole-dipole interaction.

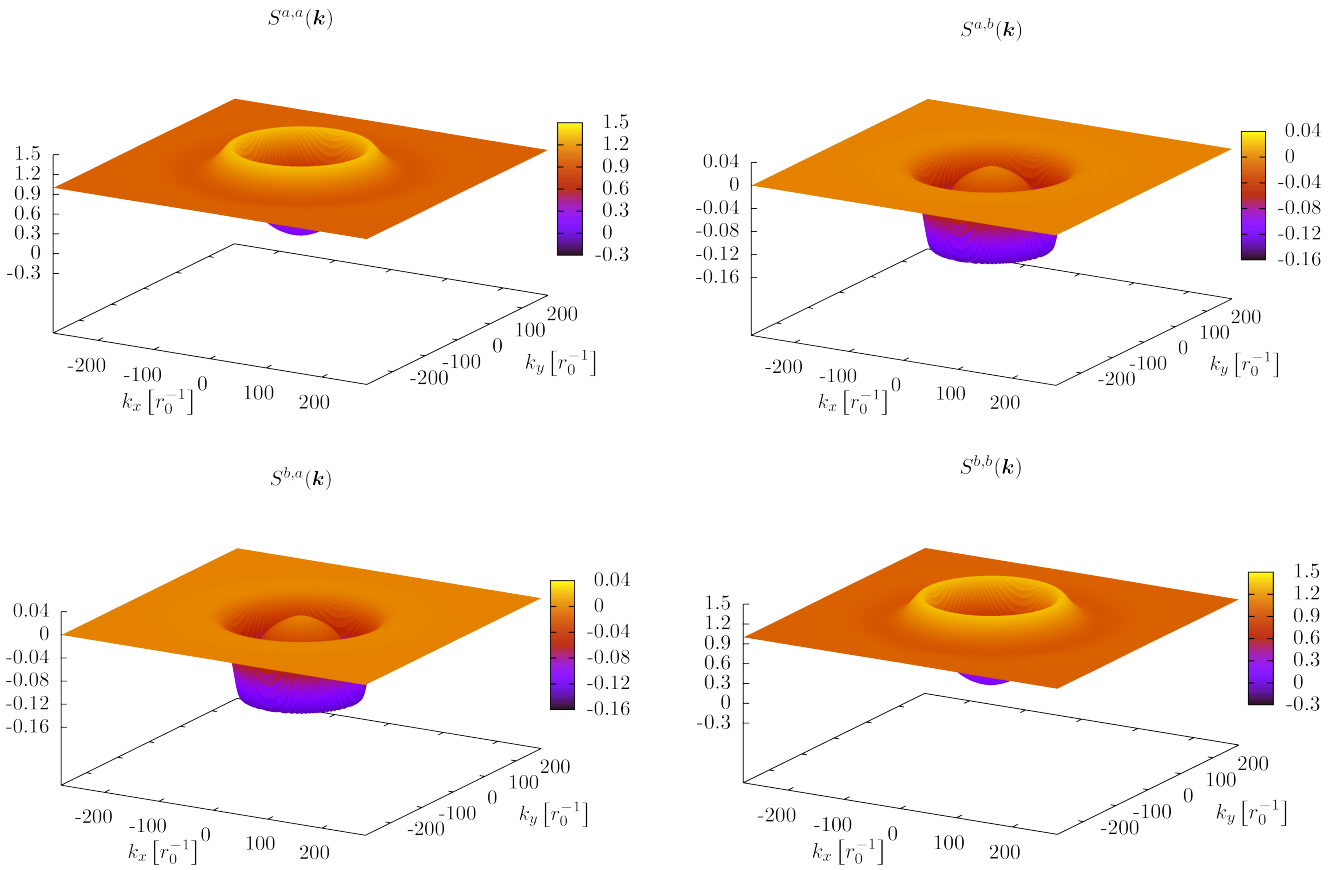


Figure 34: Static structure functions $S^{a,a}(\boldsymbol{k})$, $S^{a,b}(\boldsymbol{k})$, $S^{b,a}(\boldsymbol{k})$, and $S^{b,b}(\boldsymbol{k})$ for two dipole layers, for a distance of $d = 0.06\,r_0$ between the layers, and for densities $\rho_1^a = \rho_1^b 256\,r_0^{-2}$. In both layers the dipoles are oriented perpendicular to the layer, but antiparallel to dipoles in the other film

## 4.4 Three Dipole Layers

Figures 35 and 36 show a system of three equidistantly ($d = 0.06\,r_0$) stacked dipole layers at densities of $\rho_1^a = \rho_1^b = \rho_1^c = 256\,r_0^{-2}$. When the plots showing the pair distribution functions and static structure functions are arranged in matrix form, like in Figures 35 and 36, one can observe what is especially true for systems with even more dipole layers: The correlations in the main diagonal ($g_2^{a,a}$, $g_2^{b,b}$ and $g_2^{c,c}$) are the strongest and decrease with increasing distance from the main diagonal.

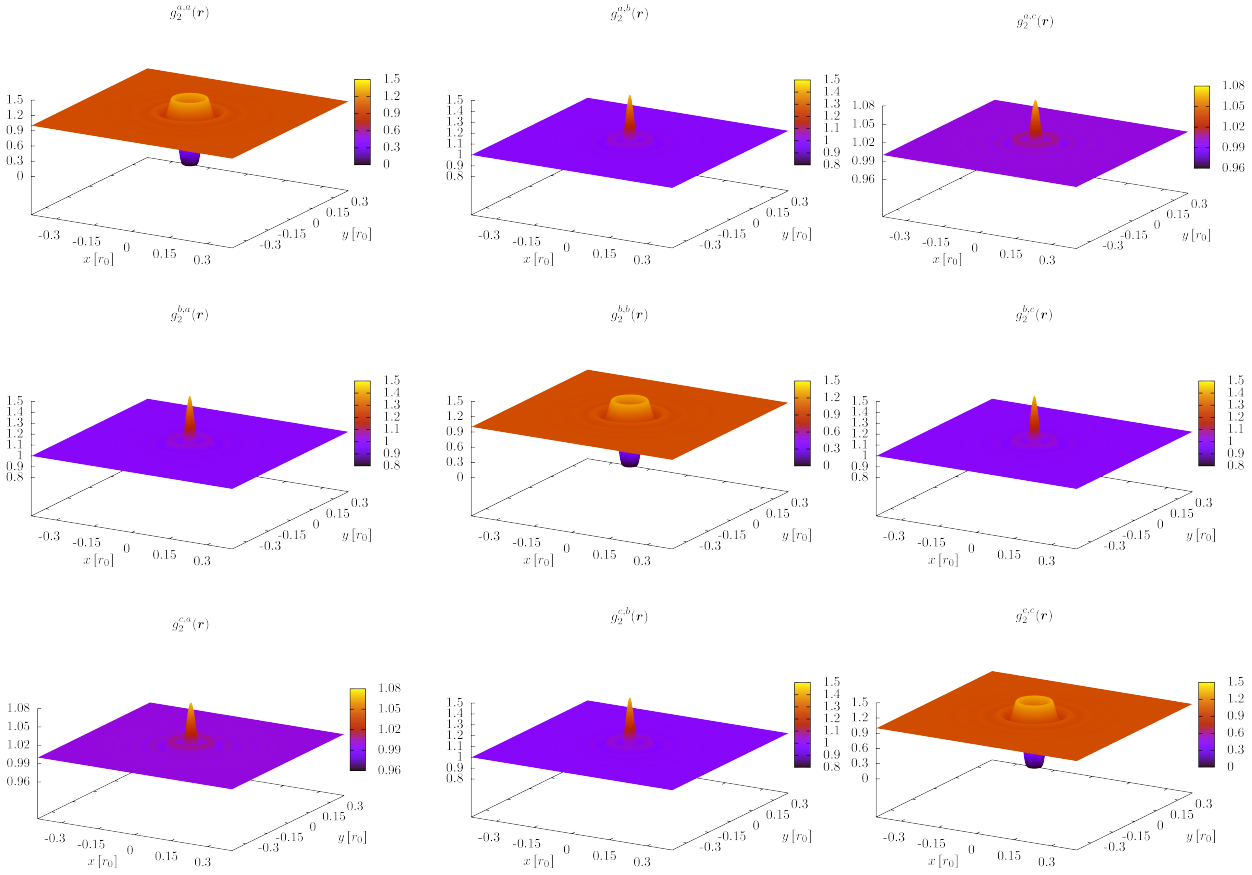

Figure 35: Pair distribution functions $g_2^{a,a}(\boldsymbol{r})$, $g_2^{a,b}(\boldsymbol{r})$, $g_2^{a,c}(\boldsymbol{r})$, $g_2^{b,a}(\boldsymbol{r})$, $g_2^{b,b}(\boldsymbol{r})$, $g_2^{b,c}(\boldsymbol{r})$, $g_2^{c,a}(\boldsymbol{r})$, $g_2^{c,b}(\boldsymbol{r})$, and $g_2^{c,c}(\boldsymbol{r})$ for three dipole layers, for distances of $d = 0.06\,r_0$ between the layers, and for densities $\rho_1^a = \rho_1^b = \rho_1^c = 256\,r_0^{-2}$. In both layers the dipoles are oriented perpendicular to the layer. Note that the correlations in the main diagonal are the strongest. The farther away from the main diagonal, the less correlations.

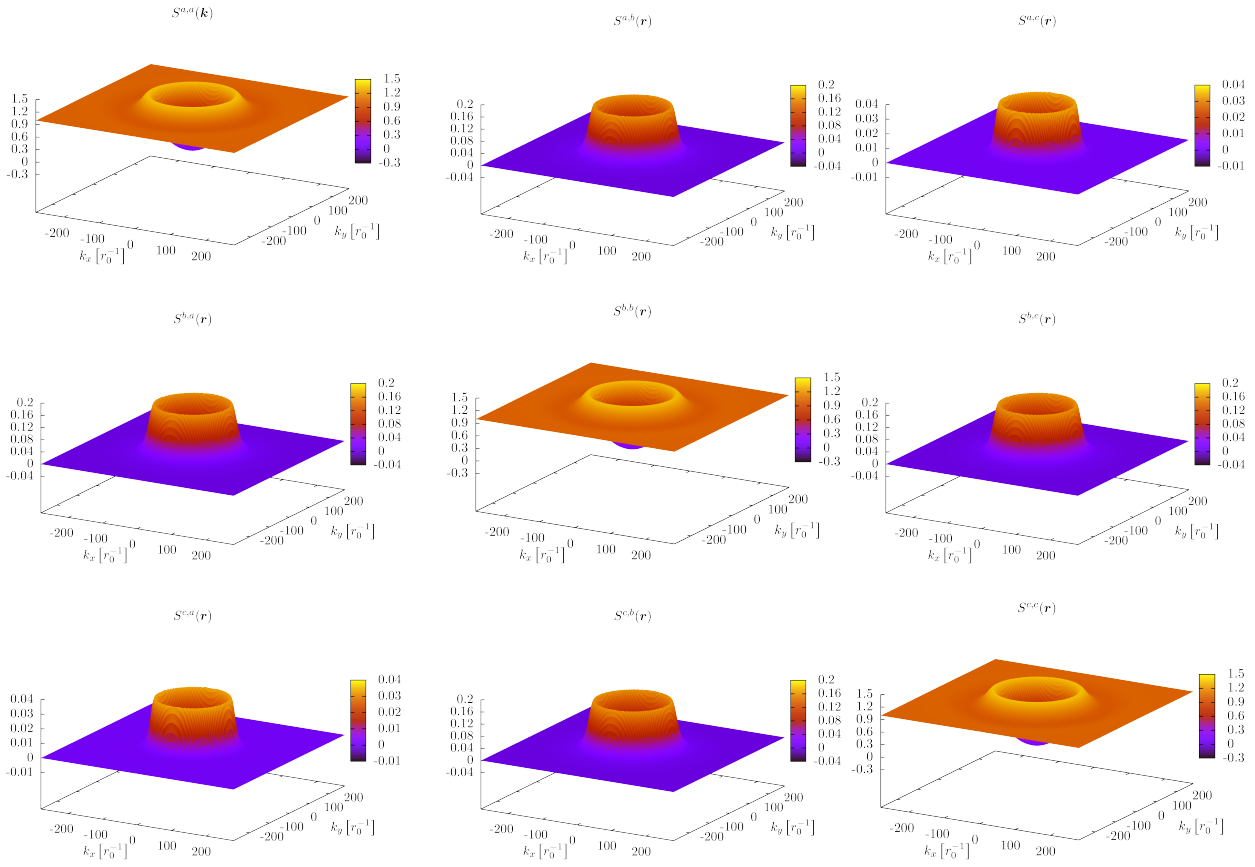


Figure 36: Static structure functions $S^{a,\,a}(\boldsymbol{k})$, $S^{a,\,b}(\boldsymbol{k})$, $S^{a,\,c}(\boldsymbol{k})$, $S^{b,\,a}(\boldsymbol{k})$, $S^{b,\,b}(\boldsymbol{k})$, $S^{b,\,c}(\boldsymbol{k})$, $S^{c,\,a}(\boldsymbol{k})$, $S^{c,\,b}(\boldsymbol{k})$, and $S^{c,\,c}(\boldsymbol{k})$ for three dipole layers, for distances of $d = 0.06\,r_0$ between the layers, and for densities $\rho_1^a = \rho_1^b = \rho_1^c = 256\,r_0^{-2}$. In both layers the dipoles are oriented perpendicular to the layer.

# 5 Conclusions

In this bachelor thesis we have discussed the ground state of strongly interacting bose gases of tilted dipoles in coupled 2D-layers. We have reduced the problem to an equivalent problem of homogeneous, multi-component dipolar bose gas in one single 2D-layer. Then hypernetted-chain Euler-Lagrange theory has been applied onto this system. Therefore we made an ansatz for the wave function including pair correlations $u_2^{\alpha,\beta}(\boldsymbol{r})$ and minimized energy according to Ritz' variational principle. In the process of calculating the functional derivative one comes across the pair distribution matrix $\boldsymbol{g}_2(\boldsymbol{r})$, which is basically the fourier transform of the static structure matrix $\boldsymbol{S}(\boldsymbol{k})$. To successfully calculate the functional derivative one has to find a relation between $\boldsymbol{g}_2(\boldsymbol{r})$ and $\boldsymbol{u}_2(\boldsymbol{r})$. This relation can be found via diagrammatic expansion leading to the Ornstein-Zernike equation and the hypernetted-chain equation. Neglecting so-called "elementary diagrams", these equations together with the Euler-Lagrange method are sufficient to formulate a set of conditional equations for $\boldsymbol{g}_2(\boldsymbol{r})$. We implemented an algorithm solving the resulting equations iteratively. We computed the static structure functions and the pair distribution functions for several systems up to three coupled layers.

The computations have shown several interesting phenomena in the homogeneous Bose gas of aligned dipoles trapped in coupled 2D layers. Higher densities lead to higher intra-layer correlations, but weaker inter-layer correlations. The correlations are also affected by the distance between the layers. Layers far apart are effectively two separate systems, not correlated at all. The correlations grow stronger when the distance between the layers is reduced, but only until a critical distance. Below this critical distance the HNC-EL equations do not converge any more. This suggests a dimerization takes place. Dimerization cannot be described with a wave function ansatz only containing pair correlations. Thus the HNC-EL equations do not converge. This critical distance depends on both tilting angle and densities. These factors both affect the strength of inter-layer correlations. When the inter-layer correlations are increased, e.g. by lowering the density, the critical distance rises. With higher densities the layers can be brought closer together before dimerization sets in. Tilting of the dipoles makes the dipole-dipole interaction anisotropic, leading to anisotropic pair distribution functions and static structure functions. With two or more layers static structure functions can even be complex. Tilting of the dipoles in direction of the x-axis causes the dipoles getting closer along x-axis and getting farther apart from each other along y-axis, preserving density in total. At high tilting angles the system even tends to get solid along the y-axis and stays gaseous along x-axis. In the case of multiple layers the computations have shown that correlations in the main diagonal of the pair distribution and static structure matrices are the strongest ones and decrease with increasing distance from the main diagonal. This would justify a restriction of inter-layer correlations to only neighbouring layers.

In this thesis, however, we present only systems with parallel or antiparallel dipole orientation. Furthermore this thesis only presents results for systems containing up to three dipole layers. The theory developed is capable of treating systems with arbitrary dipole orientations and layer counts, though. The most simple version of the HNC-EL method is not quite as accurate as Monte Carlo simulations, the results are qualitatively correct, though. However, a big advantage of HNC-EL over Mote Carlo methods is, that it's faster by orders of magnitude. Results for the bi-layer systems presented in this bachelor thesis usually take about 40 minutes of computation time on a dual core home computer. Furthermore, the computation time could be decreased massively due to the very high parallelizability of the algorithm.

In the theory presented in this paper, some approximations were introduced, namely the restriction of the wave function to pair correlations and the neglect of elementary diagrams. These approximations hardly effect systems at lower densities, so those results are quite accurate. At higher densities, such as $\rho_1 = 256\, r_0^{-2}$, however, the accuracy decreases. However, the theory can be improved by introducing triplet correlations and taking some of the elementary diagrams into account. This makes the theory both faster than Monte Carlo simulations and in case of $^4$He almost as accurate as Monte Carlo methods.

There are interesting questions, that should be addressed in future work:

- The HNC-EL equations with a pair correlations ansatz do not converge at low inter-layer distances due to dimerization. Can dimerization be described when higher order correlations are included?
- Can the algorithm be improved exploiting some more symmetries, which could result from dipole orientations in some special cases?

Not only the ground state, but also excitations in the homogeneous Bose gas of aligned dipoles trapped in coupled 2D layers are interesting. For the calculation of excitations the ground state is the basis to start from. Excitations for some of the systems covered in this bachelor thesis were computed by Michael Rader [12].

## References


[1] K. Aikawa, A. Frisch, M. Mark, S. Baier, A. Rietzler, R. Grimm, and F. Ferlaino. Bose-Einstein condensation of erbium. *Phys. Rev. Lett.*, 108:210401, May 2012.

[2] G. E. Astrakharchik, J. Boronat, I. L. Kurbakov, and Y. E. Lozovik. Quantum phase transition in a two-dimensional system of dipoles. *Phys. Rev. Lett.*, 98:060405, Feb 2007.

[3] M. A. Baranov, M. Dalmonte, G. Pupillo, and P. Zoller. Condensed matter theory of dipolar quantum gases. *Chem. Rev.*, 112:5012, August 2012.

[4] T. Chakraborty. Structure of binary boson mixtures at $T = 0$ K. *Phys. Rev. B*, 26:6131–6140, Dec 1982.

[5] T. Chakraborty. Variational theory of binary boson mixture at $T = 0$ K. *Phys. Rev. B*, 25:3177–3180, Mar 1982.

[6] J. P. Hansen and I. R. McDonald. *Theory of Simple Liquids*. Elsevier Science, 2006.

[7] K. Hiroike. Variational study of the ground state of a Bose-Einstein fluid. *Progress of Theoretical Physics*, 27(2):342–360, 1962.

[8] E. Krotscheck and J. W. Clark. Unpublished. Johannes Kepler Universität Linz.

[9] T. Lahaye, T. Koch, B. Fröhlich, M. Fattori, J. Metz, A. Griesmaier, S. Giovanazzi, and T. Pfau. Strong dipolar effects in a quantum ferrofluid. *Nature*, 448:672, 2007.

[10] M. Lu, N. Q. Burdick, S. H. Youn, and B. L. Lev. Strongly dipolar Bose-Einstein condensate of dysprosium. *Phys. Rev. Lett.*, 107:190401, 2011.

[11] A. Macia, D. Hufnagl, F. Mazzanti, J. Boronat, and R. E. Zillich. Excitations and stripe phase formation in a 2d dipolar Bose gas with tilted polarization. *Phys. Rev. Lett.*, 109:235307, 2012.

[12] M. Rader. Excitations in dense bose gases of tilted dipoles in coupled 2D-layers. Bachelor thesis. Johannes Kepler Universität Linz, 2013. Unpublished.

[13] M. Saarela, V. Apaja, and J. Halinen. *Structure and Dynamics of the bulk Liquid and bulk Mixtures*. World Scientific Pub Co Inc, first edition, November 2004.

[14] B. K. Stuhl, M. T. Hummon, M. Yeo, G. Quéméner, J. L. Bohn, and J. Ye. Evaporative cooling of the dipolar hydroxyl radical. *Nature*, 492:396, 2012.

[15] T. Takekoshi, M. Debatin, R. Rameshan, F. Ferlaino, R. Grimm, H.-C. Nägerl, C. R. Le Sueur, J. M. Hutson, P. S. Julienne, S. Kotochigova, and E. Tiemann. Towards the production of ultracold ground-state RbCs molecules: Feshbach resonances, weakly bound states, and the coupled-channel model. *Phys. Rev. A*, 85:032506, 2012.